

Experimental and Theoretical Investigations on Transition Metal and Lanthanide Containing Molecular Magnets

Dissertation

zur Erlangung des akademischen Grades doctor rerum naturalium
(Dr. rer. nat)

vorgelegt dem Rat der Chemisch-Geowissenschaftlichen Fakultät der
Friedrich-Schiller-Universität Jena

von Diplom-Chemiker David Hornig
geboren am 17. Oktober 1984 in Werdau

Gutachter:

1. Prof. Dr. Winfried Plass, Institut für Anorganische und Analytische Chemie, Friedrich-Schiller-Universität Jena
2. Prof. Dr. Stefanie Gräfe, Institut für Physikalische Chemie, Friedrich-Schiller-Universität Jena
3. Prof. Dr. Felix Tuzek, Institut für Anorganische Chemie, Christian-Albrechts-Universität Kiel

Tag der öffentlichen Verteidigung: 19. November 2014

DANKSAGUNG

An dieser Stelle möchte ich kurz allen meinen Dank aussprechen, die am Gelingen dieser Doktorarbeit direkt oder indirekt beteiligt waren.

Zuerst möchte ich meinem Betreuer Prof. Dr. Winfried Plass für die Möglichkeit danken, diese Dissertation in seiner Arbeitsgruppe anfertigen zu können. Der Wechsel von der organischen Synthese zur Magnetochemie war nicht leicht, doch bot er die Möglichkeit, das chemische Wissen beträchtlich zu erweitern. Besonders die großzügigen Freiheiten bei der Forschung sowie die wissenschaftlichen Diskussionen und Ratschläge wusste ich zu schätzen. Weiterhin bedanke ich mich für die zahlreichen Möglichkeiten, an wissenschaftlichen Konferenzen teilnehmen und dort auch Ergebnisse dem Fachpublikum präsentieren zu können.

Frau Prof. Dr. Stefanie Gräfe möchte ich für die Anfertigung des Zweitgutachtens danken.

Für die Korrekturen und Anmerkungen zum Manuskript danke ich Dr. Stephan Kupfer, Dr. Daniel Kinzel und Dr. Dirk Schuch.

Den Analytikabteilungen in der anorganischen und organischen Chemie danke ich für die Messung der NMR- und Massenspektren. Für die Messung der EPR-Spektren möchte ich mich bei Dr. Manfred Friedrich und Frau Bärbel Rambach bedanke. Dr. Axel Buchholz und Christa Felbel danke ich für die Messung der magnetischen Eigenschaften mit dem SQUID-Magnetometer.

Für das Messen und Lösen zahlreicher Strukturen, auch der mit dem „blöden Chloroform“, möchte ich Herrn Dr. Helmar Görls danken.

Bei der Hilfestellung zu zahlreichen Fragen bezüglich der Theorie, Labor, PC-Programmen am Anfang der Arbeit danke ich vor allem Dr. Eike T. Spielberg, Dr. Daniel Plaul, Daniel Geibig, sowie Dr. Dirk Schuch.

Dr. Axel Buchholz danke ich für die (teilweise mehrfache) Erklärung aller techni-

schen Geräte im Fuhrpark der Arbeitsgruppe sowie für die Einführung in die Röntgenkristallstrukturanalyse.

Den Mitgliedern der Arbeitsgruppe Plass danke ich für die angenehme Arbeitsatmosphäre und die nie versiegenden Vorrat an Kaffee und Espresso.

Der Mittagsrunde wechselnder Zusammensetzung möchte ich für die außerfachlichen Gespräche und die nötige Zerstreuung danken. Die Protagonisten: Dr. Roberto Menzel, Dr. Bobby Happ, Benedict Sandmann, Dr. Stephan Kupfer und Dr. Alexander Breul.

Meiner Familie und meinen Freunden gilt mein besonderer Dank für die seelische und moralische Unterstützung während der gesamten Zeit des Studiums und der Forschungsarbeit.

LIST OF PUBLICATIONS

Oral Presentations

- **Magnetische Anomalien bei Verzerrt Tetraedrischen Kupfer(II)komplexen mit Carbazolbasierten Schiffbaseliganden.** David Hornig. 8. *Mitteldeutsches Anorganiker-Nachwuchssymposium*, September 23, 2010, Halle/S., Germany.
- **Zweikernige Kupfer(II)komplexe mit Carbazolbasierten Liganden: Synthese und Eigenschaften.** David Hornig. 7. *Koordinationschemie-Treffen*, February 27 - March 1, 2011, Stuttgart, Germany.
- **Neue Einzelmolekülmagnete mit Tetraedrisch Koordinierten Cobalt(II)ionen.** David Hornig. 9. *Koordinationschemie-Treffen*, February 24-26, 2013, Bayreuth, Germany.
- **Neue Einzelmolekülmagnete mit Tetraedrisch Koordinierten Cobalt(II)ionen.** David Hornig. 11. *Mitteldeutsches Anorganiker-Nachwuchssymposium*, September 19, 2013, Dresden, Germany.

Poster Presentations

- **DFT-Studien zu den Magnetischen Eigenschaften von Oligonuklearen Kupferkomplexen.** David Hornig and Winfried Plass. 6. *Koordinationschemie-Treffen*, February 21-23, 2010, Mainz, Germany.
- **Single-Molecule Magnets Based on Cobalt(II) and Lanthanide(III) Ions.** David Hornig, Dirk Schuch, Abiodun Eseola, Axel Buchholz and Winfried Plass, *ACTINET-i3 ThUL School in Actinide Chemistry*, January 14-18, 2013, Karlsruhe, Germany.

List of Publications

- **Multiconfigurational Calculations on Molecular Magnets Based on 4f Ions.** David Hornig, Dirk Schuch and Winfried Plass. *EUFEN-2: 2nd European f-Element Chemistry Conference*, April 15-18, 2013, Dublin, Ireland.
- **Multiconfigurational Calculations on 3d and 4f Single-Molecule Magnets.** David Hornig, Dirk Schuch, Sven Ziegenbalg and Winfried Plass, *16. Frühjahrssymposium*, March 26-29, 2014, Jena, Germany.

Further Posters

- **From Byproducts to Efficient Fluorophores Based on Fused Pyrazines.** Jan Fleischhauer, Rainer Beckert, David Hornig and Yvonne Jüttke. *ORCHEM*, September 13-15, 2010, Weimar, Germany.
- **Substituenteneinflüsse auf das magnetische Verhalten von Cobalt(II) SMMs.** Sven Ziegenbalg, David Hornig and Winfried Plass. *10. Koordinationschemie-Treffen*, March 2-4, 2014, Kaiserslautern, Germany.

CONTENTS

Danksagung	iii
List of Publications	v
List of Abbreviations and Symbols	xi
I. Introductory Part	1
1. Introduction	3
1.1. Challenges in Information Technology	3
1.2. Magnetism of Paramagnetic Ions	4
1.2.1. Electronic Structure of Paramagnetic Ions	5
1.2.2. Cooperative Effects Between Paramagnetic Ions	8
1.3. Recent Areas of Interest in Magnetochemistry	9
1.3.1. Single-Molecule Magnets	9
1.3.2. Spin-Frustration	11
1.3.3. Spin-Crossover	12
1.4. Aims of this Work	12
2. Theoretical Methods	15
2.1. <i>Ab initio</i> Methods	16
2.1.1. Hartree-Fock Approximation	16
2.1.2. Configuration Interaction	20
2.1.3. Complete Active Space SCF Method	21
2.1.4. CASPT2 Method	23

2.2.	Density Functional Theory	24
2.2.1.	Hohenberg-Kohn Theorems and Kohn-Sham Method	24
2.2.2.	Important Exchange-Correlation Functionals	26
2.2.3.	The Broken-Symmetry Formalism	28
2.3.	Practical Aspects for Calculations on 3d and 4f Complexes	30
II.	Results	33
3.	Dinuclear Metallamacrocycles with Carbazole-Based Ligands	35
3.1.	Synthesis	36
3.1.1.	Synthesis of the Ligand	36
3.1.2.	Synthesis of the Complexes	37
3.2.	Crystal Structures	38
3.3.	Magnetic Properties	43
3.3.1.	Copper(II) Complexes	44
3.3.2.	Cobalt(II) Complexes	47
4.	Electronic Structure of Tetrahedral Cobalt(II) SMMs	53
4.1.	[N ₂ O ₂] Coordinated Cobalt(II) Complexes	55
4.2.	Systematic Calculations on the Distortion of Tetrahedral Cobalt(II)	61
5.	Linear Cobalt(II) Complexes	65
5.1.	Energy Spectrum of CoCl ₂	66
5.2.	Potential Linear Cobalt(II) SMM Candidates	69
6.	Multiconfigurational Calculations on Lanthanide(III) SMMs	77
6.1.	Noteworthy Examples	79
6.2.	Dy(III) and Er(III) Complexes with Triaminoguanidine-Based Ligands	80
6.2.1.	CASSCF/RASSI-SO Calculations on Dy(III) and Er(III) Complexes	82
6.2.2.	Simulations of $\chi_M T$	89
7.	BS-DFT Calculations on Oligonuclear Transition Metal Complexes	95
7.1.	Exchange Coupling in Cu ₄ O ₄ Cubanes with Sugar-Ligands	95
7.1.1.	4+2 Cubanes	99
7.1.2.	2+4 Cubanes	103
7.2.	Hexanuclear Copper(II) Metallacrown with Hydronium Guests	105
7.2.1.	Magnetic Properties	108

7.2.2. Broken-Symmetry DFT calculations	111
7.3. Ferromagnetic Trinuclear Chromium(III) Complexes	116
7.3.1. Energy Spectrum of $[\text{Cr}_3(\text{TAG}^{\text{R}})(\text{bipy})_3(\text{Cl})_3]\text{Cl}$	117
7.3.2. Broken-Symmetry DFT Calculations	118
8. Conclusion	123
9. Zusammenfassung	127
III. Experimental Part	131
10. Physical Measurements	133
10.1. Instruments	133
10.2. Crystal Structure Determination	134
11. Computational Details	135
11.1. Broken-Symmetry Calculations	135
11.2. Multiconfigurational Calculations	135
12. Synthesis	137
12.1. Materials	137
12.2. Preparation	137
Appendix	143
A. Structural Details	145
A.1. Carbazole-Based Complexes	145
B. Crystallographic Details	151
C. Continuous Shape Measures	157
C.1. Similarities for Co(II) Complexes	158
C.2. Similarities for Dy(III) Complexes	159
D. Additional Details for Quantummechanical Calculations	161
D.1. CASSCF and CASPT2 Calculations on Tetrahedral Cobalt(II) SMMs	161
D.2. Linear Cobalt(II) Complexes	166
D.3. DFT Energies for Calculations on 42	169

Contents

Bibliography	171
Curriculum Vitae	181
Declaration of Originality	183

LIST OF ABBREVIATIONS AND SYMBOLS

Analytical Methods and Devices

CV	cyclic voltammetry
EPR	electron paramagnetic resonance
ESI	electrospray ionization
FAB	fast atom bombardment
IR	infrared
MS	mass spectrometry
NMR	nuclear magnetic resonance
SQUID	superconducting quantum interference device
TGA	thermogravimetric analysis
UV	ultraviolet
VIS	visible

Chemicals and Moieties

<i>t</i> Bu	<i>tert</i> -butyl
Ac	acetyl
bipy	2,2'-bipyridine
Bn	benzyl
crypt-222	[2.2.2]cryptand
Ln	lanthanide
Me	methyl
MeOH	Methanol

List of Abbreviations and Symbols

Naph	naphthyl
Ph	phenyl
<i>i</i> Pr	<i>iso</i> -propyl
TAG	triaminoguanidine
thf	tetrahydrofuran

Crystal Structures

CShM	continuous Shape Measure
BTPR-8	biaugmented trigonal prism
SAPR-8	square antiprism
SP-4	square-planar
SS-4	seesaw
T-4	tetrahedron
TDD-8	triangular dodecahedron
$\Phi_{P1 \rightarrow P2}$	angular fraction on the minimal distortion pathway between the polyhedra <i>P1</i> and <i>P2</i>

IR Spectroscopy

$\tilde{\nu}$	wave number
ar	aryl
ATR	attenuated total reflectance
b	broad
m	medium
s	strong
vs	very strong
w	weak

Magnetism

<i>A</i>	hyper-fine constant
----------	---------------------

α	distribution width (ac SQUID measurements)
ac	alternating current
AFM	antiferromagnetic
χ_0	isothermal susceptibility
χ_M	molar magnetic susceptibility
χ'_M	in-phase susceptibility
χ''_M	out-of-phase susceptibility
χ_S	adiabatic susceptibility
χ_{TIP}	temperature-independent paramagnetism
D	axial zero-field splitting parameter
dc	direct current
E	rhombic zero-field splitting parameter
g	g -tensor
H	external magnetic field
\hat{H}	Hamiltonian
HS	high-spin
FM	ferromagnetic
I	nuclear spin quantum number
\hat{I}	nuclear spin operator
J	exchange interaction parameter (Chapters 1, 3 and 7)
	angular momentum quantum number associated with \hat{J}^2 (Chapter 6)
\hat{J}	total angular momentum operator
λ	intermolecular interaction
LIESST	light induced excited spin state trapping
KD	Kramers doublet
M	magnetization

List of Abbreviations and Symbols

M_J	angular momentum quantum number associated with \hat{J}_z
M_L	orbital quantum number associated with \hat{L}_z
M_S	spin quantum number associated with \hat{S}_z
MFT	molecular field theory
$\boldsymbol{\mu}$	vector of the magnetic momentum
μ_B	Bohr magneton
ω	frequency of the ac field
QTM	quantum tunneling of magnetization
ρ	molar fraction of paramagnetic impurity
SMM	single molecule magnet
S	spin quantum number associated with \hat{S}^2
\hat{S}	spin operator
\hat{S}_z	z -component of the spin operator
τ_c	relaxation time
TAQT	thermally assisted quantum tunneling
U_{eff}	spin reversal barrier
ZFS	zero-field splitting
NMR Spectroscopy	
δ	chemical shift
d	doublet
m	multiplet
s	singlet
Theoretical methods	
BS	broken symmetry
CASSCF	complete active space self-consistent field
CASPT2	complete active space perturbation theory to 2nd order

CI	configuration interaction
COT	corresponding orbital transformation
CSF	configuration state function
DFT	density functional theory
DKH	Douglas-Kroll-Hess Hamiltonian
HF	Hartee-Fock
FCI	full configuration interaction
KS	Kohn-Sham
LCAO	linear combination of atomic orbitals
MCSCF	multiconfigurational self-consistent field
MO	molecular orbital
NEVPT2	n-electron valence state perturbation theory to 2nd order
QDPT	quasi-degenerate perturbation theory
RASSCF	restricted active space self-consistent field
RASSI	restricted active space state interaction
ρ	electron density probability
SO	spin-orbit
SOMO	singly occupied molecular orbital
ZORA	zeroth-order regular approximation

Part I

Introductory Part

INTRODUCTION

1.1. Challenges in Information Technology

Since the invention of transistors in the 1940s and their utilization in integrated circuits, miniaturization with respect to new production processes led to an exponential growth of the number of sheeted transistors per processing unit, commonly known as Moore's law.^[1,2] Thereby, also the computational power of microprocessors used for scientific, business, military or intelligence purposes made a huge leap forward. While the 22 nm technology is established at the moment and new lithography processes (extreme ultraviolet lithography, multiple patterning) are in principle able to achieve much smaller structures, future miniaturization will face problems due to tunneling effects for source-drain distances below 5 nm.^[3] Similar problems will be encountered for magnetic data storage systems. Commercially available hard disks exhibit storage densities of 1 Tbit/in², implying elementary magnetic registers of $\approx 100 \text{ nm}^2$ size.^[4] Recent jumps in storage density were achieved by perpendicular magnetic recording^[5] and shingled magnetic recording,^[6] while further improvements are still developed (heat-assisted^[7] and bit-patterned^[8] techniques). However, ongoing shrinking of the magnetic cells might also reach the superparamagnetic limit of materials with larger coercivities and smaller grain sizes, respectively.^[7]

These challenges demand completely fresh approaches. One idea for new computer architectures possible with further miniaturization are so-called quantum computers, as first suggested in the 1980s by Feynman^[9] amongst others. Quantum computers are made up of quantum bits (Qubits), that have to suffice the criteria formulated by DiVincenzo,^[10] and may exist in two states $|0\rangle$ and $|1\rangle$. In contrast to classical bits,

1. Introduction

Qubits are also able to exist in superpositions $|\Psi\rangle = c_0|0\rangle + c_1|1\rangle$ of the state vectors. Furthermore, entanglement of several Qubits forming quantum registers leads to new basis vectors $|00\rangle, |01\rangle, |10\rangle, |11\rangle$ (for the case of two Qubits), that cannot be decomposed into states of single Qubits. Particular strengths of quantum computers lie at completely different algorithms possible to be effectively implemented. Shor's algorithm^[11] challenges asymmetric encryption algorithms, that depend on integer factorization (i.e. the RSA cryptosystem*). An ideal implementation should be able to significantly reduce the computation times for such problems. Furthermore, database queries might be substantially accelerated by the randomized algorithm proposed by Grover.^[12,13] However, a recent benchmark of a commercially available 512 Qubit quantum computer[†] did not yield any speedups compared to conventional computers.^[14] Over the years, numerous implementations for Qubits were suggested. Some proposed systems for Qubits originate from the field of molecular magnets, challenging the field of magnetochemistry. Possible implementations might be realized with single-molecule magnets (SMMs),^[15] antiferromagnetically coupled systems with an odd number of spin carriers^[16,17] or spin frustrated molecules.^[18,19]

For the storage of data, basically every bistable system which can be read and written, and exhibits a sufficient stability of the storage, might be used. FePt nanoparticles with a 3 nm diameter, for instance, show the largest magnetocrystalline anisotropy known so far.^[4] On the molecular level, especially iron complexes are known for spin crossover (SCO) behavior, describing a change of the ground state multiplicity.^[20] Also, SMMs might be useful for this application.^[21]

The outstanding magnetic properties putting these molecular species in the spotlight arise from the interactions within the distinct paramagnetic metal ions and/or from interactions between them. In the next section, major influences on the magnetic behavior of chemical systems are outlined.

1.2. Magnetism of Paramagnetic Ions

Magnetism is a quantum mechanical effect, that arises from unpaired electrons. These may be found in the metal ions from the d- and f-block of the PSE as well as in certain stable radicals (e.g. the triphenylmethyl radical or nitroxide radicals). The electrons afford a magnetic moment due to their spin of $s = \frac{1}{2}$. Unfortunately, the prediction of

*Named after the inventors Ron Rivest, Adi Shamir, and Leonard Adleman.

†www.dwavesys.com

Table 1.1.: Estimated magnitudes of the interactions in paramagnetic ions of d- and f-elements.^[22]

Interaction	System	Energy Equivalent [cm ⁻¹]
\hat{H}_{ee}	3d, 4d, 5d	3d > 4d > 5d $\approx 10^4$
	4f, 5f	4f > 5f $\approx 10^4$
\hat{H}_{LF}	3d, 4d, 5d	3d < 4d < 5d $\approx 2 \cdot 10^4$
	4f	$\approx 10^2$
	5f	$\approx 10^3$
\hat{H}_{SO}	3d, 4d, 5d	3d < 4d < 5d $\approx 10^3$
	4f, 5f	4f < 5f $\approx 10^3$

magnetic properties is not intuitive, and many aspects have to be considered, of which the most important are explained in this section.

1.2.1. Electronic Structure of Paramagnetic Ions

There are different quantum mechanical effects, that have an influence on the electronic structure of paramagnetic ions, and therefore, on their magnetic properties. With respect to the position of the paramagnetic ion in the periodic system of elements, the order and magnitude of the distinct effects may vary. Below, the most important interactions in the ground state are briefly explained. Estimated magnitudes according to Lueken^[22] are listed in Table 1.1. Visual representations of the resulting energy spectra are shown in Fig. 1.1 utilizing the model system cobalt(II) and dysprosium(III) due to their importance in this work.

Electron-Electron Interaction The interelectronic interaction, \hat{H}_{ee} , shows the largest impact on the electronic structure for most of the d- and f-ions. It results in the splitting into energy terms defined by the total spin S and the orbital momentum L , with the ground term predicted by the first and second Hund's rule for ideal (spherical) symmetry of the ion.^[23,24]

Ligand Field The ligand field interaction, \hat{H}_{LF} , is caused by the interelectronic repulsion between the electrons of the metal ion and the ligands. Depending on the symmetry of the coordination environment, orbital degeneracies are lifted completely or just to a certain degree, and, thus, requirements for strong spin-orbit interaction may

1. Introduction

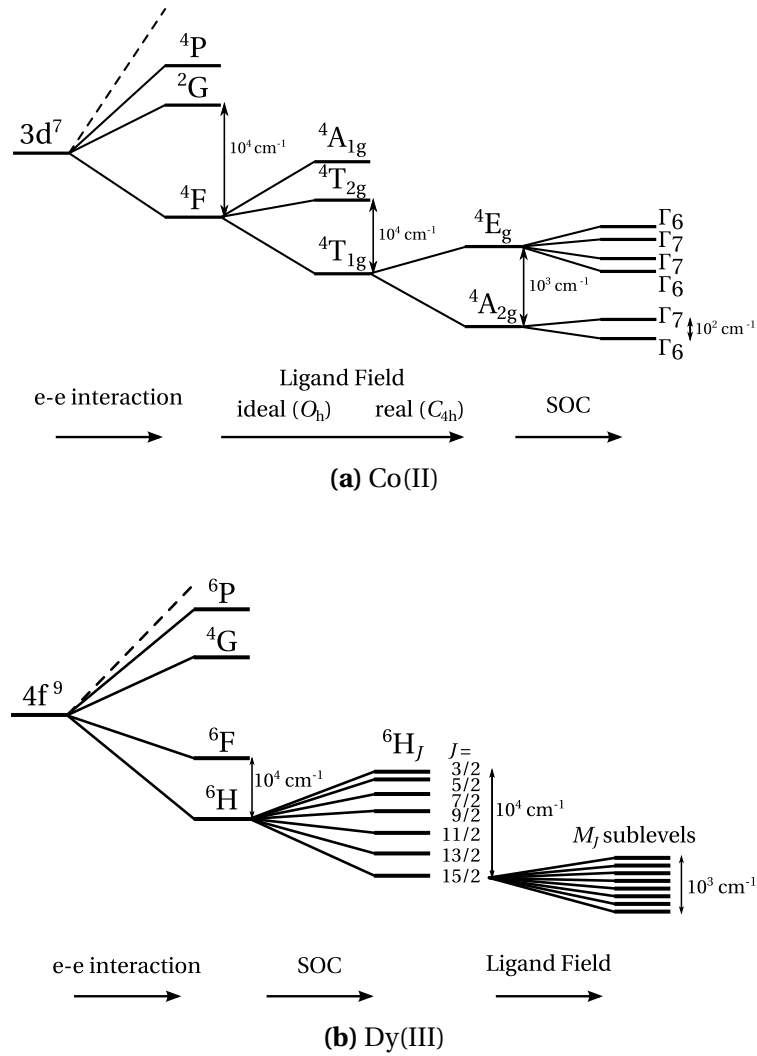


Figure 1.1.: Electronic structure of the Co(II) and Dy(III) ions with sequential perturbations of interactions with decreasing magnitude. For Co(II), an elongated O_h environment was assumed, where Γ_6 and Γ_7 denote the $M_S = \pm \frac{1}{2}$ and $\pm \frac{3}{2}$ doublets, respectively.

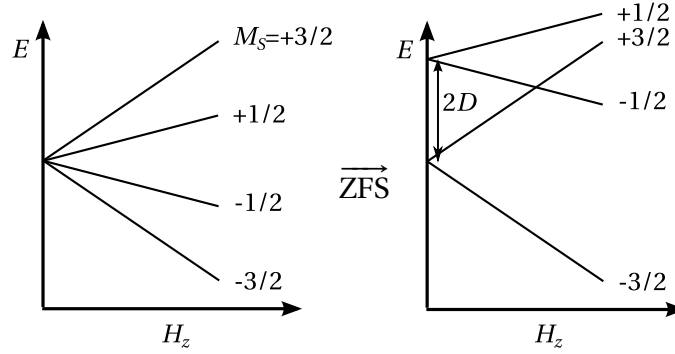


Figure 1.2.: Effect of ZFS on the energy of the Zeeman states in a $S = \frac{3}{2}$ system.

be met or denied. The stronger the repulsion between the electrons, the larger the ligand field splitting becomes. The magnitude of \hat{H}_{LF} increases within the row $3d < 4d < 5d$, giving rise to a low-spin ground state for the majority of 4d and 5d complexes.

Spin-Orbit Coupling The spin-orbit coupling (SOC) term, \hat{H}_{SO} , results from the interaction of the electron spin with the orbital momentum of its orbit function. It originates from relativistic quantum mechanics and causes a shift or splitting of the ligand field states. In the case of 4f ions, its influence is even larger than \hat{H}_{LF} , which is illustrated by the interchanged order of perturbation shown in Fig. 1.1b for Dy(III). For orbitally non-degenerated ground states with $S \geq 1$, the interaction resulting from second-order SOC is called zero-field splitting (ZFS) and may lift the degeneracy of the $|M_S\rangle$ states of a given S multiplet. The effect on the energies of the Zeeman states is described in the spin Hamiltonian formalism by

$$\hat{H} = D \left[\hat{S}_z^2 - \frac{1}{3} S(S+1) \right] + E \left[\hat{S}_x^2 - \hat{S}_y^2 \right], \quad (1.1)$$

where D is the axial and E is the rhombic ZFS parameter. The influence of D is depicted in Fig. 1.2, whereas the effects of the rhombic parameter E are more complicated. The fraction $\frac{E}{D}$ is the rhombicity and has to be in the range $0 \geq \frac{E}{D} \geq \frac{1}{3}$ according to its definition.

Zeeman Effect Interaction of the magnetic field and the M_S states is described by the Zeeman effect. The energy of M_S levels changes according to

$$\hat{H}_{ZE} = g\mu_B \mathbf{H} \hat{S}, \quad (1.2)$$

1. Introduction

where g is the g -tensor and \mathbf{H} the external magnetic field. Depending on the electron configuration, g may be isotropic ($g_x = g_y = g_z$), axial ($g_x = g_y \neq g_z$), or rhombic ($g_x \neq g_y \neq g_z \neq g_x$). The free electron exhibits $g_e = 2.0023$, whereas it may vary widely for paramagnetic ions. Deviations from the free-electron value are caused by SOC. The M_S state energies with respect to the Zeeman effect without and with ZFS for an $S = \frac{3}{2}$ system are shown in Fig. 1.2.

1.2.2. Cooperative Effects Between Paramagnetic Ions

Many macroscopic magnetic phenomena can only be explained, if the interaction between paramagnetic centers is accounted for. If the overall interaction between magnetic moments results in a parallel alignment (see Fig. 1.3a), a ferromagnetic phase is obtained. They exhibit a complex behavior in the magnetic field and show hysteresis effects in the M vs. H plot below the Curie temperature T_C . Above T_C , paramagnetic behavior obeying the Curie or Curie-Weiss law^[25] shown in Eqs. (1.3) and (1.4), respectively, is observed.

$$\chi_M = \frac{C}{T} \quad (1.3)$$

$$\chi_M = \frac{C}{T - \Theta_p} \quad (1.4)$$

Antiferromagnetism is observed, when interaction between magnetic moments yield (speaking in classical terms) antiparallel alignment (see Fig. 1.3b) with a resulting magnetic moment of zero. The transition to Curie(-Weiss) behavior is possible in the same manner as for ferromagnets above the Néel temperature T_N . When two ferromagnetic sublattices with different magnetic moments undergo antiferromagnetic interaction

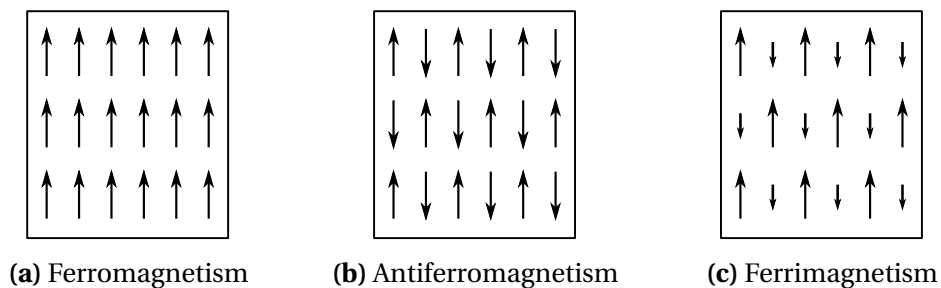


Figure 1.3.: Cooperative effects between permanent magnetic moments in the solid state.

between those two sublattices, the overall magnetic moment does not vanish. Such ferrimagnetic phases (e.g. magnetit) were the first observed evidence of magnetism due to the forces between them and iron.^[26]

In molecular species, cooperative effects are treated with an exchange term in the spin Hamiltonian. While in literature, the expressions $-J\hat{S}_1\hat{S}_2$, $-2J\hat{S}_1\hat{S}_2$, and $J\hat{S}_1\hat{S}_2$ are mentioned,^[22] in this work, only the first form is used.

1.3. Recent Areas of Interest in Magnetochemistry

The aforementioned phenomena applicable in future information technology will be shortly reviewed. Due to the utter importance of SMMs in this work, they will receive the most attention. Spin frustrated systems are also explained due to the systems encountered in Sections 7.2 and 7.3, which are closely related to research in this area. Although no SCO systems were investigated in this work, recently, such complexes have received considerable attention, and, therefore, a few basics are presented.

1.3.1. Single-Molecule Magnets

A thermal barrier for the reversal of the magnetic moment is normally observed for regular permanent magnets, demanding ferromagnetic behavior in a magnetic domain of several thousands of paramagnetic centers. Thus, it was very surprising to find an out-of-phase signal during dynamic susceptibility measurements for $[\text{Mn}_{12}\text{O}_{12}(\text{AcO})_{16}(\text{H}_2\text{O})_4] \cdot 2\text{AcOH} \cdot 4\text{H}_2\text{O}$,^[28] which at that time was already known for several years.^[29] More oligonuclear manganese carboxylate complexes with SMM behavior became known a short while afterwards.^[30] SMMs involving iron, nickel, cobalt and vanadium were also reported,^[31] while the first mononuclear SMMs contained terbium(III) ions, whose S_8 -symmetric complexes still exhibit the largest reported spin reversal barriers.^[32–35] Closely related complexes paved the road for the next successes in this research area. Recent examples of Co(II) and lanthanide(III) SMMs are shortly reviewed in the Chapters 4 and 6, respectively.

Spin-orbit interactions within single ions or ferromagnetically coupled clusters manifest as ZFS. Therefrom, a double-well potential of $|M_S\rangle$ states[‡] is created. The energy ladder of the double-well potential is depicted in Fig. 1.4 without and with an applied external field. Ideally, only thermal relaxation should occur to obtain large

[‡]Or $|M_J\rangle$ states, depending on which quantum numbers are better suited for the situation.

1. Introduction

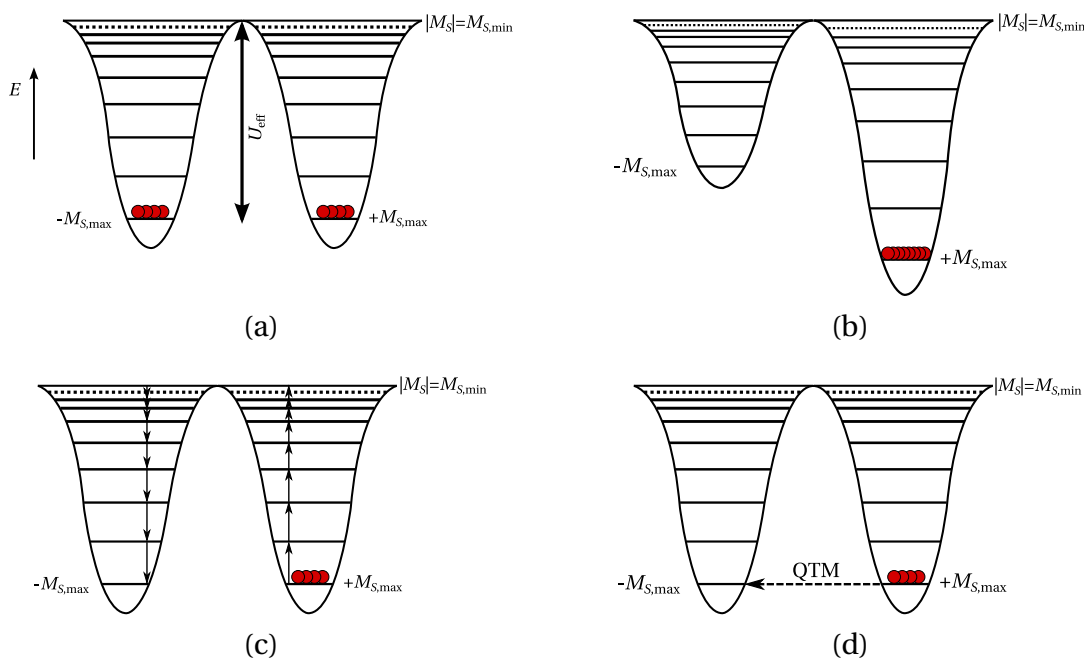


Figure 1.4.: Double-well potential seen by the spin resulting from magnetic anisotropy and possible relaxation pathways. The underlying theory of the double-well potential in SMM was published by Leuenberger and Loss.^[15,27] (a) Without external stimuli, the magnetic moments are aligned statistically. (b) Upon application of an external magnetic field, one direction of the magnetic moment is preferred, and this $+M_S$ state is populated. (c) Removing the external field may result in thermal relaxation processes over the barrier U_{eff} . (d) Under certain requirements, also tunneling processes are observed.

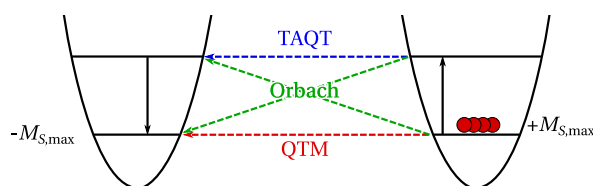


Figure 1.5.: Important relaxation processes in single-molecule magnets between the lowest $|M_S\rangle$ states.

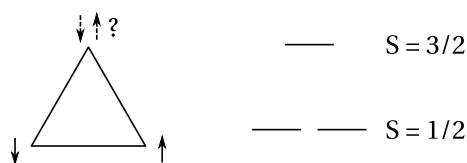


Figure 1.6.: Schematic representation of a frustrated system of three $S = \frac{1}{2}$ spins. The result is a twofold degenerated $S = \frac{1}{2}$ ground state, as depicted on the right.

spin reversal barriers. In real compounds, however, relaxation of the magnetization between the lowest spin-orbit states by tunneling is also often found (quantum tunneling of magnetization, QTM). The relaxation kinetics of the tunneling processes do not depend on the temperature, whereas the kinetics of thermal processes do. Combination of thermal and tunneling processes leads to thermally assisted quantum tunneling (TAQT) (see Fig. 1.5). Transitions between $|M_{S,\max}\rangle \rightarrow |\pm M_{S,\max+1}\rangle$ are called Orbach processes. Both these processes depend on the energy separation between the lowest and the first excited $|M_S\rangle$ state.

Large barriers are obtained, when the mixing of different $|M_S\rangle$ states is prevented due to an ideal rotation symmetry. Otherwise, large transversal elements of the g -tensor occur and open tunneling pathways. However, the best-suited coordination environment for achieving a permanent magnetization heavily depends on the properties of the ion itself. For example, lanthanides do exhibit different spatial electron distributions for the $|M_{J,\max}\rangle$ state, demanding different geometries for a large separation of the ground state, which is explained in more detail in Chapter 6.

1.3.2. Spin-Frustration

For molecular species with competing magnetic interactions, a situation may arise, that does not suffice the preferred alignment of the involved local spins. The most simple example might be an equilateral triangle of $S = \frac{1}{2}$ spins, that interact antiferromagnetically. As depicted in Fig. 1.6, this gives rise to a situation, where (in the classical picture) not all spins can be aligned antiparallel, and, hence, frustration is achieved. Half-integer spins will then give rise to an orbitally degenerated ground state with $S = \frac{1}{2}$, while for integer spins, the magnetic moment of the resulting ground state vanishes. Thus, according to Kahn,^[36] only the former case should explicitly named spin-frustration. For Cu_3 triangles, antisymmetric and anisotropic exchange interactions are necessary for the correct description of the electronic structure, illustrating the non-triviality of such systems.^[37] A very promising candidate was prepared in

1. Introduction

our group by Zharkuskaya,^[38] utilizing triaminoguanidine-based ligands to obtain C_3 -symmetric copper(II) complexes.

1.3.3. Spin-Crossover

Ions with d^4 - d^7 configurations are known to exist as high-spin or low-spin systems with respect to the ligand field strength of the employed ligands. While most ligands are associated with a distinctive spin state, some, mainly polydentate, ligands tend to generate ligand field strengths of intermediate size. Odd magnetic behavior upon thermal stimuli was reported as early as 1931 by Cambi and Szergö for dithiocarbamate complexes of iron(II).^[39] A crucial influence of the axial ligands on the magnetic moment of iron heme complexes was found by Pauling a few years later.^[40] The nature of this properties was clarified by Mößbauer spectroscopy,^[41] finding that the ground state multiplicity changes, and thus, also the structure of the complexes (i.e. ionic radius of the metal). The average metal-ligand bond length is in general shorter for the low-spin state than for the high-spin state. Later, also stimulation by pressure^[42] and light^[43,44] was found to induce spin-crossover. Under certain circumstances, also cooperative effects play a significant role, potentially yielding bistable systems with hysteresis effects (e.g.^[45-49]).

1.4. Aims of this Work

In this work, several aspects of the above mentioned systems were considered. Based on the work of Eike T. Spielberg^[19,50] about carbazole-based ligands for transition metal complexes, new ligands with potential photoreactivity will be designed and synthesized. As presented in Chapter 3, also the synthesis and magnetic properties of complexes of these ligands with transition metal ions will be investigated.

In the other parts of this work, quantum mechanical methods will be employed to clarify the magnetic behavior and its origin of numerous magnetic compounds connected to different recent synthetical results. The theoretical methods used are explained in Chapter 2. One major goal is the calculation of energies and g -tensors of the spin-orbit states for several classes of SMM candidates. Therefore, the multiconfigurational CASSCF method in addition with the RASSI-SO method will be used. In Chapter 4, the focus will lie on tetra-coordinated Co(II) complexes described in Chapter 3, and some of those reported by Buchholz^[51] and Ziegenbalg^[52] as well as a few

more. These complexes will also be investigated concerning the structural influences on the ZFS parameters. Inspired by recent results of Zadrozny,^[53] different linear Co(II) complexes from approximately 20 years of literature will be calculated in Chapter 5 to possibly identify high-performing SMM candidates. Complexes of the metal ions with the probably largest growth of confirmed SMMs, the lanthanides, will be studied in Chapter 6. Properties of the dysprosium(III) and erbium(III) complexes with triaminoguanidine (TAG) based ligands prepared by Schuch^[54] and Möller^[55] showed large spin reversal barriers, and, hence, their spin-orbit spectrum will be calculated. For complexes with hydrogen-bridged dimers present in the crystal structure, the interactions between the lanthanide(III) ions are an interesting aspect to look into.

Finally, in Chapter 7, several exchange coupled system will be theoretically investigated in order to gain insight into the exchange interactions between transition metal ions. This task will be performed within the *broken-symmetry* formalism. Cu_4O_4 cubanes prepared by Burkhardt^[56] under the premise of exploring the coordination properties of sugar-based ligand systems with a possible magnetochiral effect will be studied in Section 7.1. In Section 7.2, a long-known metallocoronate with H_3O^+ guest molecules^[38] will be reinvestigated, since its magnetic properties still leave some questions unsolved. Trinuclear chromium(III) complexes with the TAG ligand yield ferromagnetic exchange, as reported by Schuch^[54], and will be calculated in Section 7.3.

THEORETICAL METHODS

In general, *ab initio* methods are based exclusively on the laws of quantum mechanics without involving any empirical parameters except for the natural constants. Methods addressing the electronic ground state usually aim to solve the time-independent Schrödinger equation $\hat{H}_{\text{eff}}\Psi_{\text{el}} = E_{\text{el}}\Psi_{\text{el}}$ with $\hat{H}_{\text{eff}} = \hat{H}_{\text{el}} + V_{\text{nn}}$ by constructing a minimum energy wave function Ψ and finding its energy eigenvalue E . All methods discussed below are treated within the Born-Oppenheimer approximation,^[57] which separates the nuclear wave function from the electronic wave function. The electronic non-relativistic Hamiltonian for many-electron systems is then given by:

$$\hat{H}_{\text{el}} = -\frac{1}{2} \sum_i \nabla_i^2 - \sum_i \sum_{\alpha} \frac{Z_{\alpha}}{r_{i\alpha}} + \sum_i \sum_{j>i} \frac{1}{r_{ij}}. \quad (2.1)$$

For *ab initio* methods, the Hamiltonian is known within the chosen approximations. The task is then to find an eigenfunction of \hat{H}_{el} , the electronic wave function Ψ_{el} . The Pauli principle^[58] demands an antisymmetric wave function, which is satisfied by using the antisymmetrized product of one-electron wave functions (also called spin orbitals) χ_i , known as Slater determinant Φ_{SD} for N electrons in the general form:

$$\Phi_{\text{SD}} = \frac{1}{\sqrt{N!}} \begin{vmatrix} \chi_1(\mathbf{x}_1) & \chi_2(\mathbf{x}_1) & \cdots & \chi_N(\mathbf{x}_1) \\ \chi_1(\mathbf{x}_2) & \chi_2(\mathbf{x}_2) & \cdots & \chi_N(\mathbf{x}_2) \\ \vdots & \vdots & \ddots & \vdots \\ \chi_1(\mathbf{x}_N) & \chi_2(\mathbf{x}_N) & \cdots & \chi_N(\mathbf{x}_N) \end{vmatrix}. \quad (2.2)$$

2. Theoretical Methods

The spin orbitals are products of the spatial orbital $\psi(\mathbf{r})$ and a spin wave function:

$$\chi_i(\mathbf{x}_j) = \begin{cases} \psi_i(\mathbf{r}_j) \cdot \alpha(\omega_j) \\ \psi_i(\mathbf{r}_j) \cdot \beta(\omega_j) \end{cases} \quad (2.3)$$

For open shell systems, eigenfunctions of the Hamiltonian are not necessarily single Slater determinants, but linear combinations thereof. The linear combinations, that are eigenfunctions are also called configuration state functions (CSF). For closed-shell calculations, a single Slater determinant by definition is a CSF.

Hartree-Fock theory is one way to calculate and minimize the energy of a Slater determinant. It is explained briefly to illustrate important concepts immanent to all *ab initio* methods. Furthermore, one concept for the calculation of correlation energy is explained utilizing the configuration interaction method. Thereafter, the multiconfigurational CASSCF method and the multireference CASPT2 method are outlined in a compact form, since they were used to obtain a significant part of the results of this work.

2.1. *Ab initio* Methods

2.1.1. Hartree-Fock Approximation

The Hartree-Fock approximation^[59,60] is a way to minimize the energy of a wave function in the form of a single Slater determinant.^[60] By the application of the variational principle for minimizing the energy of the determinant in Eq. (2.2), the Hartree-Fock equations are obtained:

$$\hat{f}(\mathbf{x}_i) |\chi(\mathbf{x}_i)\rangle = \epsilon |\chi(\mathbf{x}_i)\rangle, \quad (2.4)$$

that lead to the one-electron wavefunctions $|\chi(\mathbf{x}_i)\rangle$ for the electrons i and their eigenvalues ϵ . The Fock operator $\hat{f}(\mathbf{x}_i)$ is defined by the one-electron operator $\hat{h}(\mathbf{x}_i)$ and the two-electron operators $\hat{J}_\mu(\mathbf{x}_i)$ (Coulomb operator) and $\hat{K}_\mu(\mathbf{x}_i)$ (exchange operator):

$$\hat{f}(\mathbf{x}_i) = \hat{h}(\mathbf{x}_i) + \sum_{\mu=1}^N (\hat{J}_\mu(\mathbf{x}_i) - \hat{K}_\mu(\mathbf{x}_i)) \quad (2.5)$$

with

$$\hat{h}(\mathbf{x}_i) = -\frac{\hbar}{2}\nabla^2 - \frac{1}{4\pi\epsilon_0} \sum_{n=1}^{N_{\text{nuc}}} \frac{Z_n e^2}{|\mathbf{r}_i - \mathbf{R}_n|}, \quad (2.6)$$

$$\hat{J}_\mu(\mathbf{x}_i) |\chi_v(\mathbf{x}_i)\rangle = \left\langle \chi_\mu(\mathbf{x}_j) \left| \frac{1}{|\mathbf{r}_1 - \mathbf{r}_2|} \right| \chi_\mu(\mathbf{x}_j) \right\rangle |\chi_v(\mathbf{x}_i)\rangle, \quad (2.7)$$

$$\text{and } \hat{K}_\mu(\mathbf{x}_i) |\chi_v(\mathbf{x}_i)\rangle = \left\langle \chi_\mu(\mathbf{x}_j) \left| \frac{1}{|\mathbf{r}_1 - \mathbf{r}_2|} \right| \chi_v(\mathbf{x}_j) \right\rangle |\chi_\mu(\mathbf{x}_i)\rangle. \quad (2.8)$$

Since \hat{J}_μ and \hat{K}_μ depend on the wave functions $|\chi_v(\mathbf{x}_i)\rangle$, these equations are not linear and have to be solved with an iterative procedure. For atoms, the Hartree-Fock equations may be solved numerically, whereas for molecular systems, no practical procedures are available. Therefore, Roothaan proposed the use of atomic basis function ϕ_μ , from which the spatial part of the MOs ψ_i are constructed using the linear combination of atomic orbitals (LCAO) ansatz.^[61]

$$|\psi_i(\mathbf{r}_j)\rangle = \sum_{\mu=1} c_{\mu i} |\phi_\mu(\mathbf{r}_j)\rangle. \quad (2.9)$$

Usually, either Slater-Type-Orbitals (STOs) or Gaussian-Type-Orbitals (GTOs) are employed in molecular calculations, but due to the computational advantages of GTOs, most quantum chemical codes use these basis functions. When the basis set expansion is introduced into the Hartree-Fock equation in Eq. (2.4) and the closed-shell case is implied (equal number of α - and β -electrons), the Roothaan-Hall equations may be formulated in matrix notation^[61,62]:

$$\mathbf{FC} = \mathbf{SC}\epsilon. \quad (2.10)$$

The matrices will have $K \cdot K$ elements with respect to the number K of basis functions. For an N electron system, the $\frac{N}{2}$ MOs with the lowest energy will be doubly occupied, while the remaining $K - \frac{N}{2}$ orbitals are unoccupied (also called virtual orbitals). The elements of the Fock matrix \mathbf{F} are given by

$$F_{ij} = \langle \phi_i(\mathbf{r}) | \hat{f}(\mathbf{r}) | \phi_j(\mathbf{r}) \rangle, \quad (2.11)$$

those of the overlap matrix \mathbf{S} by

$$S_{ij} = \langle \phi_i(\mathbf{r}) | \phi_j(\mathbf{r}) \rangle, \quad (2.12)$$

2. Theoretical Methods

and coefficient matrix C has the form

$$C_{ij} = \begin{pmatrix} C_{11} & C_{12} & \cdots & C_{1K} \\ C_{21} & C_{22} & \cdots & C_{2K} \\ \vdots & \vdots & \ddots & \vdots \\ C_{K1} & C_{K2} & \cdots & C_{KK} \end{pmatrix}. \quad (2.13)$$

The elements of the Fock matrix F are sums of integrals involving the one-electron operators and a sum over the coefficients of all occupied MOs multiplied with two-electron integrals. The latter term is often expressed as a product of the density matrix D and the two-electron integrals G :

$$F = h + G \cdot D. \quad (2.14)$$

Diagonalization of F leads to a set of new coefficients to be used in an iterative Self-Consistent Field (SCF) procedure (see Fig. 2.1) until the set of coefficients are converged. These converged coefficients minimize the energy of the Slater determinant. The orbital energies are then found on the diagonal of ϵ :

$$\epsilon_{ij} = \begin{pmatrix} \epsilon_1 & & & 0 \\ & \epsilon_2 & & \\ & & \ddots & \\ 0 & & & \epsilon_K \end{pmatrix} \quad (2.15)$$

The initial set of coefficients is usually obtained from a prior semiempirical calculation (e.g. extended Hückel theory). In the case of a complete basis, the orbital energies would be the exact energies within the HF approximation (HF limit). But due to the computational limitations, only a finite number of basis functions can be used.

A major drawback of this method is the negligence of the correlated motion of the electrons. The electron-electron interaction is treated by the operators \hat{J} and \hat{K} , exposing each electron to an averaged electrostatic field caused by all other electrons. The correlation energy is therefore defined as the difference between the exact electronic energy and the HF limit.

$$E_{\text{corr}} = E_{\text{exact}} - E_{\text{HF}}^{\text{limit}} \quad (2.16)$$

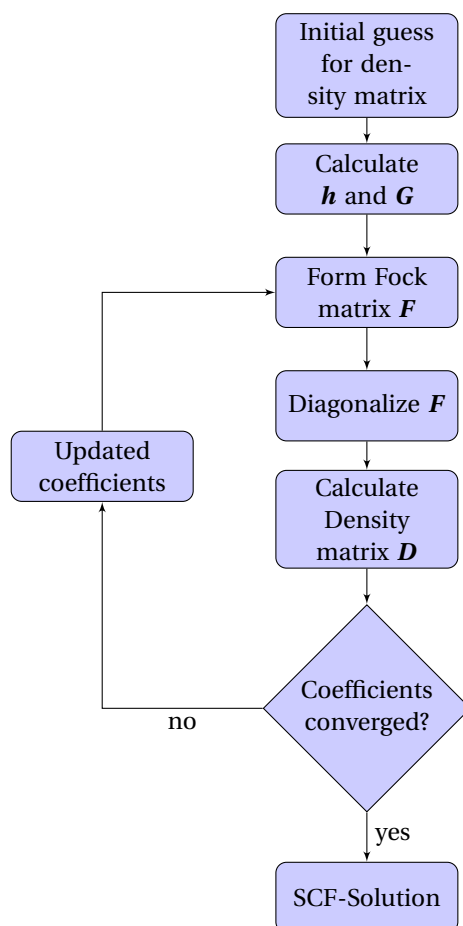


Figure 2.1.: Simplified SCF procedure used in the Hartree-Fock method.

For the correct treatment of electronic correlation, different approaches are available. One of these approaches is the variational Configuration Interaction (CI) method, that includes excited determinants in a linear combination and is further explained below in Section 2.1.2. The multiconfigurational CASSCF approach, closely related to CI, is addressed in Section 2.1.3. A perturbational ansatz is the Møller-Plesset method^[63] (MP2 for perturbation to second order), which includes electron correlation by means of Rayleigh-Schrödinger perturbation theory.^[64] While MP2 is not explained further, the multiconfigurational perturbation method CASPT2^[65] is portrayed in a compact form in Section 2.1.4.

2.1.2. Configuration Interaction

Probably the most straight-forward way of accounting for the correlation energy is the expansion of the wave function into a linear combination of all possible singly, doubly, triply, ... excited configurations, where Ψ_0 is the HF ground state determinant. The variational method optimizing the wave function in such a way is called configuration interaction (CI). a, b, c, \dots and r, s, t, \dots denote excitations from the previously occupied MOs $\psi_a, \psi_b, \psi_c, \dots$ to the virtual MOs $\psi_r, \psi_s, \psi_t, \dots$

$$|\Phi_0\rangle = a_0 |\Psi_0\rangle + \sum_{ar} a_a^r |\Psi_a^r\rangle + \sum_{\substack{a<b \\ r<s}} a_{ab}^{rs} |\Psi_{ab}^{rs}\rangle + \sum_{\substack{a<b<c \\ r<s<t}} a_{abc}^{rst} |\Psi_{abc}^{rst}\rangle + \dots \quad (2.17)$$

For the sake of clarity, the CI expansion can be written in a more compact form.

$$|\Phi_0\rangle = a_0 |\Psi_0\rangle + a_S |S\rangle + a_D |D\rangle + a_T |T\rangle + \dots \quad (2.18)$$

Minimizing the energy of the wave function by optimization of the CI coefficients a_i in Eq. (2.18) leads to a constrained optimization, that can be formulated in a similar fashion as the MO optimization within the HF method. Hence, a very similar eigenvalue problem is obtained. The matrix elements between excitation levels are summarized in the CI matrix as shown in Table 2.1. Between the HF ground state determinant $|\Psi_0\rangle$ and the singly excited CSFs $|S\rangle$, the matrix elements disappear (Brillouin's theorem).^[66] Non-zero matrix elements of $|\Psi_0\rangle$ are only obtained with $|D\rangle$, which should therefore show the largest influence on the CI wave function $|\Phi_0\rangle$. The interaction of the other CSFs with $|\Psi_0\rangle$ is only mediated through off-diagonal elements of $|D\rangle$ with other excited states.

If all possible excitations are accounted for, the method is referred to as full CI (FCI).

Table 2.1.: General Structure of the CI matrix.

	$ \Psi_0\rangle$	$ S\rangle$	$ D\rangle$	$ T\rangle$	$ Q\rangle$...
$\langle\Psi_0 $	$\langle\Psi_0 \hat{H} \Psi_0\rangle$	0	$\langle\Psi_0 \hat{H} D\rangle$	0	0	...
$\langle S $	0	$\langle S \hat{H} S\rangle$	$\langle S \hat{H} D\rangle$	$\langle S \hat{H} T\rangle$	0	...
$\langle D $	$\langle D \hat{H} \Psi_0\rangle$	$\langle D \hat{H} S\rangle$	$\langle D \hat{H} D\rangle$	$\langle D \hat{H} T\rangle$	$\langle D \hat{H} Q\rangle$...
$\langle T $	0	$\langle T \hat{H} S\rangle$	$\langle T \hat{H} D\rangle$	$\langle T \hat{H} T\rangle$	$\langle T \hat{H} Q\rangle$...
$\langle Q $	0	0	$\langle Q \hat{H} D\rangle$	$\langle Q \hat{H} T\rangle$	$\langle Q \hat{H} Q\rangle$...
\vdots	\vdots	\vdots	\vdots	\vdots	\vdots	

In theory, FCI can recover the entire correlation energy when applied with a complete basis. Unfortunately, the number of CSFs increases factorially with the number of basis functions and electrons. With a set of K spatial orbitals and N electrons to be distributed, the rapidly growing number of $\binom{K}{N} = \frac{K!}{N!(N-K)!}$ CSFs has to be considered. Even for moderately sized molecules like water, this generates computational problems with large basis sets. Hence, certain approximations are encountered regularly. Within the frozen-core approximation, excitations from core orbitals are excluded for the construction of CSFs. Different truncated CI methods only allow an arbitrary number of excitations (CISD, CISDT, ...), but suffer from an increasing loss of recovered correlation energy for increasing molecular size. Furthermore, the single-reference CI approach fails, where multiple configurations are necessary to draw a qualitatively correct picture of the electronic ground state.

2.1.3. Complete Active Space SCF Method

The complete active space SCF (CASSCF) method^[67] is a widely used variety of the multiconfigurational SCF (MCSCF) method. The main idea behind MCSCF is the use of wave functions expressed by linear combinations of CSFs $\Phi = \sum_i a_i \Psi_i$, somewhat similar to the CI wave functions in Eq. (2.18), respectively. However, in addition to the variation of the CI coefficients a_i (Eq. (2.18)), the MO coefficients c_i (Eq. (2.9)) are varied simultaneously. To illustrate the nature of a MCSCF wave function, in Eq. (2.19) the ground state wave function of the He atom using two basis functions χ_i ($i = 1, 2$) is shown. Not only does it rely on two CI coefficients a_j ($j = 1, 2$), but also on four MO coefficients c_{ij} .

$$\begin{aligned} \Phi &= a_1 \Psi_1 + a_2 \Psi_2 = a_1 \left| \phi_1 \bar{\phi}_1 \right| + a_2 \left| \phi_2 \bar{\phi}_2 \right| \\ &= a_1 \left| (c_{11}\chi_1 + c_{21}\chi_2) \overline{(c_{11}\chi_1 + c_{21}\chi_2)} \right| + a_2 \left| (c_{12}\chi_1 + c_{22}\chi_2) \overline{(c_{12}\chi_1 + c_{22}\chi_2)} \right| \end{aligned} \quad (2.19)$$

During a regular CI calculation, the MO coefficients of the optimized reference determinant are used for all CSFs. The separate optimization of the MOs for each CSF often leads to a faster convergence for MCSCF than for CI calculations.

To decrease the number of used CSFs, within the CASSCF method, the orbitals are divided into three subspaces: inactive, active, and virtual orbitals (see Fig. 2.2). The inactive orbitals are fully occupied for all included CSFs, whereas all excitations arising from n active electrons in m active orbitals are explicitly treated in a FCI-like way. The

2. Theoretical Methods

size of the active space is denoted as $CAS(n, m)$. Due to the omitted excitations from the inactive orbitals, the method is not appropriate for recovering large fractions of the correlation energy. The correlation treated within the active space arises from electrons that have relatively similar energy and is called the non-dynamical or static correlation. The remaining correlation energy, obtained when more orbitals are included into the CI-expansion, is called the dynamical correlation. Using the CASSCF reference wave function, it may be calculated with variational (MRCI) or perturbational methods (CASPT2).

Later, the CASSCF methodology was extended, yielding the RASSCF (restricted active space SCF) method. It is an approach to enlarge the number of active orbitals without making the number of CSFs unmanageable (see Fig. 2.2, right). Therein, the active orbitals are assigned to the RAS1, RAS2, and RAS3 subspaces with a certain number of allowed holes (RAS1) and excited electrons (RAS3). The RAS2 subspace is equivalent to the active space in the CASSCF methodology.

Despite its shortcomings, CASSCF is especially useful to describe systems, where single-reference methods are not able to draw a qualitatively correct picture. Single-reference methods will fail, when non-equivalent resonance structures are encountered. Benzene for instance can be described by two equivalent resonance structures, and thus, its electronic structure is handled correctly even by HF theory. The ozone molecule is a more challenging example for single-reference methods because ionic

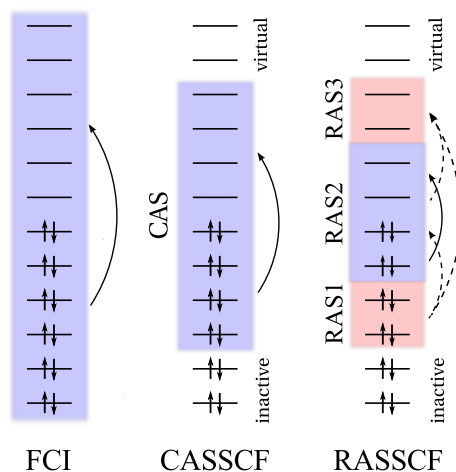


Figure 2.2.: Included excitations for the construction of the CSFs in FCI, CASSCF and RASSCF calculations. For solid arrows, all possible excitations are allowed, whereas for dashed arrows the number of simultaneous excitations is restricted.

and biradical resonance structures are readily formulated. Since the CASSCF method is able to treat excited states, it is also very well suited for electronic structure calculations on 3d- and 4f-elements, which possess a manifold of excited states close to the ground state. Therefore, especially state-averaged CASSCF (SA-CASSCF) is of interest, where averaged MOs are used for all states.

2.1.4. CASPT2 Method

Unfortunately, the scope of the CASSCF method suffers from the maximum number of excitations, which can be treated with reasonable effort. The correlation energy recovered by excitations of electrons distant in energy from the “chemically active” ones in the active space is called dynamical correlation, as stated above. An established method to account for this shortcoming of CASSCF, is the perturbational treatment of these excitations by the CASPT2 method.^[65,68] As found generally for all perturbational methods, the Hamiltonian is defined as a sum of a zeroth-order Hamiltonian \hat{H}_0 and a perturbation \hat{V} :

$$\hat{H} = \hat{H}_0 + \hat{V}, \quad (2.20)$$

where \hat{H}_0 is defined as:

$$\hat{H}_0 = \hat{P}_0 \hat{F} \hat{P}_0 + \hat{P}_{SD} \hat{F} \hat{P}_{SD} + \hat{P}_{TQ} \dots \hat{F} \hat{P}_{TQ} \dots \quad (2.21)$$

and the projection operators \hat{P}_i . $\hat{P}_0 = |\Phi_{\text{CASSCF}}\rangle \langle \Phi_{\text{CASSCF}}|$ is the projection operator with respect to the reference function, whereas \hat{P}_{SD} does the same for single and double excited states. Projections on higher excited states by $\hat{P}_{TQ} \dots$ are omitted in CASPT2. \hat{F} generalized Fock operator:

$$\hat{F} = \sum_{p,q} f_{pq} \hat{E}_{pq} \quad (2.22)$$

with the matrix element f_{pq} for the orbitals $|\psi_p\rangle$ and $|\psi_q\rangle$ and \hat{E}_{pq} being the spin-summed excitation operator (see^[65] for further details). To obtain the second order perturbation, in fact, the first-order wave function $|\Phi_{\text{CASSCF}}^{(1)}\rangle$ has to be known. A similar method as used in MP2 is therefore employed:

$$|\Phi_{\text{CASSCF}}^{(1)}\rangle = \sum_{pqrs} t_{pqrs} \hat{E}_{rs} \hat{E}_{pq} |\Phi_{\text{CASSCF}}\rangle = \sum_k^M c_k |\Phi_{k,\text{CASSCF}}^{(1)}\rangle, \quad (2.23)$$

where \hat{E}_{pq} denotes the annihilation operator for the electrons p and q , and \hat{E}_{rs} denotes

2. Theoretical Methods

the creation operator for the electrons r and s , respectively. The diagonal second-order energies are then obtained as:

$$E_{\text{el,CASSCF}}^{(2)} = - \sum_{k=1}^M \frac{\left| \langle \Phi_{k,\text{CASSCF}}^{(1)} | \hat{V} | \Phi_{\text{CASSCF}} \rangle \right|^2}{\epsilon_k - E_{\text{el,CASSCF}}^{(0)}}. \quad (2.24)$$

The form of the denominator reveals possible problems for states of the first-order interaction space, if ϵ_k gets close to the CASSCF energy $E_{\text{el,CASSCF}}^{(0)}$. These so-called intruder states may be avoided by introducing a level shift ε ,^[69,70] leaving the second-order energy in the form of:

$$E_{\text{el,CASSCF}}^{(2)'} = - \sum_{k=1}^M \frac{\left| \langle \Phi_{k,\text{CASSCF}}^{(1)} | \hat{V} | \Phi_{\text{CASSCF}} \rangle \right|^2}{\epsilon_k - E_{\text{el,CASSCF}}^{(0)} + \varepsilon}. \quad (2.25)$$

Values of $\varepsilon = 0.2\text{-}0.3$ a.u. have proven suitable for transition metal complexes.^[71]

2.2. Density Functional Theory

Many chemists, who are not exclusively working in the field of computational chemistry, which is the vast majority, are nowadays performing calculations on their own to interpret or verify experimental results. Therefore, they usually rely on density functional theory (DFT), as it is nowadays easy to use and yields meaningful results for many applications. This is emphasized by the tremendous increase of works using DFT for understanding reaction mechanisms, prediction of products, calculations of the optical properties, and so on. From less than 100 publications in 1990, 23 years later there are more than 17000 publications per year where density functional theory was mentioned. Probably the main reason for the wide acceptance of DFT is the good description of the electronic structure including correlation effects with the same or less computational costs than *ab initio* Hartree-Fock calculations. In 1998, Walter Kohn was awarded the Nobel Prize in Chemistry (together with John Anthony Pople) for his contributions especially to density functional theory.^[72,73]

2.2.1. Hohenberg-Kohn Theorems and Kohn-Sham Method

When the purely electronic non-relativistic Hamiltonian from Eq. (2.1) is applied to a n -electron wave function, the energy is expressed in terms of one- and two-electron

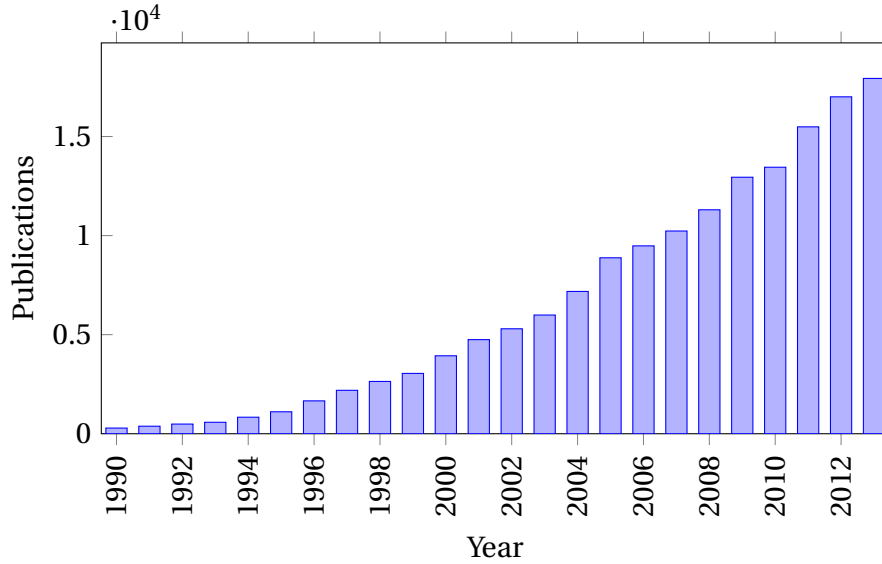


Figure 2.3.: Number of publications with “Density Functional Theory” as a topic. The search was done with CAS Scifinder on July 31st, 2014.

integrals, involving three, respectively six spatial coordinates. In their first theorem,^[74] Pierre Hohenberg and Walter Kohn proved, that for a non-degenerate ground state, the energy and the entire electronic structure are determined by the electron density $\rho_0(x, y, z)$ of the electronic ground state described by only three spatial coordinates. The electronic energy obtained from Eq. (2.1) is the sum of the kinetic energy of the electrons T , the electron-nuclear attraction V_{Ne} , and the electron-electron repulsion V_{ee} . In the case of $\rho_0(x, y, z)$, each of this terms is a functional of ρ_0 :

$$E_0 = E[\rho_0] = T[\rho_0] + V_{Ne}[\rho_0] + V_{ee}[\rho_0] \quad (2.26)$$

The second theorem proven by Hohenberg and Kohn, shows, the inequality $E_0 \leq E_v[\rho_{tr}]$ holds true for all trial density functions ρ_{tr} . Only the “right” electron density ρ_0 will yield the true ground state energy: $E_0 = E_v[\rho_0]$. Thus, the true ground-state electron density will minimize the functional $E_v[\rho_0]$.

The two Hohenberg-Kohn theorems only tell us, that it is possible to calculate the ground-state energy E_0 from the correct electron density ρ_0 , but neither how to find the correct ground-state density, nor, how to calculate the energy from that density. In principal, the method allows to calculate the exact energy, but since the functional is unknown, an approximate functional has to be used, delivering only approximate energies.

A method to obtain ρ_0 and from there finding E_0 was proposed by Walter Kohn and

2. Theoretical Methods

Lu J. Sham.^[75] At first, a reference system of non-interacting electrons (subscript s) is introduced, where all electrons experience the potential $v_s(\mathbf{r}_i)$, that has to influence the electron density $\rho_s(\mathbf{r})$ in such a way, that it becomes equal to the true ground-state density $\rho_0(\mathbf{r})$. For this system, the Hamiltonian can be formulated as

$$\hat{H}_s = \sum_{i=1}^n \left[-\frac{1}{2} \nabla_i^2 + v_s(\mathbf{r}_i) \right] \equiv \sum_{i=1}^n \hat{h}_i^{\text{KS}}. \quad (2.27)$$

Now, also the antisymmetry requirement is met and the ground-state wave function $\Psi_{s,0}$ is the antisymmetrized product of the lowest Kohn-Sham spin-orbitals (Slater determinant) as a product of spatial orbitals θ^{KS} and spin functions σ , with their energies ε^{KS} determined by \hat{h}^{KS} . The electron density is easily obtained by the summation over the square of the KS-orbitals.

$$u_i^{\text{KS}} = \theta_i^{\text{KS}}(\mathbf{r}_i) \sigma_i \quad (2.28)$$

$$\hat{h}_i^{\text{KS}} \theta_i^{\text{KS}} = \varepsilon_i^{\text{KS}} \theta_i^{\text{KS}} \quad (2.29)$$

$$\rho_s = \sum_{i=1}^n |\theta_i^{\text{KS}}|^2 \quad (2.30)$$

To obtain the ground-state energy from the Kohn-Sham spin-orbitals, 2.31 is used. For the deduction of this formula standard text books can be consulted (e.g.^[76]).

$$E_0 = - \sum_{\alpha} Z_{\alpha} \int \rho(\mathbf{r}_1) d\mathbf{r}_1 - \frac{1}{2} \sum_{i=1}^n \langle \theta_i^{\text{KS}}(1) | \nabla_1^2 | \theta_i^{\text{KS}}(1) \rangle + \frac{1}{2} \iint \frac{\rho(\mathbf{r}_1) \rho(\mathbf{r}_2)}{r_{12}} d\mathbf{r}_1 d\mathbf{r}_2 + E_{xc}[\rho] \quad (2.31)$$

The exchange energy as well as the correlation energy are not yet accounted for. They are both included in the term $E_{xc}[\rho]$ and cannot be derived straight-forward. Different approaches for accounting for these energies have been made and the most important examples are given below.

2.2.2. Important Exchange-Correlation Functionals

Local Density Approximation

For the Local Density Approximation (LDA), the electrons are viewed as a uniform electron gas, the exchange energy is then given by the Dirac formula (Eq. (2.32)). The functional of the correlation energy $E_c[\rho]$ was derived by fitting the exact correlation

energy values calculated with quantum Monte Carlo simulations to a set of parameters. The complete expression is rather complicated, but the functional itself became well-known by the initials of three scientist: Vosko, Wilk, and Nussair (2.33).^[77]

$$E_x^{\text{LDA}}[\rho] = -\frac{3}{4} \left(\frac{3}{\pi}\right)^{\frac{1}{3}} \int \rho^{\frac{4}{3}}(\mathbf{r}) d\mathbf{r} \quad (2.32)$$

$$E_c^{\text{LDA}}[\rho] = E_c^{\text{VWN}}[\rho] \quad (2.33)$$

The corresponding unrestricted formulation of LDA is the local spin-density approximation (LSDA), where the α - and β -orbitals are allowed to have different spatial KS orbitals.

General Gradient Approximation

The integrand in 2.32 is only a function of ρ , which is only appropriate for systems with a slowly varying electron density, like the homogenous electron gas. A correction of LSDA for the variation of the electron density is introduced in functionals, that also include gradients of ρ in the integrand. Therefore, these kind of functionals are assigned to the General-Gradient Approximation (GGA) or are called gradient-corrected functionals. One of the most widely used GGA functional is called Becke's 1988 functional, denoted B88.^[78]

$$E_x^{\text{B88}} = E_x^{\text{LSDA}} - b \sum_{\sigma=\alpha,\beta} \int \frac{(\rho^\sigma)^{\frac{4}{3}} \chi_\sigma^2}{1 + 6b\chi_\sigma \ln[\chi_\sigma + (\chi_\sigma^2 + 1)]} d\mathbf{r} \quad (2.34)$$

$$\text{where } \chi_\sigma \equiv \frac{|\nabla\rho^\sigma|}{(\rho^\sigma)^{\frac{4}{3}}} \quad (2.35)$$

The most used correlation functionals include the Lee-Yang-Parr correlation functional (LYP)^[79] and the Perdew 1986 correlation functional (P86).^[80] Combinations of different exchange and correlation functionals found their way to a wide scientific audience and are known under names like BP86 (B88 + P86) and BLYP (B88 + LYP).

Hybrid Functionals

Hybrid functionals additionally introduce a term for the exact Hartree-Fock exchange energy E_x^{HF} . The most popular hybrid functional is without doubt the B3LYP functional (Becke's 3-parameter functional). The exchange energy is formulated as a

2. Theoretical Methods

sum of different percentages of E_x^{LSDA} , E_x^{HF} , and E_x^{B88} , while the correlation part includes E_c^{VWN} and E_c^{LYP} . The complete expression includes three parameters, which were fitted to match the atomization energies of a certain set of molecules ($a_0 = 0.20$, $a_x = 0.72$, $a_c = 0.81$).

$$E_{xc}^{\text{B3LYP}} = (1 - a_0 - a_x)E_x^{\text{LSDA}} + a_0E_x^{\text{HF}} + a_xE_x^{\text{B88}} + (1 - a_c)E_c^{\text{VWN}} + a_cE_c^{\text{LYP}} \quad (2.36)$$

2.2.3. The Broken-Symmetry Formalism

In principle, multiconfigurational *ab initio* methods would also be suitable to calculate the interactions of several paramagnetic ions, and are in fact applied on these systems.^[81] But unfortunately, the active space would be rather large, if all necessary orbitals (d-orbitals of the metal ions, orbitals of the bridging ligands) were included. Hence, the computational limitations demand a more simplified approach. While most magnetically interesting transition metal ions are unsuited for DFT due to their low-lying excited states, methods have been developed to give reasonable results concerning their chemical properties. One of these methods is the Broken-Symmetry approach proposed in the early 80s by Noodleman^[82] for the treatment of magnetic exchange interacting between interaction metal ions.

Dinuclear complexes with two spin sites S_A and S_B may be aligned ferromagnetically in order to give a ferromagnetic ground state spin $S = S_A + S_B$. The Kohn-Sham method describes this state well, since only one determinant is necessary for the construction of the CSF. The antiferromagnetic state, however, demands multiple determinants for a correct description. A system of two centers with each one unpaired electron, for instance, would lead to the CSF

$$\Psi_{\text{AF}} = \frac{1}{\sqrt{2}} \left(\left| a_1 \bar{b}_1 \right| - \left| \bar{a}_1 b_1 \right| \right), \quad (2.37)$$

where a_1 and b_1 are orbitals localized at A and B, respectively. Within DFT, such a state cannot be represented correctly. Noodleman^[82] proposed the broken-symmetry approach, where the calculation of the antiferromagnetic state starts from orbitals obtained from calculations on the ferromagnetic state. The spin coordinate of one converged singly occupied MO (SOMO) η is therefore changed and taken as the starting point:

$$\Psi_{\text{FM}} = \left| (\text{core}) \eta_a \eta_b \right| \longrightarrow \Psi_{\text{BS}}^{\text{guess}} = \left| (\text{core}) \eta_a \bar{\eta}_b \right|. \quad (2.38)$$

It is an easy task to show, that the determinant $\Psi_{\text{BS}}^{\text{guess}}$ always lies energetically above Ψ_{FM} . Applying the variational principle on $\Psi_{\text{BS}}^{\text{guess}}$ yields a more relaxed picture of the unpaired electrons. While the broken-symmetry solution was subject of discussion in the DFT community, regularly, results of almost quantitative agreement with experimental exchange interaction parameters were reported. As stated by Neese,^[83] the strong spin contamination with $\langle \hat{S}^2 \rangle > S(S+1)$ is not a matter of concern, but a requirement in order to obtain the correct influence of the neutral and ionic components of the antiferromagnetic state. To obtain the correct exchange spectrum of the magnetic species under investigation, the energies of the states Ψ_{FM} and Ψ_{BS} have to be mapped onto the states of the spin Hamiltonian. A straightforward approach might see both Ψ_{HS} and Ψ_{BS} as eigenfunctions of \hat{S}_A and \hat{S}_B and map the expectation values of the Born-Oppenheimer Hamiltonian onto the spin Hamiltonian, as suggested by Yamaguchi *et al.*:

$$\begin{aligned} \langle \Psi_{\text{BS}} | \hat{H}_{\text{Spin}} | \Psi_{\text{BS}} \rangle &= -J(\langle \hat{S}^2 \rangle_{\text{BS}} - S_A(S_A+1) - S_B(S_B+1)) \\ &= E_{\text{BS}} = \langle \Psi_{\text{BS}} | \hat{H}_{\text{BO}} | \Psi_{\text{BS}} \rangle \end{aligned} \quad (2.39)$$

$$\begin{aligned} \langle \Psi_{\text{FM}} | \hat{H}_{\text{Spin}} | \Psi_{\text{FM}} \rangle &= -J(\langle \hat{S}^2 \rangle_{\text{FM}} - S_A(S_A+1) - S_B(S_B+1)) \\ &= E_{\text{FM}} = \langle \Psi_{\text{FM}} | \hat{H}_{\text{BO}} | \Psi_{\text{FM}} \rangle. \end{aligned} \quad (2.40)$$

The energy difference is then:

$$E_{\text{BS}} - E_{\text{FM}} = J(\langle \hat{S}^2 \rangle_{\text{FM}} - \langle \hat{S}^2 \rangle_{\text{BS}}), \quad (2.41)$$

as shown by Yamaguchi *et al.*^[84] The case of small subsystem interaction was already formulated by Noodleman in his first works on the broken-symmetry formalism^[82] and may be written as:

$$E_{\text{BS}} - E_{\text{HS}} = JS_{\text{max}}^2. \quad (2.42)$$

The strong interaction limit was advocated by Ruiz *et al.*^[85]:

$$E_{\text{BS}} - E_{\text{HS}} = J(S_1 S_2 + S_2) \quad \text{with } S_1 \leq S_2. \quad (2.43)$$

Corresponding Orbital transformation

Unfortunately, the Kohn-Sham-Orbitals obtained from the broken-symmetry DFT (BS-DFT) calculations are very likely delocalized over a large part of the molecule and are not of much help for the interpretation of the exchange pathway. Also, orbital-symmetry considerations are only helpful in cases not too complicated, but lose their practicalness for low molecular symmetry. Hence, Neese proposed the use of the Corresponding Orbital Transformation (COT)^[86] to localize magnetic orbitals of the broken-symmetry solution.^[87] COT is suited to localize the SOMOs in a way, that gives a chemically more intuitive description. When the transformation of the BS determinant is performed, the corresponding orbitals can be divided into three MO-subspaces:

1. spin-orbitals with a spatial overlap close to 1, essentially containing covalent bonds and non-bonding electron pairs
2. non-orthogonal magnetic spin-orbital pairs (orbitals responsible for the exchange interaction)
3. unpaired α -orbitals, when $S_1 > S_2$.

This procedure has proven to be useful in a number of cases like the theoretical treatment of complexes with non-innocent ligands,^[88–90] or for determining the origins of magnetostructural correlations of different bridging motifs.^[91]

2.3. Practical Aspects for Calculations on 3d and 4f Complexes

In this work, the magnetochemistry of 3d and 4f ions is of special concern, and therefore, the most important aspects for quantum chemical calculations are briefly outlined. The energy scheme in 2.4 illustrates the applicability of different theoretical methods for the energy spectrum with succeeding introduction of the quantum mechanical effects mentioned in Chapter 1 for the example of octahedral Co(II). HF and DFT as monodeterminantal methods can only handle the ground state. HF theory, in general, is not applied anymore due to the superior properties of density functionals available in all standard program packages. Extensive benchmarks showed a remarkable precision of the structural predictions for transition metal complexes already met

2.3. Practical Aspects for Calculations on 3d and 4f Complexes

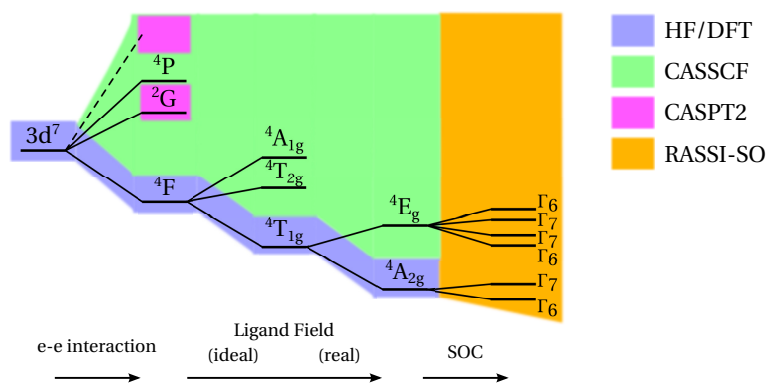


Figure 2.4.: Employed methods for computational treatment of different influences on the electronic structure for the example of Co(II) in an axially elongated O_h environment. Γ_6 and Γ_7 denote $M_S = \pm \frac{1}{2}$ respectively $M_S = \pm \frac{3}{2}$ doublets.

by GGA-DFT methods.^[92,93] Otherwise, DFT is likely to fail if a statement about the ground state multiplicity is desired.

Excited states of all multiplicities can be accounted for with state-averaged CASSCF (SA-CASSCF) calculations, where also results about state degeneracies are rather accurate. Pierloot *et al.* were able to show, how the use of a second set of d-functions for the description of the active space orbitals largely improved the performance of CASSCF calculations for late 3d ions due to "angular correlation" effects.^[94] Therefore, 10 d-orbitals localized at the transition metal were included in all CASSCF calculations of this work, which is also a *de facto* standard in actual research.^[95–97] Unlike found in Pierloot's early work, where atomic spectra were the subject of research, the s- and p- orbitals were not included in the active space, since the $s \rightarrow d$ transitions are much less important in complexes of the ions. For energetically close states of different multiplicities, CASSCF results have to be taken with care, since the correct order of the states may demand the CASPT2 method for the correct treatment of dynamical correlation (e.g. in Co(III) complexes^[98]). For lanthanide(III) ions, a multiconfigurational ansatz is mandatory because of the large number of low-lying states to be accounted for. Dynamical correlation was reported not to change the picture qualitatively for lanthanide ions (i.e. order of states in CASSCF and CASPT2 calculations),^[99] but it is also worth noting, that the sheer number of basis functions and states of real complexes demand very large computational resources.

Scalar relativistic effects may be included in the Hamiltonian by two major approaches used in literature, either the zeroth-order regular approximation

2. Theoretical Methods

(ZORA)^[100-102] or the Douglas-Kroll-Hess Hamiltonian (DKH).^[103] They become non-negligible for heavy atoms ($Z > 40$), but may also substantially enhance the results for lighter elements, like calculations of atomic spectra of Cu.^[104] Due to the availability in the program package MOLCAS,^[105] the DKH approach was used for all calculations. The remaining relativistic effect due to spin-orbit coupling, which is necessary to understand the non-intuitive magnetic properties of ions exhibiting this effect, is treated by the restricted active space state interaction method with spin-orbit coupling (RASSI-SO).^[104]

As stated-above examination of cooperative effects between 3d metals, are regularly treated by means of BS-DFT. It was found in several studies, that almost quantitative agreement with experiment is achieved, especially if the B3LYP functional was employed, whereas GGA functionals often heavily deviate.^[85,106] Magnetic interactions between 4f ions on the other hand are of much lower magnitude and contain a significant part of dipole-dipole interactions. Because calculations on the magnetic properties of lanthanide(III) ions are outside the abilities of BS-DFT, their interactions with other ions in oligonuclear complexes was only investigated by simulations. The POLY_ANISO routine developed by Chibotaru *et al.*^[98,99,107] is able to calculate dipole-dipole interactions between these ions from their spin-orbit functions obtained by the RASSI-SO method. Exchange interactions of arbitrary size can be included and the $\chi_M T$ curves can be compared with measured data.

Part II

Results

DINUCLER METALLAMACROCYLES WITH CARBAZOLE-BASED LIGANDS

When derivatives of 3,6-diaminocarbazole are condensed with salicylic aldehydes, Schiff-base ligand with two bidentate binding pockets are formed. The distance between the two coordination sites and the rigidity of the carbazole backbone induce the formation of dinuclear metallamacrocycles, when the carbazole-based ligands react with transition metals.^[108] To introduce new functionalities (e.g. optical), also anchoring groups were attached to the carbazole nitrogen.^[50]

To obtain new properties of the carbazole system, some results of Fischer & Neugebauer were introduced into the ligand design. Besides preparing different substitution patterns of different *tert*-butyl carbazoles,^[109] Fischer & Neugebauer showed that the lithium salt of 1,3,6,8-tetra-*tert*-butyl carbazole can be oxidized with elemental iodine in benzene.^[110] The neutral radical was shown to be stable in the solid state by recrystallization from a benzene solution. EPR measurements of the radical revealed large spin densities located at the nitrogen atom as well as at the carbon atoms at position 1 and 3. Large spin densities should result in a higher reactivity of this positions compared to the other ring positions. But since positions 1, 3, 6, and 8 are protected by bulky *tert*-butyl groups, the aminyl radical remains stable.

To obtain transition metal complexes based on carbazole that are possibly able to be oxidized to aminyl radicals, *tert*-butyl groups are introduced at the positions next to the hetero atom of the ring system.

3. Dinuclear Metallamacrocyles with Carbazole-Based Ligands

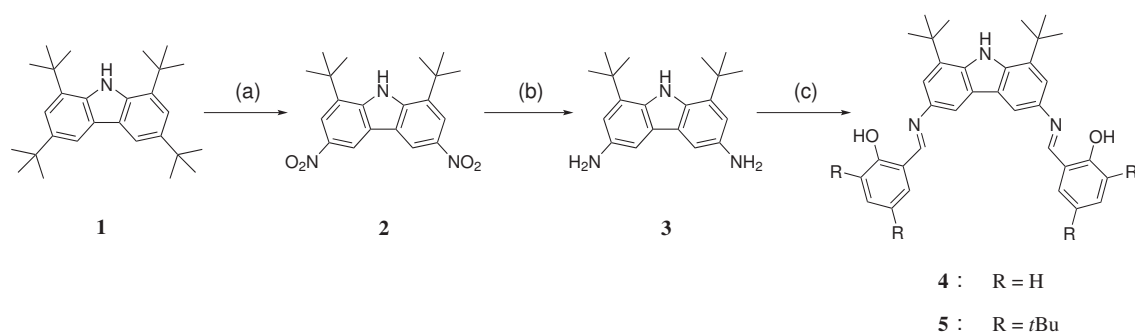


Figure 3.1.: Overview of the preparation of the ligands **4** and **5**.

(a) Cu(NO₃)₂, AcOH, Ac₂O; (b) 60 bar H₂, Pd/C, EtOH, 60°C; (c) derivative of salicylic aldehyde, MeOH, reflux, 1h.

3.1. Synthesis

3.1.1. Synthesis of the Ligand

The synthesis of the ligand in 4 steps is lined out in Fig. 3.1. In the first step, 9H-carbazole is tetra-alkylated. The procedure proposed by Neugebauer & Fischer delivers a mixture of all possible substitution patterns with *tert*-butyl groups in position 1, 3, 6, and/or 8.^[109] A procedure reported by Moskalev proved to be more effective: the carbazole is alkylated employing *tert*-butyl alcohol in trifluoro acetic acid with an almost quantitative yield of **1** and no side products.^[111] **1** is then nitrated with copper(II) nitrate in a mixture of glacial acetic acid and acetic acid anhydride. Under this conditions, the intermediate nitration agent acetyl nitrate is formed, which is known to react very selectively, but is also potentially explosive. The main product is the desired 1,8-di-*tert*-butyl-3,6-dinitro carbazole **2**, which is easily purified by recrystallization. **2** is then reduced in a hydrogen atmosphere at 60 bar employing palladium on charcoal as the catalyst. 3,6-Diamino-1,8-di-*tert*-butyl carbazole **3** is obtained in quantitative yield by filtering off the catalyst and removing the solvent *in vacuo*.

The Schiff-Base ligands are generated by a condensation reaction of **3** and either salicylic aldehyde or 3,5-di-*tert*-butyl salicylic aldehyde, leading to H₂L^H (**4**) or H₂L^{*t*Bu} (**5**), respectively. When methanol is used as solvent, the product can be filtered off after refluxing the reaction mixture for one hour due to the low solubility of the ligands in polar solvents. The ligands were characterized by ¹H- and ¹³C-NMR spectroscopy, mass spectrometry, elemental analysis, and IR spectroscopy.

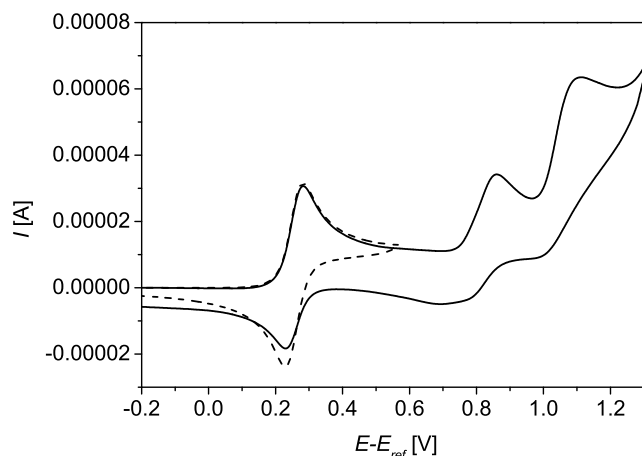


Figure 3.2.: Cyclic voltammetric oxidation of 1.33 mM of complex **8** using a scan rate of 1 V/s.

3.1.2. Synthesis of the Complexes

When the ligands **4** and **5** are reacted with copper(II) acetate, cobalt(II) acetate, or zinc(II) acetate, dinuclear metallamacrocycles of the formula $[M_2(L)_2]$ are formed. Due to the different solubilities of the ligands and the metal acetates, a mixture of methanol and chloroform was used. When a solution of a metal(II) acetate is added to a solution of a ligand, the complex is obtained as a microcrystalline precipitate. Slow diffusion of a methanolic layer of the metal salt into a layer of the ligand in chloroform yielded crystals suitable for single crystal diffraction. X-ray crystallography revealed the formation of dinuclear complexes $[Cu_2(L^H)_2]$ (**6**), $[Cu_2(L^{tBu})_2]$ (**7**), $[Co_2(L^H)_2]$ (**8**), $[Co_2(L^{tBu})_2]$ (**9**), and $[Zn_2(L^H)_2]$ (**10**). All complexes were characterized by IR spectroscopy, mass spectrometry and elemental analysis.

Unfortunately, all experiments involving the oxidation of the complexes employing PbO_2 , I_2 , or electrochemical methods did not yield any aminyl radicals as found for **1**.^[109] For the chemical oxidation agents, no reaction at all was observed, while cyclic voltammetric measurements shown in Fig. 3.2 revealed two irreversible oxidation steps above 0.8 V. A similar behavior at this potential was already observed for salicylidene anils,^[112] and, hence, the imine group is probably oxidized before the desired oxidation of the carbazole nitrogen can take place. In addition, a reversible oxidation process is found, if the CV was recorded over a smaller potential range, that was assigned to the oxidation of the Co(II) ions to Co(III).

3.2. Crystal Structures

X-Ray diffraction measurements on single crystals reveal a closely related structure of the transition metal complexes of ligands **4** and **5**. All obtained complexes exhibit a macrocyclic constitution formed by two doubly deprotonated ligand molecules and two metal ions, as depicted in Fig. 3.3. Each coordination pocket of the ligands donates one phenolate oxygen atom and one imino nitrogen atom to form a $[N_2O_2]$ donor set for each metal ion. Structural parameters of the coordination environments of the complexes **6-10** are listed Table 3.1. Despite the similarities of the molecular structures, the complexes crystallize in different space groups. Only crystals of **6** and **9** exhibit the same space group $P2_1/c$. But, however, the symmetry operations for creating symmetrically equivalent atoms of one complex molecule (see note below Table 3.1) reveals a different alignment of the complex molecules within the unit cell. These symmetry operations furthermore illustrate the inversion symmetry of all complexes. Metal-oxygen bond distances are all in the range of 190 ± 2 pm, while metal-nitrogen bond lengths show a larger variance. The shortest M–N bond lengths were found for the Cu(II) complexes with ≈ 195 pm. **8** exhibited a M–N bond length difference of 4 pm with distances of 195.5 pm and 199.7 pm, whereas for **9** these bond lengths were rather similar (198.8 pm and 198.4 pm). For the Zn(II) complex **10**, the largest M–N bond lengths of more than 200 pm are observed. The bite angles $\angle O1-M-N1$ and $\angle O2A-M-N2A$ are somewhat smaller for **6** and **7** ($\approx 94^\circ$), than for the other complexes. Furthermore, for the Cu(II) complexes, the largest distances between the metal and the salicylidene planes ($d(M-Sal1)$, $d(M-Sal2)$) are encountered. More differences become obvious by comparing the dihedral angle $\angle Sal1/Sal2$ between the salicylidene moieties, yielding $\leq 50^\circ$ for Cu(II), while values of $\approx 76^\circ$ are found for the Co(II) and Zn(II) complexes. Also, the Cu(II) ion in **6** and **7** does have a larger distance to the salicylidene planes than in the Co(II) and Zn(II) complexes. A similar trend is found for the dihedral angle between the carbazole moiety and the the salicylidene moieties ($\angle Sal1/Carb$, $\angle Sal2/Carb$), being a bit smaller for the Cu(II) compounds. Although the molecular structures of all complexes are quite similar, the d^9 configuration of Cu(II) favors a square planar coordination environment (Jahn-Teller effect), while Co(II) and Zn(II) are satisfied with a tetrahedral arrangement.

The shape of the coordination polyhedra was further characterized utilizing continuous shape measures (CShM) as proposed by Avnir *et al.*,^[113] with S_i values describing the differences compared to an ideal geometry with a real value between 0 and 100. The

Table 3.1.: Selected bond lengths [pm], bond angles [°], dihedral angles [°] between mean planes of the salicylidene moieties (Sal1 and Sal2)^a and the carbazole body (Carb),^b the tilting [°] between the two benzene moieties (Ar1 and Ar2),^c the deviation $d(\text{M-Sali})$ [pm] of the metal ion and the salicylidene planes, and the CShM parameters for the complexes **6**, **7**, **8**, **9**, and **10**.

M	6 Cu	7 Cu	8 Co	9 Co	10 Zn
M–O1	188.9(2)	189.1(3)	191.2(2)	189.8(2)	191.8(2)
M–O2A	190.6(2)	189.6(3)	189.8(2)	189.5(2)	190.3(2)
M–N1	194.8(2)	194.2(3)	199.4(2)	198.4(2)	202.3(2)
M–N2A	194.7(2)	195.3(3)	198.8(2)	198.8(2)	200.7(2)
O1–M–O2A	93.59(7)	99.63(12)	118.81(9)	121.87(7)	122.22(8)
O1–M–N1	94.18(8)	93.73(13)	96.24(8)	95.26(7)	96.26(8)
O1–M–N2A	149.62(8)	140.58(13)	124.27(9)	121.87(7)	122.59(8)
O2A–M–N1	143.64(8)	143.90(14)	120.20(8)	120.85(8)	119.17(8)
O2A–M–N2A	94.02(8)	94.08(13)	96.74(8)	95.41(7)	97.92(8)
N1–M–N2A	96.92(8)	96.53(13)	101.04(8)	101.69(8)	97.42(8)
\angle Sal1/Sal2	47	50	77	75	76
\angle Sal1/Carb	46	30	49	42	55
\angle Sal2/Carb	27	36	46	62	39
\angle Ar1/Ar2	5	5	3	7	4
$d(\text{M-Sal1})$	47	59	1	25	0
$d(\text{M-Sal2})$	62	57	20	48	16
$S_{D_{4h}}$	8.229	10.498	23.404	24.142	24.043
S_{T_d}	10.263	8.018	1.931	1.993	1.882
S_{SS4}	5.676	5.266	6.272	6.988	6.612
$\Phi_{D_{4h} \rightarrow T_d}$ [%]	47	54	82	84	83

Atoms with the suffix A were generated by the following symmetry operations:

6: $-x, -y, 1-z$

7: $2-x, -y, 1-z$

8 and 9: $1-x, 1-y, 1-z$

10: $2-x, -y, 2-z$

^aSalicylidene mean planes are defined by the following atoms. Sal1: O1, N1, C1, C2, C3, C4, C5, C6, and C7. Sal2: O2, N2, C20, C21, C22, C23, C24, C25, and C26.

^bCarbazole mean plane is defined by the following atoms: N3, C8, C9, C10, C11, C12, C13, C14, C15, C16, C17, C18, and C19.

^cMean planes of the benzene rings of carbazole body is defined by the following atoms. Ar1: C8, C9, C10, C11, C12, and C13. Ar2: C14, C15, C16, C17, C18, and C19.

3. Dinuclear Metallamacrocycles with Carbazole-Based Ligands

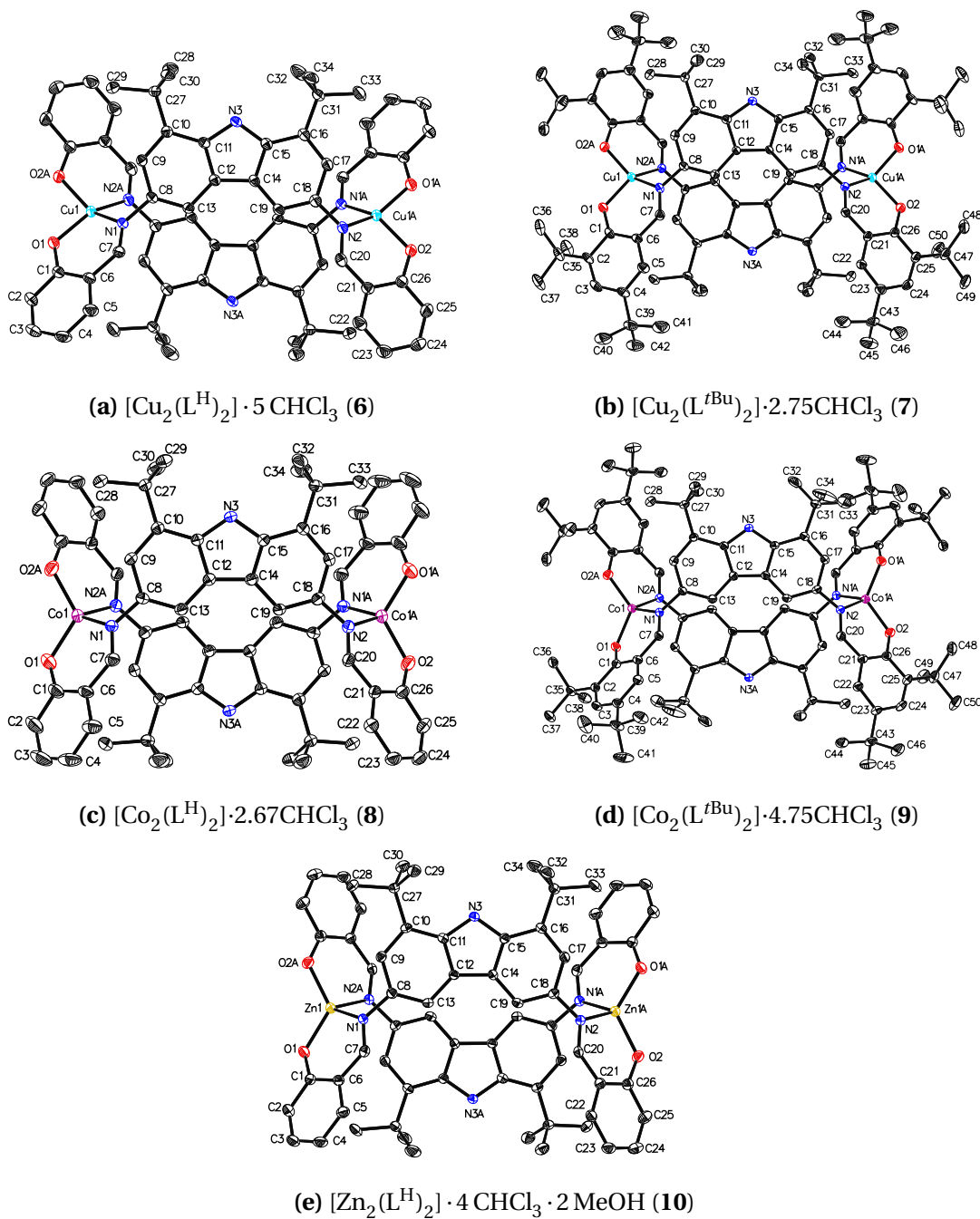


Figure 3.3.: Molecular structure of all five carbazole-based complexes. Non-carbon atoms are turquoise (Cu), pink (Co), yellow (Zn), red (O), and blue (N). Thermal ellipsoids are drawn at 50% probability. Hydrogen atoms were omitted for the sake of clarity.

Table 3.2.: Solvent accessible voids for the crystal structures where the co-crystallized solvent molecules could not be resolved.

Complex	Refined solvent molecules per dimer	Volume of void	e^-	Modeled solvent
6	5 CHCl ₃	–	–	–
7	2 CHCl ₃	375.1	42.7	0.75 CHCl ₃
8	–	408.9	155.0	2.67 CHCl ₃
9	2 CHCl ₃	546.5	160.5	2.75 CHCl ₃
10	4 CHCl ₃ + 2 MeOH	–	–	–

results are listed at the end of Table 3.1. While the transition metal in **8**, **9**, and **10** exhibits primarily tetrahedral coordination (low S_{T_d} values), the CShM results for Cu(II) in **6** and **7** are more or less ambiguous. S_i values may suggest a Seesaw (SS4) constitution (*cis*-divacant octahedron) at first, but employing minimal distortion pathways along with the deviation from these paths reveals for all five complexes to lie closest to the distortion pathway from tetrahedral to square planar geometry. The angular fractions $\phi(D_{4h} \rightarrow T_d)$ show, that the coordination polyhedra of **6** and **7** lie almost exactly halfway on the transition between ideal T_d and D_{4h} symmetry. As already found above utilizing S_i values, the Co(II) and Zn(II) are closer to tetrahedral coordination.

While the crystal structures of all complexes contained co-crystallized solvent molecules, only for **6** and **10** it was possible to completely refine their position to a satisfactory extent. During the refinement of the solvent molecules in the crystal structures **7** and **9**, one CHCl₃ molecule was possible to refine, whereas a part of the electron density data had to be modeled as solvent accessible voids utilizing the SQUEEZE/BYPASS procedure^[114] (see Section 10.2 for details). For Complex **8**, no stable refinement besides the electron density of the complex molecule itself was possible, and therefore, all of the co-crystallized solvent had to be modeled this way. The amount of electrons accounted for and the number of solvent molecules modeled therefrom are listed in Table 3.2.

3. Dinuclear Metallamacrocycles with Carbazole-Based Ligands

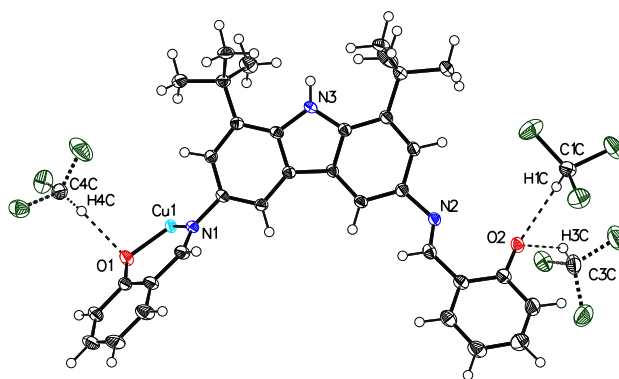


Figure 3.4.: Hydrogen bonds formed by co-crystallized solvent molecules in the crystal structures of **6**. Only the asymmetric unit is depicted. The chloroform molecules drawn with broken bonds are disordered around the same position each with a fractional occupation of 0.5.

Table 3.3.: Bond lengths [pm] and angles [°] found for the hydrogen bonds in $[\text{Cu}_2(\text{L}^{\text{H}})_2] \cdot 5 \text{CHCl}_3$ (**6**).

D–H···A	d(D–H)	d(H···A)	d(D···A)	$\angle(\text{D–H}\cdots\text{A})$
C1C–H···O2	100	223	309.3(2)	144.0
C3C–H···O2	100	220	316.7(2)	163.1
C4C–H···O1	100	220	319.5(2)	170.5

Unlike the carbazole-based complexes synthesized by Spielberg,^[50] π - π -stacking does not play an important role for the packing of the complex molecules in the crystal. Due to the bulky *tert*-butyl groups, preventing the aromatic moieties from ordering in a coplanar arrangement, large voids are found between the molecules, thus, enabling the cocrystallization of solvent molecules. For **6** and **10**, the solvent molecules form hydrogen bonds with the phenolate-oxygen atoms. The packing diagrams can be found in Appendix A.

In the crystal structure of **6**, CHCl_3 molecules are found at 3 positions, of which one is fully occupied ($\text{CHCl}_3(1)$), one is half occupied ($\text{CHCl}_3(2)$), and the third one exhibits a 1:1 disorder of an entire CHCl_3 molecule ($\text{CHCl}_3(3)$ and $\text{CHCl}_3(4)$). According to the bonding parameters listed in Table 3.3, $\text{CHCl}_3(1)$ and $\text{CHCl}_3(3)$ form hydrogen bonds to O2, while $\text{CHCl}_3(4)$ is oriented towards the oxygen atom O1. Due to the rather

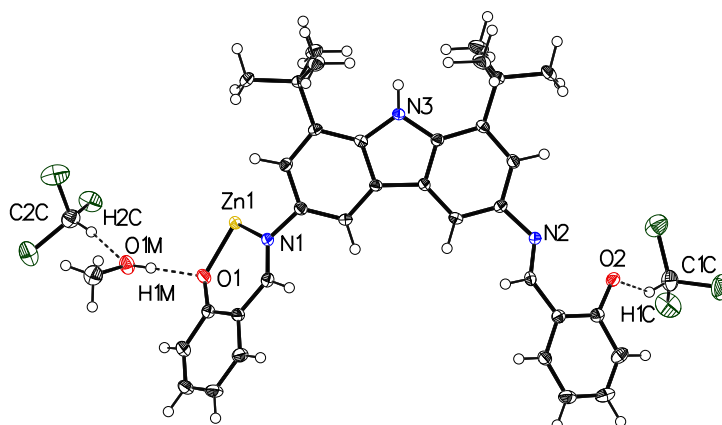


Figure 3.5.: Hydrogen bonds formed by co-crystallized solvent molecules in the crystal structure of **10**. Only the asymmetric unit is depicted.

confusing depiction of one complex molecule of **6** with hydrogen-bonded chloroform molecules at 6 positions, only the asymmetric unit is shown in Fig. 3.4.

The structure of **10** reveals, that the methanol molecule as well as one chloroform molecule each form hydrogen bonds to one of the phenolate-oxygen atom in the asymmetric unit. The second CHCl_3 molecule is bound to the methanol molecule (see Fig. 3.5 and Table 3.4). The sterically demanding *tert*-butyl groups at the salicylidene moieties of the ligand L^{tBu} in **7** and **9** do not allow hydrogen bonds with solvent molecules in a similar manner, and thus, are found only to underlie van-der-Waals interactions with the aliphatic groups.

Table 3.4.: Bond lengths [pm] and angles [°] found for the hydrogen bonds in $[\text{Zn}_2(\text{L}^{\text{H}})_2] \cdot 4\text{CHCl}_3 \cdot 2\text{MeOH}$ (**10**).

D-H...A	d(D-H)	d(H...A)	d(D...A)	$\angle(\text{D-H}\cdots\text{A})$
O1M-H1M...O1	84	192	276.2(3)	175.2
C2C-H2C...O1M	100	209	304.7(3)	159.7
C1C-H1C...O2	100	227	307.9(3)	136.8

3.3. Magnetic Properties

All magnetic measurements on the Cu(II) and Co(II) complexes were carried out on powdered samples of crystalline complexes. According to elemental analysis, the

3. Dinuclear Metallamacrocyles with Carbazole-Based Ligands

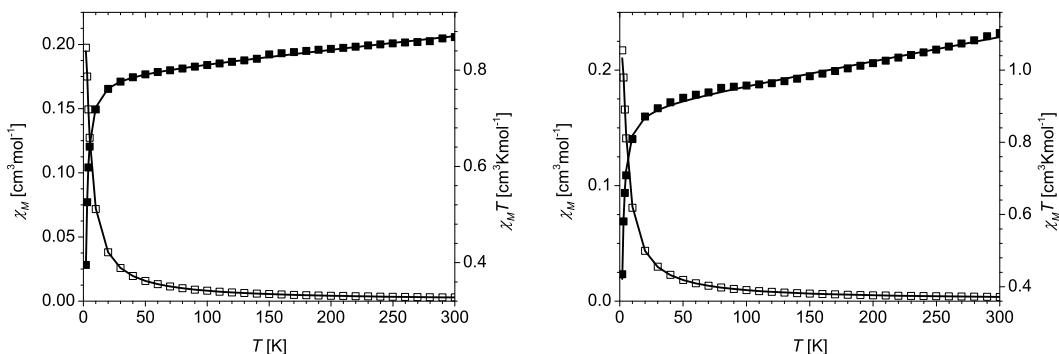


Figure 3.6.: Thermal dependence of χ_M (empty boxes) and $\chi_M T$ (black boxes) for **6** (left) and **7** (right). The solid lines are the simulated values using parameters mentioned in the text.

powders of **6**, **7**, and **9** did not contain any residual solvents. The sample of **8** used for magnetic measurements contained a different amount of co-crystallized solvent compared than proposed for the crystal structure, leading to the overall formula $[\text{Co}_2(\text{L}^{\text{H}})_2] \cdot 4 \text{CHCl}_3 \cdot 1 \text{MeOH}$. But this difference could also be attributed to the modeling by solvent accessible voids for the crystal structure of **8**, due to the lack of any statement about the atoms in the cavities.

Temperature-dependent susceptibility measurements were performed for **6**, **7**, **8**, and **9** with a static applied field of 5000 Oe in the temperature range from 2 to 300 K. In addition, for **8** and **9**, variable-field magnetization measurements from 0 to 50000 Oe in the temperature range between 2 to 5 K were performed. Furthermore, the Co(II) complexes were investigated utilizing ac SQUID susceptibility measurements. The powder of **8** was mixed with molten paraffin, since otherwise, it aligned in the magnetic field.

3.3.1. Copper(II) Complexes

Plots of the experimental χ_M and $\chi_M T$ values for **6** and **7** are shown in Fig. 3.6. Upon cooling from room temperature, $\chi_M T$ descends linearly. Below 50 K, the $\chi_M T$ value drops to less than half of the r.t. value.

$$\hat{H} = g\mu_{\text{B}}\mathbf{H} \cdot \sum_{i=1}^2 \hat{S}_i - J\hat{S}_1\hat{S}_2 \quad (3.1)$$

For complex **6** $\chi_M T = 0.87 \text{ cm}^3 \text{ K mol}^{-1}$ was measured at room temperature, linearly decreasing to $0.77 \text{ cm}^3 \text{ K mol}^{-1}$ at 30 K. The linear behavior may be attributed to diamag-

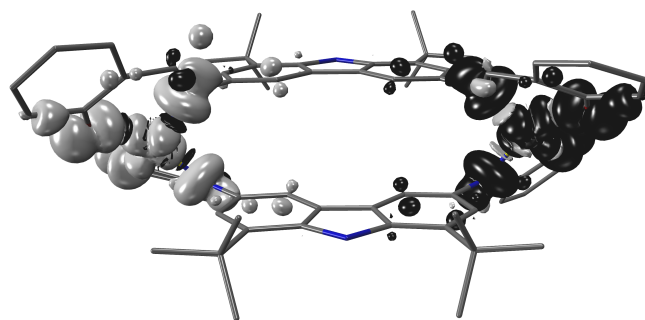


Figure 3.7.: Spin density plot for the broken-symmetry state of **6**. The iso-surface was drawn at $0.001 e^-/\text{\AA}^3$. The gray surface represents α -spin density, while the black surface represents β -spin density, respectively.

netism yet unaccounted for. A further reduction of the temperature causes $\chi_M T$ to decrease to $0.40 \text{ cm}^3 \text{Kmol}^{-1}$ at 2 K. To simulate the dinuclear system with two $S = \frac{1}{2}$ ions, the Hamiltonian shown in Eq. (3.1) was used. It takes into account the Zeeman interaction and the isotropic exchange interaction. For the description of the diamagnetism, the temperature-independent susceptibility term χ_{TIP} was introduced. A least-squares fit yields the parameters $g_{\text{eff}} = 2.05$, $J = -2.3 \text{ cm}^{-1}$, and $\chi_{\text{TIP}} = 2.76 \cdot 10^{-4} \text{ cm}^3 \text{mol}^{-1}$.

The susceptibility measurements of **7** show similar magnetic properties. In the high-temperature regime, $\chi_M T$ is found to be $1.10 \text{ cm}^3 \text{Kmol}^{-1}$. This value decreases almost linearly to $0.92 \text{ cm}^3 \text{Kmol}^{-1}$ at 50 K. $\chi_M T$ further declines to a value of $0.43 \text{ cm}^3 \text{Kmol}^{-1}$ at 2 K. By a least-squares fit, the parameters $g_{\text{eff}} = 2.19$, $J = -2.4 \text{ cm}^{-1}$, and a temperature-independent paramagnetism of $\chi_{\text{TIP}} = 6.6 \cdot 10^{-4} \text{ cm}^3 \text{mol}^{-1}$ were obtained.

The g -values found were slightly larger than 2.0, which is in the typical region for Cu(II) ions. Both complexes exhibit a small antiferromagnetic exchange interaction, which is in agreement with similar reported complexes.^[50,108] Due to the planar arrangement of the carbazole moieties and the coordinating imino nitrogen atoms, a spin-polarization model gives a reasonable explanation in spite of the large intramolecular Cu \cdots Cu distances of over 1000 pm. Additional BS-DFT calculations (B3LYP, def2-TZVP) for **6** suggest an exchange interaction parameter J of -1.5 cm^{-1} , which perfectly well reproduces the antiferromagnetic interaction experimentally found within the computational accuracy. The spin density plot in Fig. 3.7 illustrates the small delocalization of spin-density along the carbazole moiety. Calculations for **7**

3. Dinuclear Metallamacrocyles with Carbazole-Based Ligands

gave similar results with a calculated coupling constant of $J = -2.3 \text{ cm}^{-1}$

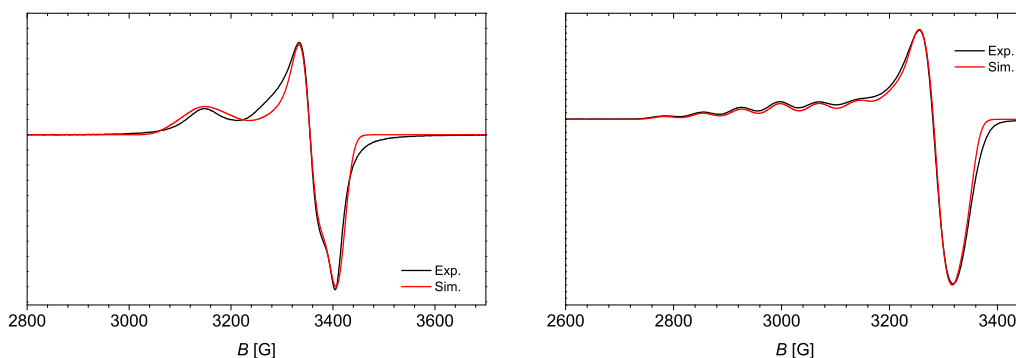


Figure 3.8.: X-band EPR spectra for **6** (left) and **7** (right). The simulations were done with the parameters given in the text.

Table 3.5.: g -values and hyper fine constants [G] obtained from simulations of the EPR spectra of **6** and **7**.

	g_x	g_y	g_z	A_x	A_y	A_z
6	2.058	2.092	2.232	9	10	45
7		2.055	2.257	23	142	

EPR spectra of the Cu(II) complexes recorded with an X-band EPR spectrometer are shown in Fig. 3.8. Complex **6** exhibits a rhombic signal, whereas **7** is found to give an axial spectrum. While the spectrum of **6** lacks any hyper fine structures, the parallel signal of **7** is split into 7 lines, of which one lies under the perpendicular signal. The hyper fine structure suggests an interactions between the electron spin and the two copper nuclei, which exhibit a nuclear spin of $I = \frac{3}{2}$. The EPR spectra were simulated accounting for the Zeeman interaction and the hyper fine splitting A using Hamiltonian shown in Eq. (3.2) for one Cu(II) ion with the natural isotope abundance (69.17% ^{63}Cu , 30.83% ^{65}Cu , both $I = \frac{3}{2}$). Due to the large magnitude of J found by SQUID measurements, transitions between exchange coupled states cannot be observed with a microwave energy of $\approx 0.33 \text{ cm}^{-1}$ as employed in X-band EPR.

$$\hat{H} = g\mu_B \mathbf{H}\hat{S} + A\hat{S} \cdot \hat{I} \quad (3.2)$$

The g -values obtained have a magnitude of < 2.1 for the transversal elements and close to 2.20 for the parallel elements (see Table 3.5), which is in the expected range for distorted tetrahedral Cu(II). The hyper fine interaction for **6** does not manifest in multiple

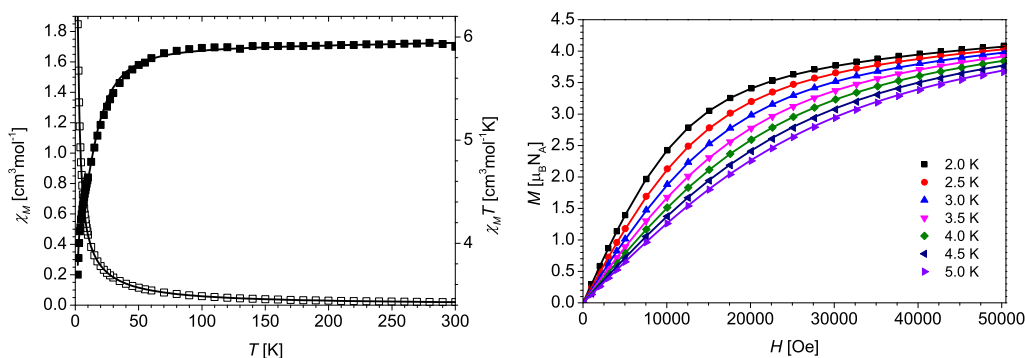


Figure 3.9.: Left: Thermal dependence of χ_M (empty boxes) and $\chi_M T$ (black boxes) for **8**. The solid lines are the simulated values using parameters mentioned in the text. Right: Variable-field magnetization data for **8** at different temperatures. Solid lines are simulated values with the parameters mentioned in the text.

signals, but rather broadens the signals, yielding relatively small A values. For **7**, the perpendicular hyper fine constant $A_{\perp} (= A_x = A_y)$ is also small, but the characteristic splitting pattern of the parallel signal with seven maxima leads to a significantly larger $A_{\parallel} (= A_z)$ of 142 G in the simulation.

3.3.2. Cobalt(II) Complexes

The temperature-dependent susceptibilities and variable-field magnetizations for both complexes **8** and **9** show similar behavior and are depicted in Fig. 3.9 (complex **8**) and 3.10 (complex **9**), respectively. EPR measurements only gave very broad signals in both parallel and perpendicular modes.

At 300 K, **8** is found to exhibit $\chi_M T = 5.93 \text{ cm}^3 \text{ K mol}^{-1}$. $\chi_M T$ stays almost constant when cooled to 100 K. Further cooling causes $\chi_M T$ to decrease to $5.73 \text{ cm}^3 \text{ K mol}^{-1}$ at 50 K, and from there, to drop more steeply, reaching $3.70 \text{ cm}^3 \text{ K mol}^{-1}$ at $T = 2 \text{ K}$. The magnetization measurements for all temperatures show a steady increase of M with increasing magnetic field applied. For the lowest temperature, M approximates a value of $4.09 \mu_B N_A$ at 50000 Oe, but has not reached saturation yet.

For complex **9**, $\chi_M T = 4.67 \text{ cm}^3 \text{ K mol}^{-1}$ was measured at room temperature. This value slightly decreases to $4.57 \text{ cm}^3 \text{ K mol}^{-1}$ at 100 K. On further cooling, $\chi_M T$ steadily drops to $2.87 \text{ cm}^3 \text{ K mol}^{-1}$ at 2 K. Magnetization measurements at 2.0 K show a value of $M = 3.73 \mu_B N_A$ at 50000 Oe, but also here, the magnetization is not yet saturated.

3. Dinuclear Metallamacrocycles with Carbazole-Based Ligands

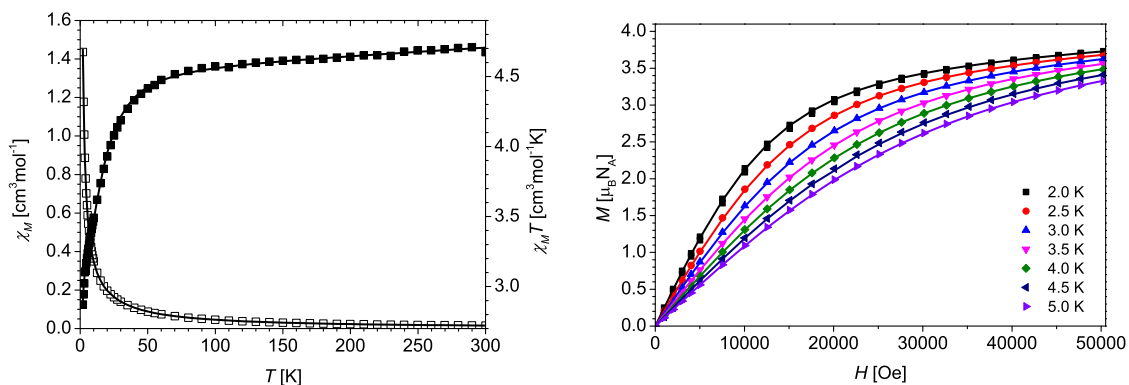


Figure 3.10.: Left: Thermal dependence of χ_M (empty boxes) and $\chi_M T$ (black boxes) for **9**. The solid lines are the simulated values using parameters mentioned in the text. Right: Variable-field magnetization data for **9** at different temperatures. Solid lines are simulated values with the parameters mentioned in the text.

$$\hat{H} = g\mu_B \mathbf{H} \cdot \sum_{i=1}^2 \hat{S}_i + D \sum_{i=1}^2 \left[\hat{S}_{z,i}^2 - \frac{1}{3} S_i (S_i + 1) \right] - J \hat{S}_1 \hat{S}_2. \quad (3.3)$$

The decrease of $\chi_M T$ for both complexes can be attributed either to an exchange interaction between different Co(II) centers or to the zero-field splitting of individual centers. The measured data for **8** and **9** were evaluated using full matrix diagonalization employing the Hamiltonian Eq. (3.3). In the most cases, an anisotropic g -value is necessary to correctly describe Co(II) ions, but to avoid overparametrization, only an isotropic g -tensor was assumed. A least-squares fit of the $\chi_M T$ for **8** data yields $g_{\text{eff}} = 2.50$, $|D| = 17 \text{ cm}^{-1}$, and an isotropic exchange interaction of $J = 0.15 \text{ cm}^{-1}$. For **9**, the parameters $g_{\text{eff}} = 2.20$, $|D| = 18 \text{ cm}^{-1}$ and $J = 0.10 \text{ cm}^{-1}$ are obtained. The sign of the axial ZFS parameter cannot be determined from the $\chi_M T$ data for an $S = \frac{3}{2}$ ion, since no characteristic differences between simulation with $\pm D$ are expected.^[115] Fits of the magnetization measurements yielded somewhat different parameter sets. For **8** the magnetic quantities found are $g_{\text{eff}} = 2.57$, $D = -37 \text{ cm}^{-1}$, and $J = -0.07 \text{ cm}^{-1}$, while the fits of M for **9** gave $g_{\text{eff}} = 2.38$, $D = -38 \text{ cm}^{-1}$ and $J = -0.08 \text{ cm}^{-1}$.

Dynamic Magnetic Measurements

The magnetic measurements of the dynamic behavior were performed with oscillating magnetic fields of 1 Oe magnitude and frequencies between 10 Hz and 1143 Hz. The *in-*

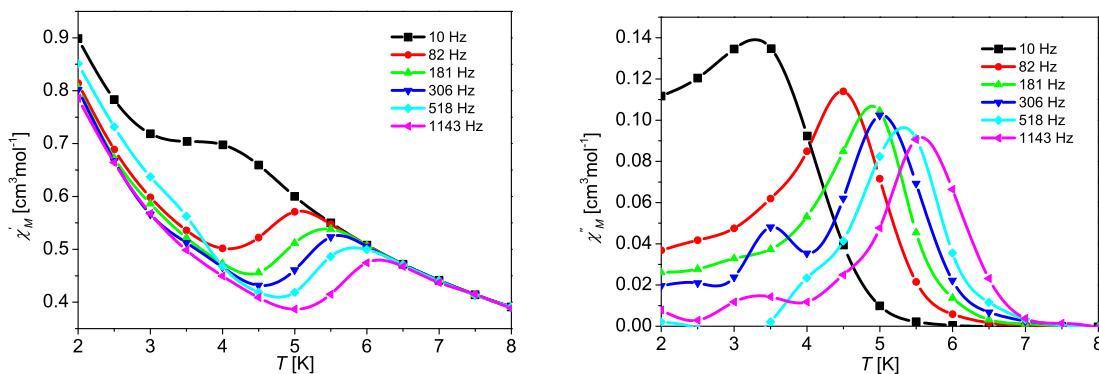


Figure 3.11.: Plots of the ac SQUID data for complex **8** with zero applied static field at different frequencies of the oscillating field. Measured data (symbols) and simulated values with the parameters mentioned in the text (solid lines). Left: Real part χ'_M . Right: Imaginary part χ''_M .

phase signal χ'_M and the out-of-phase signal χ''_M of the susceptibility were measured in the temperature range from 2 to 10 K in steps of 0.5 K.

The ac SQUID data measured for complex **8** with zero applied static field is shown in Fig. 3.11. For frequencies of 10 Hz and higher, χ''_M exhibit a clear maxima. At 10 Hz, the maximum is found at ca. 3.5 K, and is shifted to 5.5 K at a frequency of 1143 Hz. The temperature dependence of the maximum of χ''_M indicates a thermal relaxation process.

$$\chi(\omega) = \chi_s + \frac{\chi_0 - \chi_s}{1 + (i\omega\tau_c)^{1-\alpha}} \quad (3.4)$$

The dynamic behavior of the susceptibility was treated with Eq. (3.4). A least-square fit of the complex function delivers a set of parameters for each temperature, including the adiabatic susceptibility χ_s , the isothermal susceptibility χ_0 , the relaxation time τ_c , and the distribution width α . The quality of these parameters can be visualized with Cole-Cole-plots (plot of χ''_M vs. χ'_M), where the values for each temperature should lie on a (stretched or compressed) half-circle (see Fig. 3.12, left). Assuming a relaxation process of first order, a linear fit of the $\ln(\tau_c)$ vs. $\frac{1}{T}$ plot is feasible (Fig. 3.12, right). From the fit, a thermal relaxation barrier $U_{\text{eff}} = 53\text{K}$ was obtained. Application of a static dc field did not yield significantly different barrier heights. Unfortunately, several later experiments trying to reproduce the dynamic magnetic properties failed. Those samples contained considerably less solvent molecules according to their elemental

3. Dinuclear Metallamacrocycles with Carbazole-Based Ligands

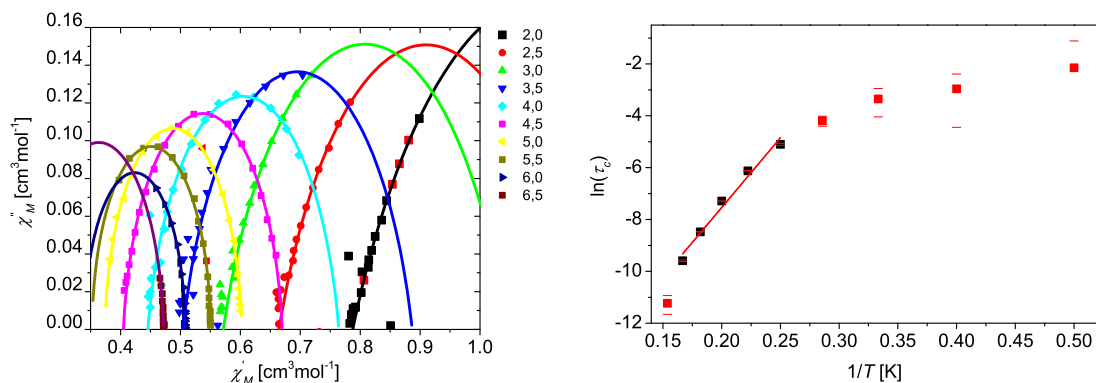


Figure 3.12.: Left: Cole-Cole-plot of imaginary susceptibility χ''_M vs. the real susceptibility χ'_M for **8**. The lines are simulated values with the parameters obtained by the fit of the complex function 3.4. Right: Arrhenius plot of τ_c values vs. $1/T$ for **8** with the error bars at each temperature. The red line is the linear regression function to obtain U_{eff} . The values depicted by red squares were omitted in the fit.

analysis. Thus, co-crystallized solvent molecules seem to be crucial in order to maintain the structure found to exhibit slow magnetic relaxation with zero applied field. Nevertheless, this also suggests, that the Co(II) ion, given the right coordination geometry, is able to show slow magnetic relaxation in a $[\text{N}_2\text{O}_2]$ environment. This donor set is rather common and easily accessible within the family of Schiff-bases of salicylic aldehydes. Furthermore, the very small exchange interaction indicates a mononuclear nature of this phenomenon.

For complex **9**, no out-of-phase susceptibility with zero applied field was observed. However, with an applied magnetic field of 400 Oe magnitude, complex **9** exhibited features of slow magnetic relaxation, e.g. maxima of the imaginary susceptibility, as shown in Fig. 3.13. For the lowest frequency of 10 Hz, the maximum is found at 3.0 K, and is shifted to 4.5 K for 1143 Hz. This again suggests a thermal relaxation process. The plots for all frequencies show increasing χ''_M values at lower temperatures, possibly indicating additional relaxation processes below 2.0 K. Fits of the complex function Eq. (3.4) gave all parameters to obtain Cole-Cole-plots (Fig. 3.14, left) as well as linear fits of the relaxation dynamics (Fig. 3.14, right), which yielded a relaxation barrier height $U_{\text{eff}} = 52$ K. A larger magnitude of the dc field of 1000 Oe does not induce a larger relaxation barrier height.

Since the two complexes exhibited rather similar coordination parameters in the crystal structures, also a closely related magnetic behavior had to be expected. The

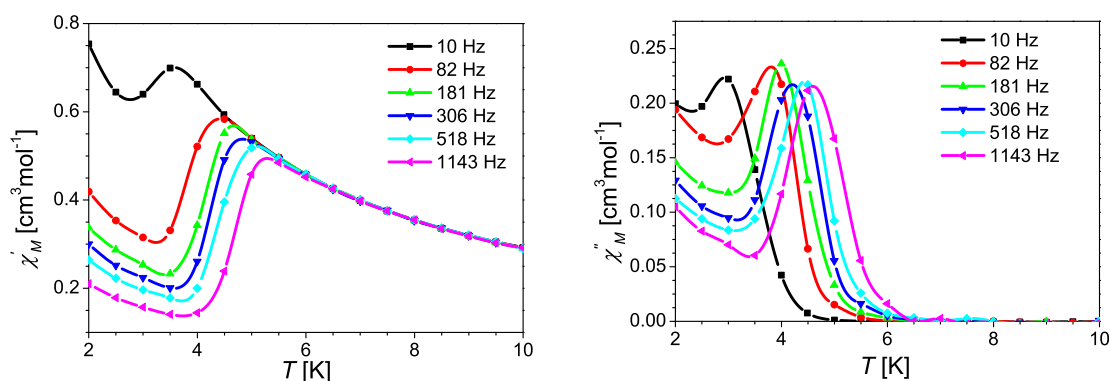


Figure 3.13.: Real and imaginary susceptibility of **9** with an applied magnetic field of 400 Oe

dc field measurements revealed, that the ZFS parameters of **8** and **9** was practically the same. The ac SQUID measurements did in fact yield SMM behavior for both complexes with comparable barrier heights U_{eff} of 53 and 52 K, but the absence of an out-of-phase susceptibility for **9** at zero external field seems rather random, since their coordination geometry is very similar. Due to the independence of U_{eff} from the magnitude of the external magnetic field, an Orbach process explains best the dynamic magnetic properties, since for a thermally-assisted quantum tunneling (TAQT) process, the lifting of the degeneracy of the excited KD would heavily affect the relaxation dynamics, or even prevent them completely. Absence of an χ_M'' -signal for **9** at zero external field may be caused by tunneling processes within the ground state KD, which is investigated further in Chapter 4 by theoretical methods. Furthermore, this illustrates the large influence of small changes in the coordination environment on the magnetization relaxation processes.

SMM behavior of Co(II) ions was previously mainly described for octahedral and square pyramidal coordination environments. The first reported zero-field SMM, however, had a tetrahedral surrounding of the Co(II) ion by four thiophenolate anions. Here, another promising coordination geometry was found to enable SMM behavior for Co(II) ions. Thus, more known and unknown complexes with tetrahedral $[\text{N}_2\text{O}_2]$ donor sets were prepared by our workgroup and investigated for their magnetic behavior. Theoretical investigations on some of the examples exhibiting SMM behavior were performed and are presented in the following chapter.

3. Dinuclear Metallamacrocyles with Carbazole-Based Ligands

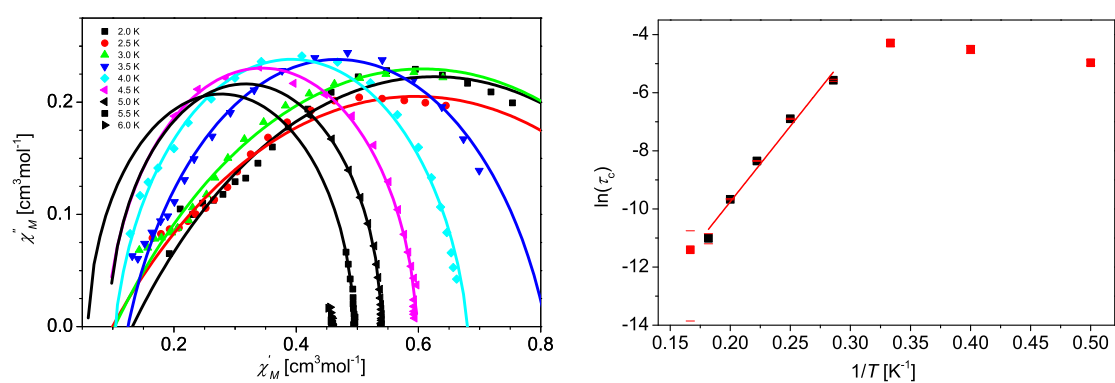


Figure 3.14.: Left: Cole-Cole-plot of imaginary susceptibility χ''_M vs. the real susceptibility χ'_M for **9**. The lines are simulated values with the parameters obtained by the fit of the complex function 3.4. Right: Arrhenius plot of τ_c values vs. $1/T$ for **9** with the error bars at each temperature. The red line is the linear regression function to obtain U_{eff} . The values depicted by red squares were omitted in the fit.

ELECTRONIC STRUCTURE OF TETRAHEDRAL COBALT(II)

SMMS

Co(II) complexes may be obtained with coordination numbers between two and eight,^[116] and, depending on the exact coordination environment, are able to exhibit a low-spin or high-spin ground state. Most commonly encountered are the coordination numbers four (tetrahedral, square-planar), five (trigonal-bipyramidal, square-pyramidal), and six (octahedral, rarely trigonal-prismatic).^[117,118] Octahedral Co(II) may exhibit high-spin or a low-spin ground state, depending on the nature of the ligand field. From the d^7 Tanabe-Sugano diagram shown in Fig. 4.1, it can be seen, that for weaker ligand fields an orbitally threefold degenerate $^4T_{1g}$ ground term is present, while stronger ligand fields induce a 2E_g ground term. For complexes with a ligand field close to this ground term transition, the spin-crossover phenomenon is regularly encountered, as reported for terpyridinone and terpyridinone complexes of Co(II).^[47,119,120] Fivefold coordinated Co(II) may exhibit square-pyramidal or trigonal-bipyramidal geometry, and, due to the intermediate ligand-field splitting, low- and high-spin complexes are possible.^[121] Fourfold coordination leads to two important geometries for Co(II): tetrahedral, which is mostly encountered and only enables a high-spin ground state, and square-planar, causing low-spin compounds in all reported cases.^[117,121] For the slow magnetic relaxation phenomenon, only the d^7 high-spin ground state is of interest.

The first reported Co(II) compound with SMM behavior was, similar to other transition metals, a polynuclear complex, namely $[\text{Co}_4(\text{hmp})_4(\text{MeOH})_4\text{Cl}_4]^*$, exhibiting

*hmp⁻ is the anion of hydroxymethylpyridine.

4. Electronic Structure of Tetrahedral Cobalt(II) SMMs

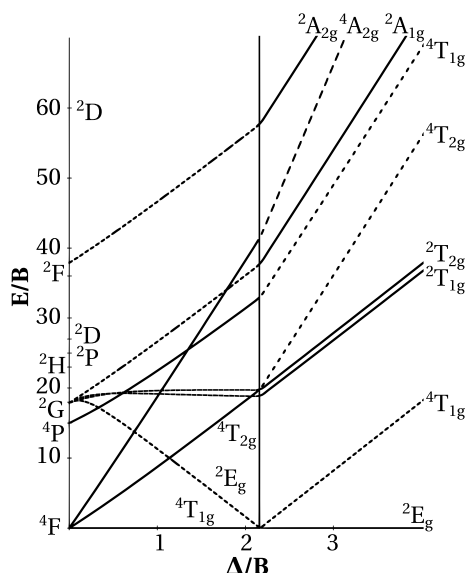


Figure 4.1.: Tanabe-Sugano diagram for the d^7 configuration in an octahedral coordination environment. The vertical line marks the ligand field strength, where the ground state changes. Dashed lines designate terms of different multiplicity than the ground term.

hysteresis of magnetization.^[122] In the following years, mostly oligonuclear complexes with primarily octahedral coordination environments were published.^[123] Though it was not recognized in the literature, the first mononuclear SMM involving trigonal-bipyramidal Co(II) (and at that time, also the first mononuclear transition metal SMM in general) was reported by Boča *et al.*^[124] A tetrahedral complex, that also demonstrated the interplay with theory,^[125] was reported by Zdrozny *et al.*,^[126] and showed a relaxation barrier of 70 K without an applied dc field. Large relaxation barriers were also achieved with heterospin systems involving diazo-substituted ligands, that were irradiated to afford stable carbenes at low temperatures.^[127,128]

In theory, high-performing SMMs are obtained, when a large ZFS interplays with a strong axiality of the g -tensor, effectively inhibiting tunneling processes. However, even if the molecular structure is known, predicting D and E is not a straight-forward task.^[115] In the last years, several investigations of ZFS in Co(II) addressed the rationalization of certain cases and its correlation with structural parameters.^[129–133] Two of these studies examine tetrahedral Co(II) complexes, but, unfortunately, only investigate Co(II) complexes with moderate ZFS of $|D| < 10 \text{ cm}^{-1}$. The Co(II) complexes described in Chapter 3 and those reported by Buchholz *et al.*,^[51] however, exhibit

tetrahedral [N₂O₂] donor environments, which are able to easily generate values of $D \approx -30 \text{ cm}^{-1}$. Thus, also taking a closer look at recently synthesized complexes with SMM behavior, *ab initio* calculations were performed, to obtain new insights on the electronic structure of Co(II) in tetrahedral [N₂O₂] environments and possibly new inspirations for the design of new high-performing SMMs. Unfortunately, the theoretical description of Co(II) is rather complicated, due to the strong intrinsic spin-orbit coupling. Here, the multiconfigurational CASSCF/CASPT2/RASSI methodology was employed.

4.1. [N₂O₂] Coordinated Cobalt(II) Complexes

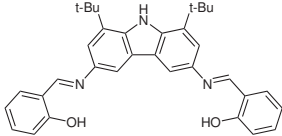
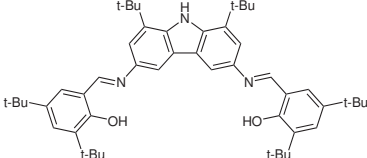
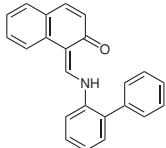
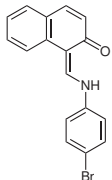
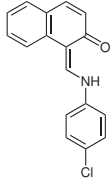
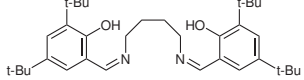
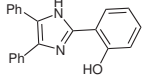
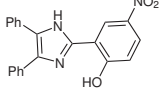
The tetrahedral Co(II) complexes under investigation are listed in Table 4.1. Complexes **8** and **9** were described earlier in Chapter 3. **11**, **12**, **13**, and **14** were prepared by Ziegenbalg during his diploma thesis^[52] and show slow magnetic relaxation under applied magnetic field. Furthermore, if oxygen is present, the oxidized Co(III) ion may be octahedrally coordinated by ligands with suitable substituents. Ziegenbalg also found, that symmetric condensates of 1,4-diaminobutane and salicylic aldehydes mainly form octahedral complexes of Co(III) preferably in dinuclear aggregates. Only in the case of **14**, a distorted tetrahedral coordination was observed. Moreover, the mononuclear Co(II) SMMs **15** and **16** containing imidazole-based ligands were included.^[51] To confirm the correct prediction of the ground state, four square-planar complexes listed in Table 4.2 were included in the set of calculated complexes. Complex **17** was also prepared by Ziegenbalg,^[52] whereas **18**, **19**, and **20** were reported elsewhere.^[134–136]

A search in the Cambridge Structure Database (CSD) using the substructure shown in Fig. 4.2 (left) features the distribution of the distance $r(\text{Co-X})$ with respect to the angle δ^\dagger depicted in the scatter plot in Fig. 4.2 (right). The vast majority of reported complexes exhibits values of either $\delta < 15^\circ$ (square-planar) or $\delta > 65^\circ$ (tetrahedral). Furthermore, Fig. 4.2 shows shorter Co–O and Co–N bond lengths for the square-planar complexes than found in tetrahedral ones, representing their different ground state multiplicities (low-spin for square-planar, high-spin for tetrahedral coordination). Four data sets, however, lie in the range between. For none of them, measurements for determining the ground state multiplicity are available. The two sets at 20.8 and 22.4° are values from two non-equivalent molecules of the same crystal structure^[137] with essentially distorted square-planar geometry, that most probably leads

[†] δ is defined as the angle between the planes containing the atoms (Co, N1, O1) and (Co, N2, O2).

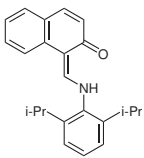
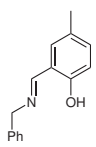
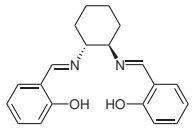
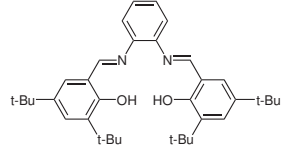
4. Electronic Structure of Tetrahedral Cobalt(II) SMMs

Table 4.1.: Tetrahedral Co(II) complexes investigated concerning their possible SMM behavior.

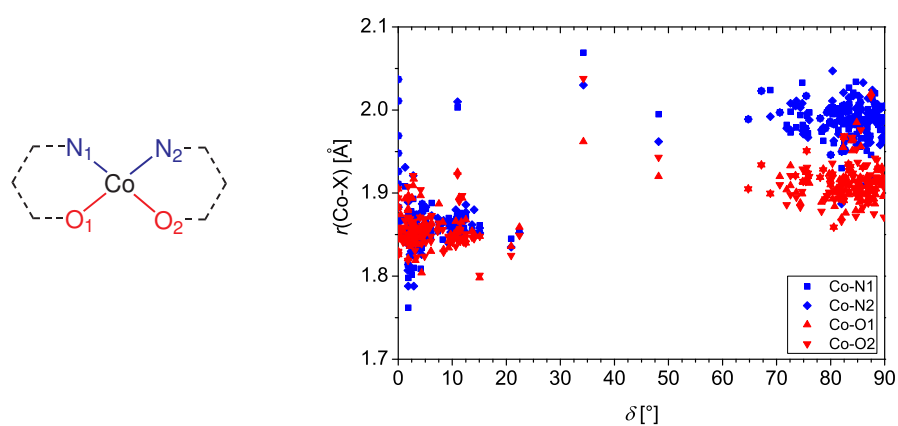
Complex	H_nL^a	Constitution	U_{eff} [K]	D [cm^{-1}]	δ [$^\circ$]
8		Co_2L_2	53 (0 Oe)	-37	78.7
9		Co_2L_2	52 (400 Oe)	-38	80.6
11		CoL_2	61 (400 Oe)	-40	64.8
12		CoL_2	51 (400 Oe)	-37	85.6
13		CoL_2	56 (400 Oe)	-24	85.0
14		CoL	tunneling	-46	71.4
15		CoL_2	89 (400 Oe)	-41	72.6
16		CoL_2	-	-35	74.9

^a n corresponds to the number of acidic protons shown in the structure.

Table 4.2.: Square-planar Co(II) complexes investigated concerning their possible SMM behavior.

Complex	H_nL^a	Constitution	δ [°]
17		CoL_2	3.7
18		CoL_2	0.0
19		CoL	10.9
20		CoL	9.8

^a n corresponds to the number of acidic protons shown in the structure.

**Figure 4.2.:** Structural motif employed for the CSD search and scatter plot of the bond lengths in reported complexes with respect to δ .

4. Electronic Structure of Tetrahedral Cobalt(II) SMMs

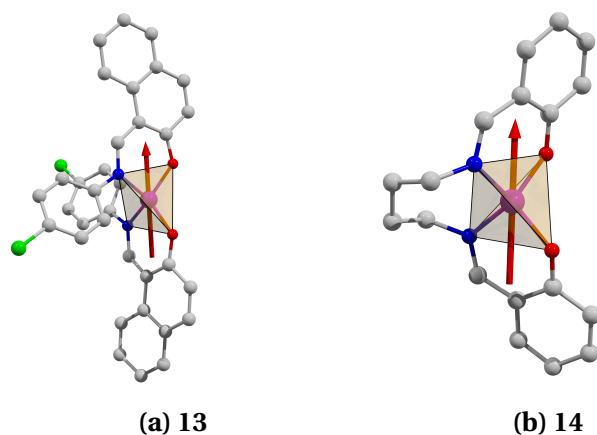


Figure 4.3.: Employed structures for two of the calculated Co(II) complexes with the designated orientation of the easy-axis of magnetization.

to a low-spin ground state, as suggested by the bond lengths below 1.9 Å. For the data sets found at $\delta = 34.3^\circ$ [138] and 48.2° , [139] the bond distances point towards a high-spin ground state. The corresponding values of δ for the investigated complexes, which are listed in Tables 4.1 and 4.2, confirm, that all of them belong to one of the aforementioned groups.

For all investigated complexes, a quartet ground state is suggested by the CASSCF calculations (energies listed in Tables D.1 and D.3). The quartet-doublet gap $E_{Q-D} = E_D - E_Q$ is found to be at least 14000 cm^{-1} for the tetrahedral complexes, (E_D and E_Q are the energies of the lowest doublet and quartet states, respectively). The square-planar complexes, however, exhibit a substantially smaller E_{Q-D} between 2300 and 3700 cm^{-1} . Introducing dynamic correlation *via* CASPT2 does not change the picture for the tetrahedral complexes, since the quartet-doublet gap is lowered by only 2000 - 3000 cm^{-1} . The lowest quartet state shows an energy separation between 1700 and 2500 cm^{-1} to the first excited quartet state and may be interpreted as the A_2 ground term. For the square-planar complexes, on the other side, the ground state multiplicity changes upon the introduction of dynamic correlation, reproducing the experimentally found ground state. Thus, it is shown, that the use of CASPT2 is essential to obtain the correct ground state for Co(II) complexes. In order to obtain slow magnetic relaxation behavior, an $S = \frac{1}{2}$ ion is not desired, and, hence, complexes **17-20** were not further investigated concerning spin-orbit interaction.

To further analyze the electronic structure behavior of the tetrahedral Co(II) com-

Table 4.3.: Angular fraction of minimal distortion pathway between D_{4h} and T_d symmetry, calculated ZFS parameter, energy barrier between the two lowest KDs, and main values of the g -tensors for **8**, **9**, and **11-16**.

	$\Phi_{SP4 \rightarrow T4}$ [%]	δ [°]	D [cm^{-1}]	$ E $ [cm^{-1}]	U_{eff} [K]	KD	g_1	g_2	g_3
8	82.0	78.7	-28	1	82	1	0.3068	0.3301	7.4576
						2	2.5056	3.9937	4.5751
9	83.6	80.6	-30	0	88	1	0.0885	0.0914	7.5101
						2	2.5347	4.1984	4.3587
11	65.6	64.8	-35	4	104	1	0.6501	0.7703	7.6893
						2	2.5691	3.6526	4.8057
12	86.7	85.6	-27	0	77	1	0.0248	0.0284	7.4644
						2	2.5255	4.2626	4.3110
13	86.0	85.0	-26	0	75	1	0.0108	0.0140	7.4441
						2	2.5181	4.2751	4.3035
14	73.2	71.4	-30	3	87	1	0.6106	0.7045	7.4554
						2	2.4710	3.6715	4.8051
15	73.7	72.6	-37	3	108	1	0.4105	0.4551	7.8085
						2	2.6588	3.9209	4.6093
16	76.5	74.9	-36	1	102	1	0.1613	0.1660	7.7728
						2	2.6567	4.1720	4.4025

4. Electronic Structure of Tetrahedral Cobalt(II) SMMs

plexes, the spin-orbit states were calculated utilizing the RASSI-SO procedure in combination with the SINGLE_ANISO routine for the calculation of the ZFS parameters. The calculated ZFS parameters D and E , the theoretical spin reversal barrier U_{eff} as well as the g -values of the two lowest KDs of **8**, **9**, and **11-16** are listed in Table 4.3. In addition, the angular fraction $\Phi_{\text{SP4} \rightarrow \text{T4}}$ along the minimal distortion pathway (see Appendix C) and the angle δ are listed in Table 4.3. The remarkable similarities between the numerical values of $\Phi_{\text{SP4} \rightarrow \text{T4}}$ and δ are more or less coincidental. The theoretical value of D was found between -28 and -40 cm^{-1} , while the rhombic parameter E lies between 0 and 5 cm^{-1} . This is in good agreement with the experimental D values, that were all in the range between -35 and -41 cm^{-1} , with the largest deviation (10 cm^{-1}) was found for **12**. Orientations of the easy-axis of magnetization are approximately the same for all complexes and approximately run through the centers of both binding pockets. **13** and **14** are depicted exemplarily for all tetrahedral complexes in Fig. 4.3. Due to the small variance of the experimental D values, a comparison with the theoretical ones proves difficult. It is worth noting, that the magnitude of the ZFS obtained from least-squares fits of the magnetization is very sensitive to the utilized model Hamiltonian and small fractions of impurities. Furthermore, the rhombic parameter E was not included in the least-squares fits to avoid overparametrization.

All complexes close to ideal tetrahedral coordination ($\Phi_{\text{SP4} \rightarrow \text{T4}} > 80\%$) exhibit calculated relaxation barriers between 77 and 88 K , whereas the more heavily distorted complexes reach a maximal value of 118 K (**11**). The only exception is found for complex **14**, where only $U_{\text{eff}} = 87 \text{ K}$ is predicted despite the second strongest distortion of the tetrahedral environment. This complex, however, shows also a large deviation from ligand mean planes of about 30 pm between the Co(II) ion and the ligand planes. In general, U_{eff} is overestimated by about $20\text{-}25\%$ compared to experiment. A look at the axiality of the g -tensor provides also a correlation with the degree of distortion. Small transversal elements ($g < 0.1$) are found only for complexes with mainly tetrahedral geometries, which, in theory, should prevent QTM. Despite having the most pronounced axiality, none of the complexes **9**, **12**, or **13** shows slow magnetic relaxation without applied dc field in the experiment. Furthermore, there is no obvious correlation between the size of the transversal g -elements and the magnitude of deviation from experimental U_{eff} -values. Nevertheless, with an applied dc field, considerable spin reversal barrier heights were found for all complexes, but surprisingly not for two of the more strongly distorted complexes, namely **14** and **16**. The two other remaining complexes **11** and **15** with $\Phi_{\text{SP4} \rightarrow \text{T4}} < 80\%$ on the other hand exhibit the highest measured relaxation bar-

riers. Unfortunately, both the experimental findings of the complete absence of SMM behavior for **16** as well as the slow magnetic relaxation with zero applied field for **8** cannot be explained by results from the *ab initio* calculations performed.

Although the exact prediction concerning slow magnetic relaxation behavior is not possible with the CASPT2/RASSI-SO results, trends concerning the ZFS are well reproduced. Thus, a systematic investigation on the effect of the distortion angle δ was performed. The dynamic properties of SMMs have already been investigated employing transition dipole moments between the SO states,^[98] but until recently, the calculation of this quantities was not yet implemented in the SINGLE_ANISO module.^[140]

4.2. Systematic Calculations on the Distortion of Tetrahedral Cobalt(II)

As seen above, the more distorted tetrahedral Co(II) complexes tended to show larger magnitudes of ZFS and spin reversal barriers. To obtain better performing SMMs, it might be helpful to systematically examine the influence of the distortion on the electronic properties. Therefore, the dependency of the energy spectrum of Co(II) from the distortion angle δ is further investigated. Due to the lack of experimental structures for the whole range of angles, model structures had to be utilized. The possible coordination modes of complexes with the substructure shown in Fig. 4.2 are depicted in Fig. 4.4. Square-planar coordination may be obtained by two bidentate ligands with large sterical hindrance, as found for **17** and **18**, or with a tetradentate ligands involving a diamine with a small distance between the imino nitrogens, as in **19** and **20**. Due to sterical reasons, the bidentate ligands show a *trans*-coordination, while the tetradentate ligands exhibit *cis*-coordination. Since most of the tetrahedral complexes do also

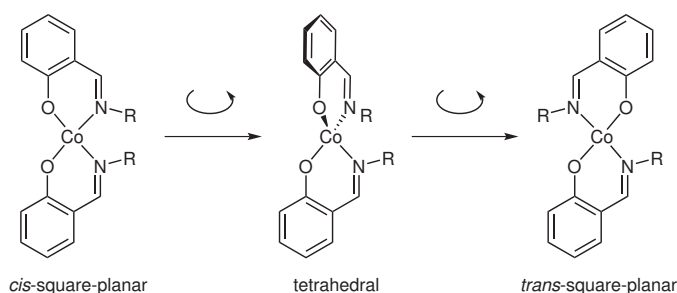


Figure 4.4.: Coordination modes of two Schiff-base ligands and Co(II).

4. Electronic Structure of Tetrahedral Cobalt(II) SMMs

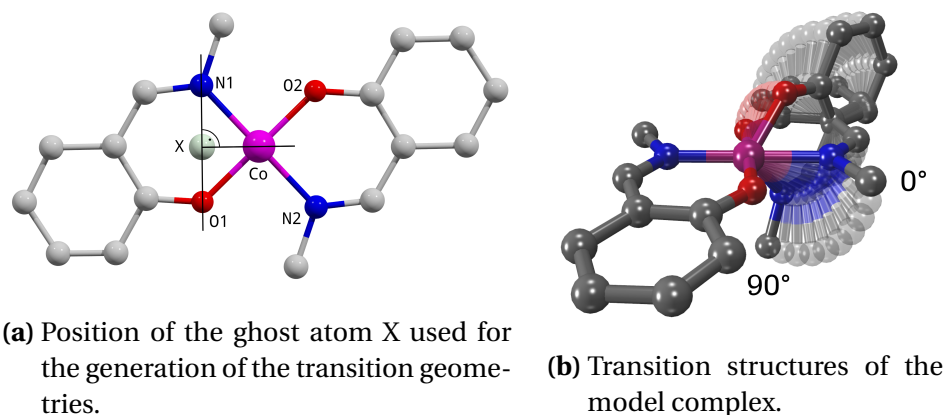


Figure 4.5.: Model complex used for the investigation of δ on the ground state properties of Co(II).

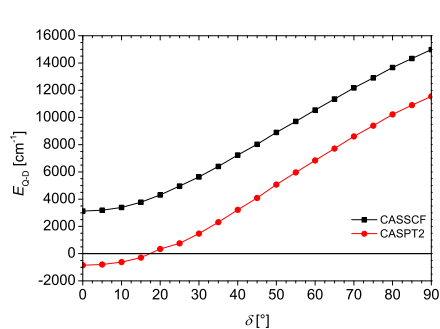
contain two bidentate ligand molecules, only the transition between tetrahedral and *trans*-square-planar coordination can be investigated without larger problems. Generating the transition structures between tetrahedral and *cis*-square-planar geometry would encounter difficulties, since the aniline moieties will inevitably come closer than their van-der-Waals radii.

The model ligand chosen for the subsequent investigations was the Schiff base of salicylic aldehyde and methylamine, a sub structure encountered practically in all previously mentioned Co(II) SMM candidates, except for the aliphatic nature of the *N*-substituent. Preliminary CASPT2 calculations on the model complex CoL_2 constructed from the optimized model complexes faced the problem of not predicting a low-spin ground state, even for the square-planar geometries. Furthermore, the structures with varying δ generated from a truncated experimental structure of a high-spin complex gave similar results. Hence, the crystal structure of a square-planar complex **17** was taken in order to obtain structures for the entire range between square-planar and tetrahedral coordination.

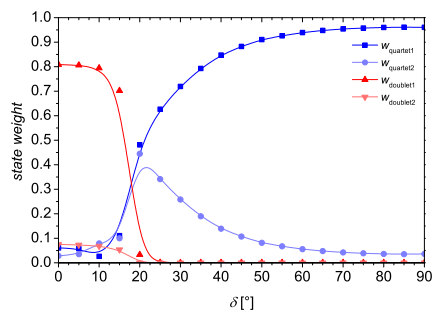
The structures with $0^\circ \leq \delta \leq 90^\circ$ in steps of 5° were then constructed with the bond-orientated manipulation tool implemented in the program AVOGADRO.^[141] The rotation axis of the salicylidene moiety containing O2 and N2 (Fig. 4.5a, right ligand) was chosen to be the connection $\overline{\text{CoX}}$, where X was placed at the perpendicular intersection from Co onto the connecting line $\overline{\text{N1 O1}}$, as shown in Fig. 4.5a. This led to the transition structures shown in Fig. 4.5b, that were used for the subsequent calculations.

The energy differences $E_{\text{Q-D}}$ between the lowest quartet and doublet states obtained

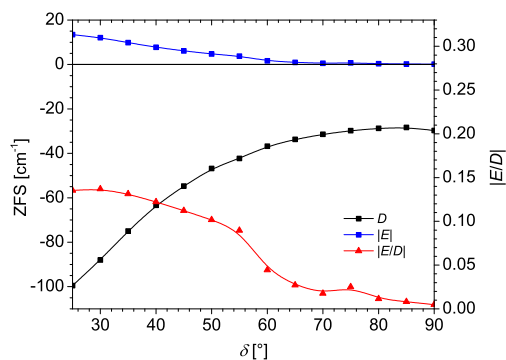
4.2. Systematic Calculations on the Distortion of Tetrahedral Cobalt(II)



(a) Quartet-doublet gap of CASSCF and CASPT2 energies.



(b) State weights of two lowest quartet and doublet states in the ground state SO function.



(c) ZFS parameters (left y -axis) and rhombicity (right y -axis).

Figure 4.6.: Plots of E_{Q-D} , state weights, and ZFS parameters for the model complex with respect to δ .

4. Electronic Structure of Tetrahedral Cobalt(II) SMMs

by both the CASSCF and CASPT2 methods are depicted in Fig. 4.6a. Both methods show an almost linear increase of E_{Q-D} with increasing δ for $\delta \geq 20^\circ$. The CASSCF results suggest a quartet ground state for all angles, whereas CASPT2 predicts a change of the ground-state below $\delta < 20^\circ$. The difference between quartet-doublet gaps E_{Q-D} obtained from CASSCF and CASPT2 calculations remains almost constant over the whole range of δ . RASSI-SO calculations were performed using the CASPT2 energies. The composition of the SO ground state concerning both the lowest two quartet and doublet states is depicted in Fig. 4.6b. Above $\delta = 50^\circ$, the state weight of the lowest quartet function is found to be at least 0.9. For lower angles δ , a stronger mixing of the two lowest quartet functions is observed, reaching almost a 1:1 ratio at $\delta = 20^\circ$. Correlating with the small degree of mixing of the quartet states, the ZFS parameters D and E (the absolute value $|E|$ was plotted, respectively) are relatively constant ($D \approx -30 \text{ cm}^{-1}$ and $|E|$ close to zero) between $\delta = 70^\circ$ and 90° . A larger distance to tetrahedral coordination leads to larger negative values for D , reaching almost -100 cm^{-1} at $\delta = 25^\circ$, while $|E|$ increases to 13 cm^{-1} . At the angle of 20° , a positive D is predicted. Even more obvious is the increase of the rhombicity $|\frac{E}{D}|$, that experiences a constant increase below $\delta = 60^\circ$.

So what exactly do these results mean for the desired structure of Co(II) SMMs? As already observed for complexes investigated in Section 4.1, a stronger deviation from ideal tetrahedral coordination up to $\delta = 60^\circ$ only offers D -values of maximal -40 cm^{-1} , corresponding to 115 K. Getting closer to square-planar coordination lets the rhombicity increase, and, hence, may be counterproductive for slow magnetic relaxation behavior due to opening of tunneling pathways. Contrary to this assumption, large rhombicities did not suppress SMM behavior for the strongly distorted complexes **11** and **16**, still leaving hope for a possible increase due to suitable ligands. Especially complexes in the range of $\delta \leq 60^\circ$ were not yet reported, probably demanding new ideas for the ligand design.

LINEAR COBALT(II) COMPLEXES

Within coordination chemistry, linear geometry is rarely observed, however, more or less well-known examples are the silver(I) complexes $[\text{Ag}(\text{NH}_3)_2]^+$ and $[\text{Ag}(\text{S}_2\text{O}_3)_2]^{3-}$, encountered already by undergraduate students in practical courses of general/inorganic chemistry. Otherwise, only few examples found their way into standard textbooks,^[121] suggesting that linear coordination is primarily promoted by a d^{10} configuration. By the right choice of ligands, however, a considerable number of stable linear complexes with d^1 – d^9 configuration has been synthesized and characterized.^[142]

Recently, a series of Fe(II) complexes^[143] with linear coordination was discovered to show slow magnetic relaxation. Furthermore, in 2013, the linear Fe(I) complex $[\text{K}(\text{crypt-222})][\text{Fe}(\text{C}(\text{SiMe}_3)_3)_2]$ was found to be a very potent SMM exhibiting a relaxation barrier of $U_{\text{eff}} = 325 \text{ K}$,^[53] a magnitude priorly unheard of for transition metal complexes. The origins for the outstanding performance were investigated by multiconfigurational calculations employing the CASSCF/NEVPT2/QDPT protocol as implemented in ORCA.^[144] It was found, that the weak ligand field generated by the linear coordination leads to an almost unquenched orbital momentum for the d^7 configuration. Hence, the almost degenerate lowest quartet states are then split heavily by spin-orbit coupling.

Although some (bent) linear Co(II) complexes have been reported during the last three decades,^[45,145–151] no dynamic susceptibility measurements were performed to examine their SMM behavior. Encouraged by the good agreement of the calculations with respect to the experimental data for the Fe(I) complex anion, it should be possible to predict the magnetic properties of linear Co(II) complexes respectively. For comparison, the spin-orbit energies of $[\text{Fe}(\text{C}(\text{SiMe}_3)_3)_2]^-$ were also calculated with the

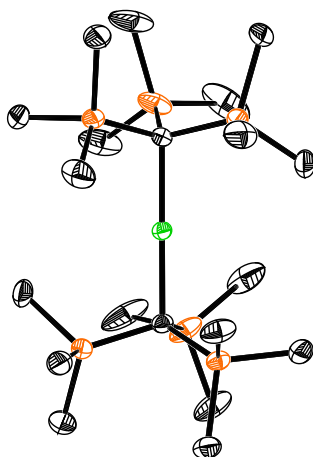


Figure 5.1.: Molecular structure of the anion of the complex $[\text{K}(\text{crypt-222})][\text{Fe}(\text{C}(\text{SiMe}_3)_3)_2]$ ^[53] (green: Fe, black: C, orange: Si). Hydrogen atoms were omitted for clarity.

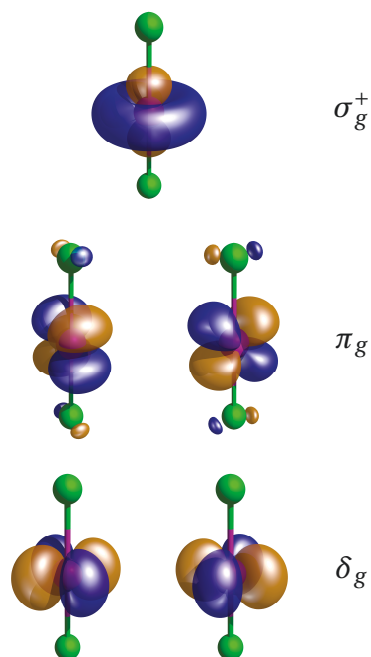
CASSCF/CASPT2/RASSI protocol, yielding very similar results to those reported by Zadrozny *et al.*^[53] Therefore, a set of two-coordinate Co(II) with a variety of donor atoms was chosen for spin-orbit calculations. While the electronic states of linear complexes are often discussed in terms of ligand field theory employing $D_{\infty h}$ symmetry (e.g. in^[145,146,149]), the existing literature remains inconsistent concerning the ground state in ideally symmetric d^7 complexes. Therefore, at first, a closer look at the simple molecule CoCl_2 was taken.

5.1. Energy Spectrum of CoCl_2

For a simplified explanation of the electronic structure for linear Co(II) complexes, the molecule CoCl_2 will be discussed. Though the complexes investigated later do not obey $D_{\infty h}$ symmetry, CoCl_2 will be studied within this point group. Since this point group is scarcely encountered, its character table is listed in Table 5.1. The electronic spectra of this molecule were measured at high temperatures in the gas phase^[152,153] and were interpreted by different researchers within the frameworks of ligand field theory^[152-154] and angular overlap model.^[155,156] Upon the application of a linear ligand field, the d -functions split into three sets, according to the character table: σ_g^+ (d_{z^2}), π_g (d_{xz} , d_{yz}), and δ_g (d_{xy} , $d_{x^2-y^2}$) (depicted in Fig. 5.2). Neglecting interelectronic repulsion, the expected energies for these orbitals would be in the order $\delta_g < \pi_g < \sigma_g^+$. For

Table 5.1.: Character table of the point group $D_{\infty h}$.

$D_{\infty h}$	E	$2C_{\infty}^{\Phi}$	\dots	$\infty\sigma_v$	i	$2S_{\infty}^{\Phi}$	\dots	∞C_2			
Σ_g^+	1	1	\dots	1	1	1	\dots	1	R_z (R_x, R_y)	$x^2 + y^2, z^2$	
Σ_g^-	1	1	\dots	-1	1	1	\dots	-1			
Π_g	2	$2\cos\Phi$	\dots	0	2	$-2\cos\Phi$	\dots	0			(xz, yz)
Δ_g	2	$2\cos 2\Phi$	\dots	0	2	$2\cos 2\Phi$	\dots	0			$(x^2 - y^2, xy)$
Φ_g	2	$2\cos 3\Phi$	\dots	0	2	$-2\cos 3\Phi$	\dots	0			
\dots	\dots	\dots	\dots	\dots	\dots	\dots	\dots	\dots			
Σ_u^+	1	1	\dots	1	-1	-1	\dots	-1	z (x, y)		
Σ_u^-	1	1	\dots	-1	-1	-1	\dots	1			
Π_u	2	$2\cos\Phi$	\dots	0	-2	$2\cos\Phi$	\dots	0			
Δ_u	2	$2\cos 2\Phi$	\dots	0	-2	$-2\cos 2\Phi$	\dots	0			
Φ_u	2	$2\cos 3\Phi$	\dots	0	-2	$2\cos 3\Phi$	\dots	0			
\dots	\dots	\dots	\dots	\dots	\dots	\dots	\dots	\dots			

**Figure 5.2.:** Average Natural Orbitals of the active space of the CoCl₂ molecule. The nomenclature implies $D_{\infty h}$ symmetry.

5. Linear Cobalt(II) Complexes

Table 5.2.: State energies [cm^{-1}] and natural orbital populations of CoCl_2 in terms of ligand field terms arising from the free ion ^4F term.

State	CASSCF energy	CASPT2 energy	Population of NOs				
			σ_g^+	π_g		δ_g	
$^4\Phi_g$	0	0	1.00	1.50	1.50	1.50	1.50
			1.00	1.50	1.50	1.50	1.50
$^4\Delta_g$	307	917	2.00	1.00	1.00	2.00	1.00
			2.00	1.00	1.00	1.00	2.00
$^4\Sigma_g^-$	1693	1644	1.00	1.57	1.57	1.43	1.43
$^4\Pi_g$	1659	1807	1.00	1.36	1.64	1.64	1.36
			1.00	1.64	1.36	1.64	1.36

handling a d^7 configuration, however, this zeroth order approximation is not helpful. The free Co(II) ion possesses a ^4F ground term, that is split into the ligand field states Φ_g ($M_L = 3$), Δ_g ($M_L = 2$), Π_g ($M_L = 1$), and Σ_g^- ($M_L = 0$).

First ligand field investigations suggested a Σ_g^- ground state with a very low lying first excited Φ_g state,^[152] while in later works by DeKock *et al.*,^[153] a Π_g ground state is proposed employing the angular overlap model. Furthermore, Smith suggested a Φ_g ground state.^[155] Introducing a parameter for the bonding nature, Lever *et al.*^[156] stated a dependence of the ground state upon the nature of bonding. With increasing π -bonding fractions, the ground states $\Sigma_g^- \rightarrow \Phi_g \rightarrow \Delta_g$ may arise. Further complication of the electronic situation may be expected by the possibility of the mixing of the 4s and $3d_{z^2}$ orbitals due to their similar symmetry race in $D_{\infty h}$. In 1998, Schwarz *et al.* reported DFT calculations on CoCl_2 and deduced a Σ_g^- ground state from the orbital energies, admitting the possible deficiencies of the method regarding multiterminant wave functions.^[157] All Co(II) halides CoF_2 , CoCl_2 , CoBr_2 , and CoI_2 have been investigated by Sliznev *et al.* with CASSCF/MCQDPT2 calculations,^[158] predicting a Δ_g ground state for all species, which would only agree with earlier results from Lever *et al.*^[156] for the case of large π -bonding fractions. Furthermore, Sliznev *et al.* used rather small basis sets for the ligand atoms for this calculations and neglected the double-d-shell effect proposed by Pierloot^[94] (five 3d- and one 4s-orbital in active space).

Due to this contradicting statements in the literature, CASSCF/CASPT2 calculation on CoCl_2 were performed. The experimental structure parameters from literature were

used ($r(\text{Co}-\text{Cl}) = 211.3 \text{ pm}$, $\angle(\text{Cl}-\text{Co}-\text{Cl}) = 180^\circ$).^[159] Deviating from the usual protocol, the ANO-RCC-VQZP basis set was employed for all atoms. The chosen CAS consisted of the 3d and 4d orbitals of the cobalt atom. As predicted above, the 4s orbital mixes into the σ_g^+ orbital, but with a rather small coefficient ($c = 0.18$). This clearly illustrates, how linear systems reach the boundaries of ligand field theory. Inclusion of an additional s-type orbital into the active space resulted in a diffuse active orbital, that had a natural population of 0.0008, and therefore does not give a meaningful increase of accuracy.

The state energies obtained from the CASSCF and CASPT2 calculations are listed in Table 5.2. While the CASSCF method yields a small energy gap of 307 cm^{-1} between the $^4\Phi_g$ ground state and the excited $^4\Delta_g$ state, CASPT2 calculations show a moderate separation of 917 cm^{-1} . The order of the higher states arising from the 4F term ($^4\Sigma_g^-$ and $^4\Pi_g$) switches upon the introduction of dynamic correlation. Due to the twofold degeneracy and the large orbital momentum of the $^4\Phi_g$ state ($M_L = 3$), strong spin-orbit coupling is observed and causes the $|\Omega\rangle$ states* to split heavily. RASSI-SO calculations show a complex mixing of the quartet states, producing the spectrum of spin-orbit states depicted in Fig. 5.3. The ground state is characterized by a large $\Omega = \pm\frac{9}{2}$ and an energetic separation of 295 cm^{-1} from the first excited SO state. This might be a good indication of the suitability of a linear coordination environment for the preparation of new SMMs with relaxation barriers well above the known U_{eff} values for Co(II) complexes.

5.2. Potential Linear Cobalt(II) SMM Candidates

Seven reported complexes were chosen from the literature. To obtain a comprehensive picture, the set of calculated complexes contained a large variety of donor environments: $\text{Co}(\text{Ar}^1)_2^\dagger$ (**21**),^[148] $(\text{Ar}^1)\text{CoN}(\text{SiMe}_3)_2$ (**22**),^[148] $\text{Co}(\text{NHAr}^2)_2^\ddagger$ (**23**), $\text{Co}(\text{NHAr}^3)_2^\S$ (**24**),^[149] $\text{Co}(\text{OAr}^2)_2$ (**25**), $\text{Co}(\text{OAr}^1)_2$ (**26**),^[151] and $\text{Co}(\text{SAr}^3)_2$ (**27**).^[147] The structures are depicted in Fig. 5.4. Structural parameters of the coordination environment of the Co(II) ion are summarized in Table 5.3. The molecular structures were truncated to a reasonable size by substituting moieties distant to the coordination environment by hydrogen atoms. Complexes **23** and **24** involve amide ligands with a hydrogen atom

*The angular momentum for linear molecules is denoted with the quantum number Ω instead of J .

[†] $\text{Ar}^1 = \text{C}_6\text{H}_3\text{-2,6-(C}_6\text{H}_3\text{-2,6-}i\text{Pr}_2)_2$

[‡] $\text{Ar}^2 = \text{C}_6\text{H}_3\text{-2,6-(C}_6\text{H}_2\text{-2,4-6-Me}_3)_2$

[§] $\text{Ar}^3 = \text{C}_6\text{H}_3\text{-2,6-(C}_6\text{H}_2\text{-2,4-6-}i\text{Pr}_3)_2$

5. Linear Cobalt(II) Complexes

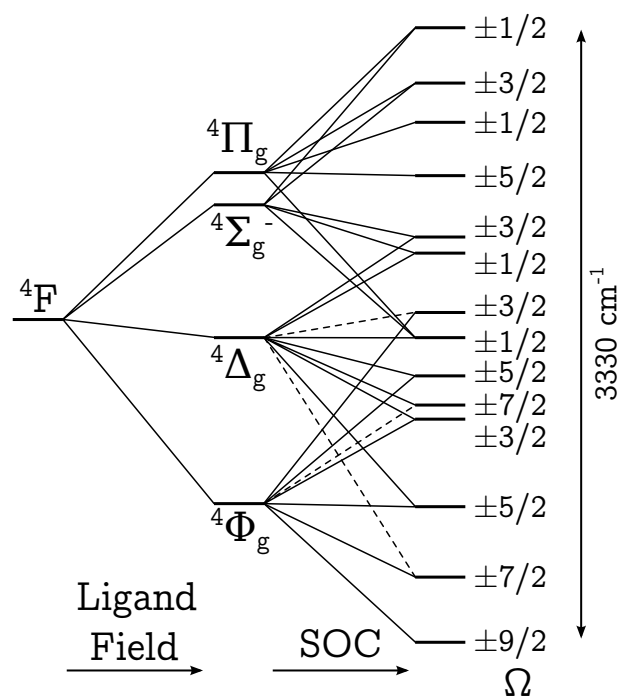


Figure 5.3.: Correlation diagram of the $4F$ state under the influence of a linear ligand field and subsequent spin-orbit coupling. The relative energies resemble the real ratio as taken from the CASPT2 results.

5.2. Potential Linear Cobalt(II) SMM Candidates

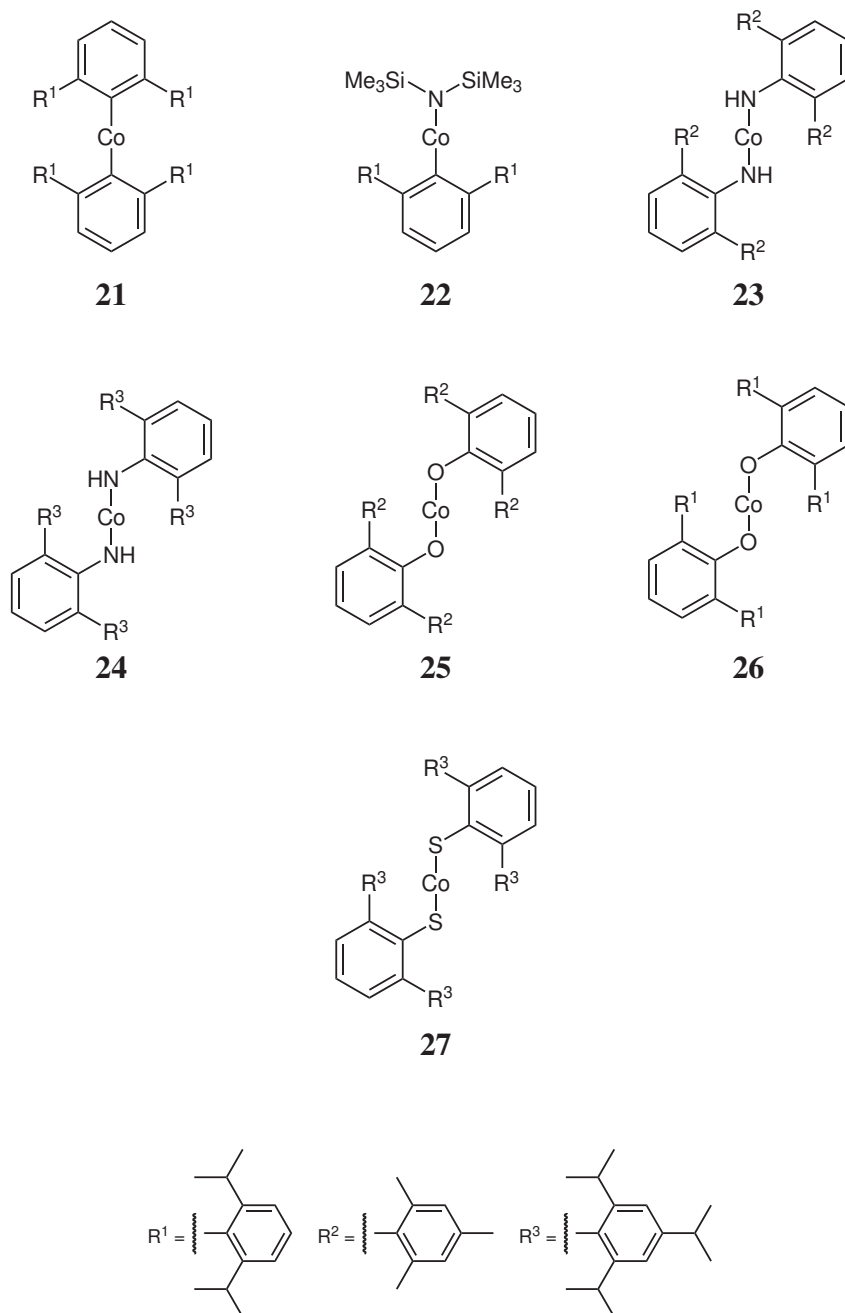


Figure 5.4.: Investigated two-coordinated cobalt(II) complexes.

5. Linear Cobalt(II) Complexes

bound to the coordinating nitrogen. Therefore, the influence of the position of the hydrogen was also investigated, but no significant differences of the energy levels between the crystal structure (riding atom) and the structure with optimized hydrogen coordinates was found.

The CASSCF results yield a quartet ground state for all linear complexes with a considerable separation from the lowest doublet state as well as from the excited 4P with a separation of at least 15000 cm^{-1} , respectively. In accordance with the results from section 4.1, introducing the dynamic correlation *via* the CASPT2 method decreases the relative energy of the lowest doublet state by $3000\text{--}4000\text{ cm}^{-1}$, not changing the ground state multiplicity for any of the complexes. All complexes show a low-lying excited quartet state with an energy gap of less than 1000 cm^{-1} . The energy differences ΔE_{CASPT2} between the two lowest quartet states are listed in Table 5.3, exhibiting a clear dependence on the bonding angle. Small separations are found for bond angles not too far from 180° . The smallest separations of $< 200\text{ cm}^{-1}$ are found for bond angles from 180 down to 159° , as found for **21**. Hence, an efficient mixing between the two lowest quartet states *via* spin-orbit coupling is possible. An increasing deviation from ideal linear geometry raises the splitting up to 413 and 896 cm^{-1} for **23** and **25**, respectively, that exhibit bond angles below 150° . Furthermore, a value of $\Delta E_{\text{CASPT2}} = 197\text{ cm}^{-1}$ for **27** seems large compared to the other complexes closer to linear coordination. The substantially elongated Co–S distance and softness of the donor atoms compared to the rest of the series might be the reason for differences of the energy spectra.

According to their CASPT2 energies, all complexes except the strongly bent ones (**23** and **25**) show similarities with ideal $D_{\infty h}$ coordination, and, hence, their ground state is well described as of $^4\Phi$ nature. For **21**, the overall splitting of the 4F state is of the same magnitude as for the other less bent complexes, probably due to the dominating influence of the aryl ligand and the weak π -donor capabilities of the aryl ligands. The ligands of the other complexes, however, are π -donors, but, unless their coordination angle deviates from 180° , the near-degeneracy of the ground state is maintained. Smaller angles in **23** and **25** induce a splitting of the $^4\Phi_g$ ground state, and, hence, lower the orbital momentum of the ground state.

The RASSI-SO calculations for all complexes show large spin reversal barriers U_{eff} (listed in Table 5.3) and low rhombicities $\frac{E}{D}$ (see Table D.7). The largest U_{eff} value was found for phenolate-coordinated complex **26** (582 K). Among the other complexes, **22**, **24**, and **27** were found to have the largest barrier heights ($\geq 500\text{ K}$) with bond angles

Table 5.3.: Structural parameters of the coordination environment, energy gap between the two lowest CASPT2 states, calculated relaxation barriers, and g -values of the two lowest Kramers doublets of the investigated linear Co(II) complexes.

Complex	D1	Co-D1	D2	Co-D1	\angle D1-Co-D2	ΔE_{CASPT2}	U_{eff}	KD	g_1	g_2	g_3
	[pm]	[pm]		[pm]	[$^\circ$]	[cm^{-1}]	[K]				
21	C	201.4	C	201.4	159.3	121	505	1	0.0708	0.0820	11.1778
								2	1.4729	1.4887	6.8150
22	C	197.3	N	187.5	179.0	88	554	1	0.0710	0.0873	11.4600
								2	1.3456	1.4500	7.1374
23	N	184.5	N	182.7	144.1	413	432	1	0.2165	0.2431	10.2192
								2	3.0056	3.3020	4.9510
24	N	186.5	N	186.5	180.0	71	519	1	0.1079	0.1155	10.6945
								2	1.2206	1.2991	6.3810
25	O	185.8	O	185.9	130.1	896	308	1	0.3940	0.4474	9.4901
								2	3.6193	3.6368	4.3167
26	O	184.1	O	184.1	180.0	32	582	1	0.1231	0.1339	11.2349
								2	0.9582	1.0119	6.8453
27	S	219.1	S	219.4	179.5	197	503	1	0.1933	0.2098	10.601
								2	1.4630	1.6524	6.1121

5. Linear Cobalt(II) Complexes

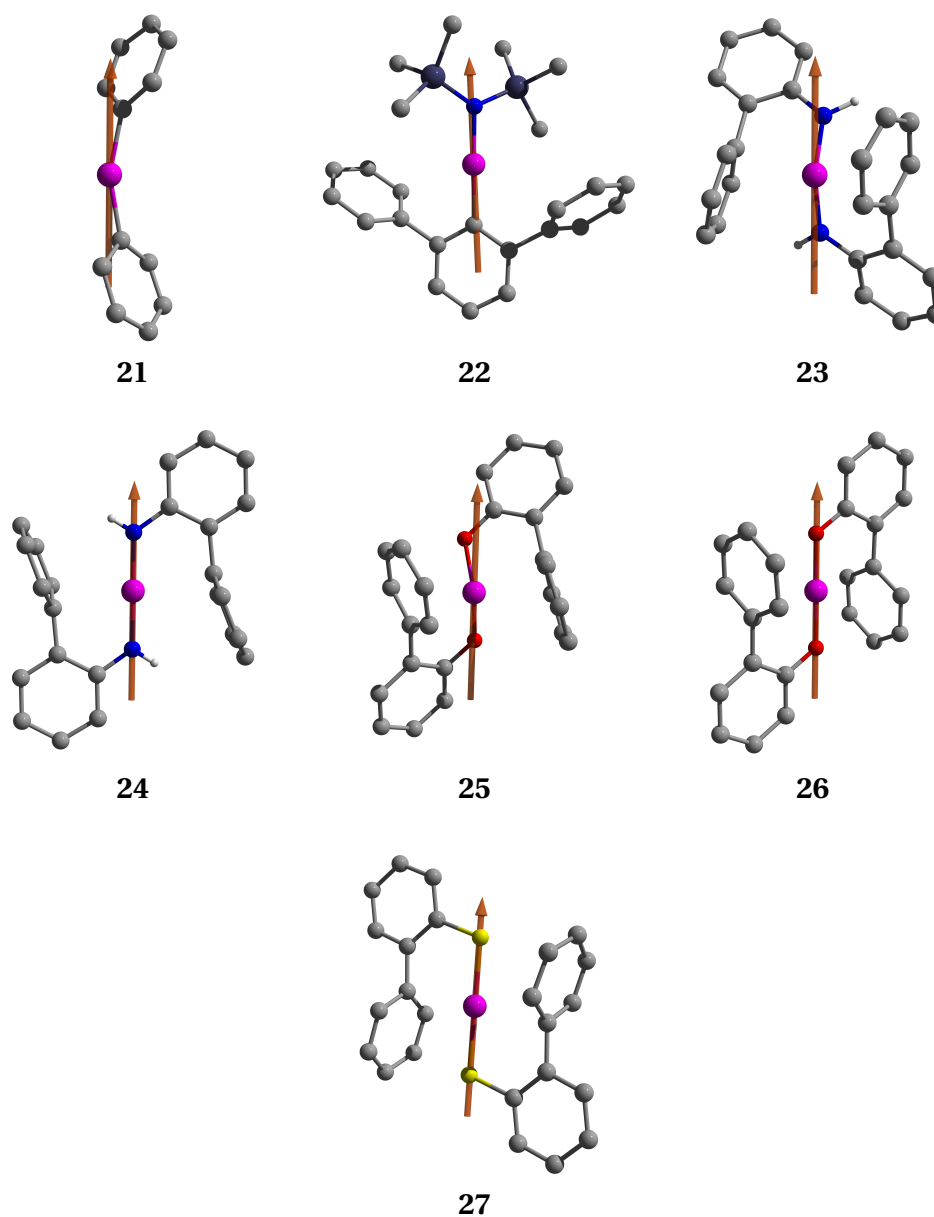


Figure 5.5.: Used models of the investigated two-coordinated cobalt(II) complexes with the main anisotropy axis of the ground Kramer's doublet. Hydrogen atoms are omitted for clarity.

5.2. Potential Linear Cobalt(II) SMM Candidates

close to 180°. Smaller angles (144° for **23**, 130° for **25**) afford significantly lower barriers (432 K and 308 K, respectively), which, nevertheless, are both still larger than values calculated in 4.1. Another property to be closely looked at is the axially of the ground state KD (listed in Table 5.3). A very strong axially is found for the complexes with coordinating carbon anions, showing $g_{x,y} < 0.1$. Somewhat larger, but still considerably low transversal g -values were obtained for the ideally linear complexes **24** and **26**. The largest transversal g -values (≥ 0.39) are found for **25** and go hand in hand with the lowest theoretical relaxation barrier. Therefore, the C-coordinated cobalt complexes and the linear complexes containing O- and N donors have to be considered to exhibit the largest relaxation barrier of the investigated complexes. The aryl ligands may furthermore cause very low tunneling probabilities due to the strong axially of the ground state KDs. But still, also all the other complexes show barrier heights of three to five times the size of the tetrahedral complexes investigated in Section 4.1. In comparison with $[\text{Fe}(\text{C}(\text{SiMe}_3)_3)_2]^-$, the linear Co(II) complexes might exhibit a substantially increased spin reversal barrier, since their calculated U_{eff} values are almost twice as large as the theoretical value obtained for the Fe(I) complexes (≈ 300 K). Still, the problem of the influence of tunneling processes on the relaxation dynamics remains hard to predict, but the obtained g -tensors of the ground state KDs look promising.

MULTICONFIGURATIONAL CALCULATIONS ON LANTHANIDE(III) SMMS

The chemical properties of lanthanide(III) ions are largely governed by the [Xe] core electron configuration. The 4f orbitals penetrate the xenon core appreciably and therefore are not able to overlap with ligand orbitals and, thus, do not participate in chemical bonding. Hence, all lanthanide(III) ions show very similar equilibrium geometries when coordinated by the same ligand system, except for a small contraction of the radius of the ions along increasing charge of the nucleus. Despite the relatively small influence of the ligand field on the 4f shell, it proves to be crucial for the SMM properties of lanthanide(III) complexes. In general, it is desired to stabilize the $|M_{J,\max}\rangle$ state, because it offers the largest magnetic momentum and, given the right coordination geometry, can exhibit the largest energetic separation of all $|M_J\rangle$ states.

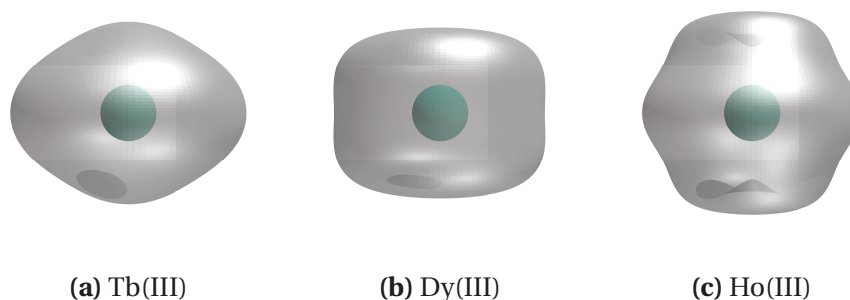


Figure 6.1.: Angular part of the charge density distribution of the $|M_{J,\max}\rangle$ state of lanthanide(III) ions important in SMM research.

6. Multiconfigurational Calculations on Lanthanide(III) SMMs

To obtain a qualitative picture, Rinehart and Long^[160] correlated the f-electron charge density distributions on the basis of a simple quadrupole treatment of the angular momentum J of the ground state multiplet according to Hund's rules. From this consideration, an oblate shape is expected for Ce(III), Pr(III), Nd(III), Tb(III), Dy(III), and Ho(III), whereas a prolate shape is expected for the free ions Pm(III), Sm(III), Er(III), Tm(III), and Yb(III). A more detailed picture is obtained by the calculation of charge density distributions of the particular $|\pm M_J\rangle$ states as reported by Sievers,^[161] which are drawn for the $|M_{J,\max}\rangle$ states of the ground multiplet for the free Tb(III), Dy(III), and Er(III) ions in Fig. 6.1. These are the most important SMM ions besides Ho(III). A stabilization of these states may be achieved by distributing the negative charges of the ligands to have the smallest electrostatic repulsion with these $|M_J\rangle$ states instead of other states of the J -multiplet. But especially for Er(III), a meaningful deduction of a suitable coordination environment for SMM purposes proves difficult, since, although formerly classified as prolate type ion, the charge density distributions for the $|M_J\rangle$ states of the $^4I_{15/2}$ term lack characteristic differences between them (see Fig. 6.2). This also manifests in the low number of reported examples for Er(III) SMMs.

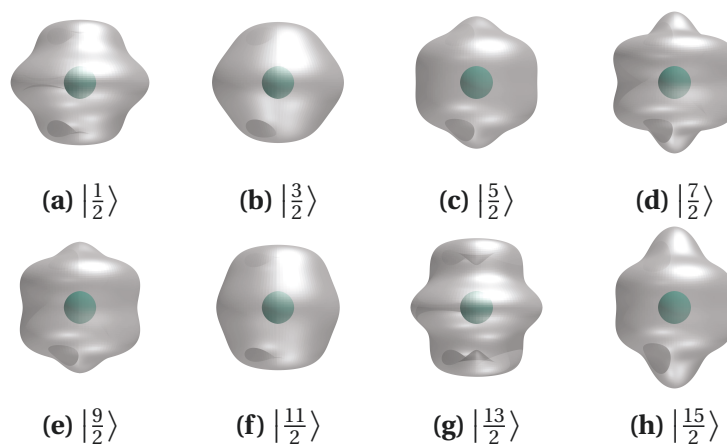


Figure 6.2.: Charge density distributions (only angular part plotted) of the $|M_J\rangle$ states of the $^4I_{15/2}$ term of the erbium(III) ion.

Obviously, all lanthanide(III) SMMs listed above contain late 4f ions. In contrast, the commercially available Nd-Fe-B and Sm-Co permanent magnets, known for large coercivities and remanences, utilize early lanthanides. The Sm(III) ion, which was earlier mentioned for having a prolate charge density in its $|\pm \frac{5}{2}\rangle$ doublet of the $^6H_{5/2}$ ground term, is hexagonally planar surrounded by cobalt atoms, thus preferring the KD with the largest M_J value. The Nd-Fe-B magnets are not as easily explained, because their

production involves the sintering of a ground powder, where neodymium is enriched on the surface of the particles.

6.1. Noteworthy Examples

The first examples of lanthanide(III) SMMs were double-decker complexes $\text{TBA}^+ \cdot [\text{Ln}(\text{Pc})_2]^-$ (Pc^{2-} = dianion of phthalocyanine), that were investigated by Ishikawa^[32] (structure depicted in Fig. 6.3). The Tb(III) and the Dy(III) complexes showed out-of-phase susceptibility signals with relaxation barrier heights of 331 K ($[\text{Tb}(\text{Pc})_2]^-$) and 40 K ($[\text{Dy}(\text{Pc})_2]^-$), respectively, for yttrium-doped crystals. The considerably larger U_{eff} value of $[\text{Tb}(\text{Pc})_2]^-$ may be attributed to the stabilization of the $|\pm 6\rangle$ doublet, which shows the most oblate-like charge distribution of the ${}^7\text{F}_6$ multiplet.^[160] Ideal S_8 symmetry ensures the pairwise degeneracy of all $|\pm M_J\rangle$ states for this interger-spin ion. For the Kramers ion Dy(III), the $|\pm M_J\rangle$ states are always degenerated, but the coordination environment encountered in $[\text{Dy}(\text{Pc})_2]^-$ does not provide a stabilizing influence on the $|\pm \frac{15}{2}\rangle$ state, but rather prefers the $|\pm \frac{13}{2}\rangle$ doublet due to its more planar charge distribution.^[160] By suitable substitution with thio-alkylether groups, U_{eff} values of $[\text{Tb}(\text{Pc})_2]^-$ analogues were increased to 871 K.^[35] Oxidizing the dianion of phthalocyanine to the monoanion, even a spin reversal barrier of 923 K may be achieved in the complex $[\text{Tb}^{\text{III}}(\text{Pc})_2]\text{Br}$.^[34] In case ideal axial symmetry is not met, non-Kramers ions like Tb(III) and Ho(III) may exhibit mixing of $|M_J|$ states mediated by off-diagonal matrix elements with the $M_J = 0$ state.

Although the $[\text{Tb}(\text{Pc})_2]^-$ complex anion showed a significantly larger relaxation

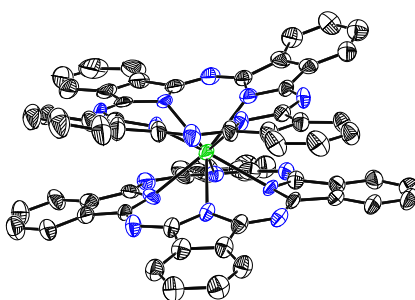


Figure 6.3.: Molecular structure of the $[\text{Tb}(\text{Pc})_2]^-$ anion (green: Tb, blue: N, black: C). The structure was reported by Loosli *et al.*^[162] Hydrogen atoms were omitted for clarity.

6. Multiconfigurational Calculations on Lanthanide(III) SMMs

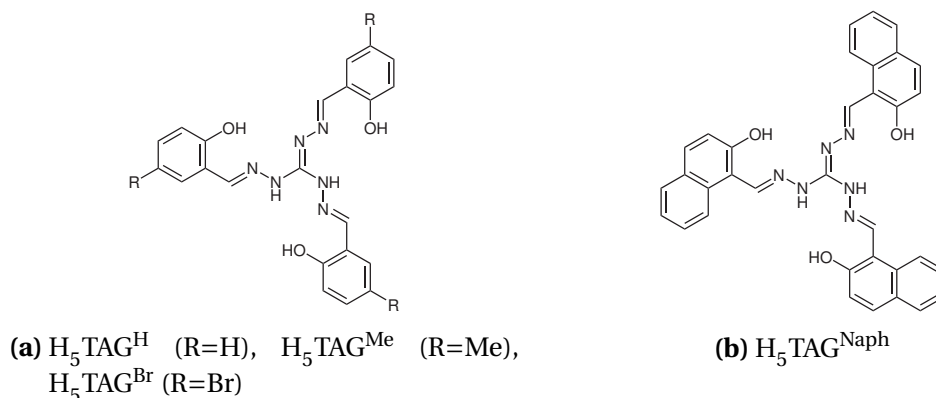


Figure 6.4.: Ligands used for the synthesis of the lanthanide(III) complexes.

barrier than $[Dy(Pc)_2]^-$, the latter lanthanide proved to exhibit much more likely SMM behavior, as the sheer number of reported examples shows.^[163] The largest yet reported U_{eff} was reported by Blagg *et al.* for the yttrium-diluted complex $[Dy_4K_2O(O^tBu)_{12}] \cdot C_6H_{14}$ exhibited a barrier height of $U_{eff} = 842$ K, thus increasing the already remarkable value of $U_{eff} = 693$ K for the undiluted complex.

In contrast to the numerous examples of dysprosium(III) SMMs, only four erbium(III) SMMs have been reported in the literature.^[164–167] The mononuclear complex $[(Cp^*)Er(COT)]$ ^[164] deserves a closer look due to its large barrier height. The two aromatic π -donors (COT, Cp^*) cause the $|\pm \frac{15}{2}\rangle$ KD to be lowered by 273 K relative to the $|\pm \frac{13}{2}\rangle$ KD (according to fits of the susceptibility), making it possible to achieve a barrier of $U_{eff} = 260$ K with zero applied dc field. The cyclic π -donors seem to fit well the charge density distribution of the $|\frac{15}{2}\rangle$ state (Fig. 6.2h), but for a generalization, more examples have to be investigated. The polyoxo metallate anion in $Na_9[Er(W_5O_{18})_2]$ ^[165] also exhibits SMM behavior in the absence of a dc field with a barrier height of 55 K. Larger aggregates involving two erbium(III) ions ($[KL_8][Er_2\{N(SiMe_3)_2\}_4(thf)_2(N_2)]$)^[166] and four erbium(III) ions ($[Er_4(salen)_6]$)^[167] need an applied dc field to show slow magnetic relaxation and exhibit barrier heights of $U_{eff} = 52$ K and $U_{eff} = 14$ K, respectively.

6.2. Dysprosium(III) and Erbium(III) Complexes with Triaminoguanidine-Based Ligands

Schiff-bases of triaminoguanidine (TAG) with derivatives of salicylic aldehyde are able to form trinuclear complexes with transition metals.^[38,54] Ln(III) ions also form com-

6.2. Dy(III) and Er(III) Complexes with Triaminoguanidine-Based Ligands

Table 6.1.: Triaminoguanidine-based complexes investigated with CASSCF/RASSI-SO procedure with their measured and calculated thermal relaxation barrier.

	Constitution	U_{eff} [K]
28	$[\text{Dy}(\text{H}_4\text{TAG}^{\text{H}})_2(\text{MeOH})_2]\text{Cl}$	131
29	$[\text{Dy}(\text{H}_4\text{TAG}^{\text{H}})_2(\text{MeOH})_2]\text{NO}_3$	262
30	$[\text{Dy}(\text{H}_4\text{TAG}^{\text{Me}})_2(\text{MeOH})_2]\text{NO}_3$	251
31	$[\text{Dy}(\text{H}_4\text{TAG}^{\text{Br}})_2(\text{MeOH})_2]\text{Cl}$	222
32	$[\text{DyNa}_2(\text{H}_4\text{TAG}^{\text{Naph}})_2(\text{MeOH})_2]\text{BPh}_4$	311
33	$[\text{Er}(\text{H}_4\text{TAG}^{\text{Naph}})(\text{H}_3\text{TAG}^{\text{Naph}})(\text{MeOH})_2]$	14

plexes with the TAG ligand system, but due to their significantly larger ion radii, they prefer a mononuclear constitution rather than a trinuclear one.^[168] The ligands used for the syntheses are depicted in Fig. 6.4. For the preparation, the hydrochlorides or hydronitrates of the ligands were utilized, and the Schiff-base ligand itself is set free by the application of a suitable base. The five dysprosium(III) complexes and one erbium(III) complex prepared by Schuch^[54] and Möller chosen for this investigation are listed in Table 6.1.

Among all Dy(III) complexes investigated, the metal ion is coordinated by two doubly deprotonated ligand molecules, each contributing a $[\text{N}_2\text{O}]$ donor set. For **33**, the coordination mode is the same, but one ligand is only singly deprotonated. The coordination sphere is saturated by two methanol molecules, giving rise to a $[\text{N}_4\text{O}_4]$ donor set, with two negative charges located at the phenolate-oxygen atoms. Other coordination scenarios, like a dimer involving a $[\text{N}_4\text{O}_3]$ donor set, also have been observed,^[54] but exhibit significantly lower U_{eff} values. Although only the complex cations present in the crystal lattice were considered for the calculations, certain differences emerging from the presence of different counterions or the lack thereof has to be mentioned. Due to the use of hydronitrates of the corresponding ligands, the complexes **29** and **30** involve a nitrate counterion in their crystal structure. The complexes **28** and **31**, however, were prepared employing the hydrochloride of $\text{H}_5\text{TAG}^{\text{H}}$, and therefore involve a chloride anion. A short look at Figs. 6.5a and 6.5b obviously shows structural differences among the complex cations. **32** features a BPh_4^- anion, because of the addition of NaBPh_4 . The erbium(III) complex **33** completely lacks an anion and, thus, one of the ligands is only threefold protonated. Furthermore, the complexes **28**, **29**, **30**, and **31** show dimeric units in their crystal structures, which are connected by hydrogen

6. Multiconfigurational Calculations on Lanthanide(III) SMMs

bonds between the methanol ligands and exhibit inversion symmetry. All of the dysprosium(III) complexes were found to show slow magnetic relaxation under zero applied dc field with relaxation barriers between 131 and 311 K (see Table 6.1). Magnetic interactions between the Dy(III) ions, especially within dimeric units, are expected to lower the height of the relaxation barrier by a considerable size. **33** does not exhibit SMM behavior without applied dc field. The thermal relaxation barrier found with an applied dc field of 1000 Oe is $U_{\text{eff}} = 14\text{ K}$, which is far below the values for the dysprosium(III) complexes. But nevertheless, with only four reported Er(III) SMMs, this has to be considered a success.

The complexes were investigated by CASSCF/RASSI-SO calculations to obtain the thermal relaxation barrier and the properties of the g -tensor of the mononuclear complexes. All CASSCF states of the highest multiplicity were considered, whereas only an arbitrary number of states of lower multiplicities was used (see Chapter 11). Further information was obtained utilizing the SINGLE_ANISO routine^[96] developed by Chibotaru *et al.*, allowing the simulation of variable field and variable temperature magnetic measurements as well as a decomposition of the spin-orbit wave functions into definite M_J projections. Magnetic properties arising from the dimeric constitution of some complexes were examined with the POLY_ANISO routine,^[98] considering both dipolar interaction and exchange interaction.

6.2.1. CASSCF/RASSI-SO Calculations on Dy(III) and Er(III) Complexes

Dysprosium(III) TAG Complexes

The CASSCF calculations for all Dy(III) complexes clearly show a ${}^6\text{H}$ ground multiplet for the Dy(III) ion. The overall splitting of the ${}^6\text{H}$ term is $\leq 1000\text{ cm}^{-1}$. Approximately 8000 cm^{-1} above the ground state, the lowest state of the excited ${}^6\text{F}$ multiplet can be found. The next-closest free ion multiplet is the ${}^4\text{G}$ term with a relative energy of $\approx 25000\text{ cm}^{-1}$. The lowest doublet state follows at $\geq 37000\text{ cm}^{-1}$ and is therefore very unlikely to mix into the low-lying spin-orbit functions. The two lowest CASSCF sextet states are nearly degenerated with a small energy difference (E_1) between 1.4 cm^{-1} for **32** and 8.7 cm^{-1} for **28** (see Table 6.2). The energy of the second excited state (E_2) was found to lie between 205 for **31** and 383 cm^{-1} for **32**. According to Aravena *et al.* first excited CASSCF state need to be close in energy to the ground state, whereas the second excited state should lie well above the ground state^[169] to achieve slow magnetic relaxation behavior.

6.2. Dy(III) and Er(III) Complexes with Triaminoguanidine-Based Ligands

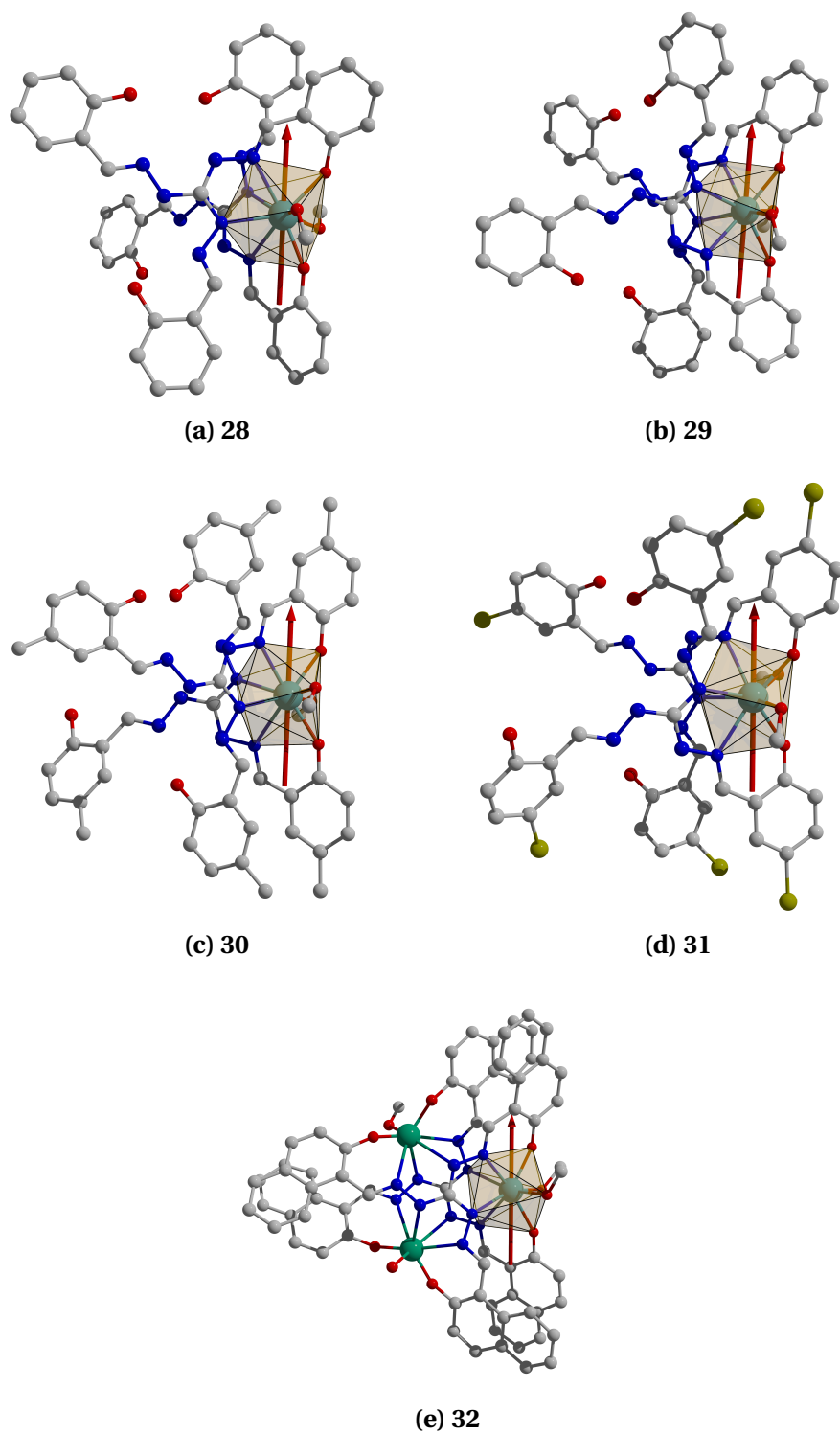


Figure 6.5.: Structure of the mononuclear units of the Dy(III) complexes. The arrow designates the main anisotropy axis of the ground state KD (easy-axis of magnetization).

6. Multiconfigurational Calculations on Lanthanide(III) SMMs

Table 6.2.: Energies of the low-lying CASSCF sextet states (in cm^{-1}), and weights of the most involved states in the ground Kramers doublet for the dysprosium(III) complexes (w_{si} and w_{qi} : weights of the i th sextet respectively quartet state for the ground state spin-orbit function).

	E_1	E_2	w_{s1}	w_{s2}	w_{q1}	w_{q2}
28	8.7	233.7	0.441	0.449	0.020	0.020
29	4.3	258.0	0.452	0.458	0.021	0.021
30	3.0	308.7	0.455	0.458	0.021	0.021
31	2.2	204.8	0.451	0.455	0.018	0.019
32	1.4	383.3	0.470	0.471	0.022	0.022

RASSI-SO calculations were performed including all 21 sextet states, 128 quartet states, and 32 doublet states. The spin-orbit functions obtained reproduce the expected energy spectrum of eight KDs, of the ${}^6\text{H}_{15/2}$ multiplet of the Dy(III) ion. The excited ${}^6\text{H}_{13/2}$ term is separated by almost 3000 cm^{-1} from the ground state. A closer look on the energies of the spin-orbit states reveals significant differences between the Dy(III) complexes. The calculated energies of the first excited Kramers doublet are listed in Table 6.3 and range from 241 for **31** to 402 K for **32**. Obviously, U_{eff} is constantly overestimated compared to the observed relaxation barrier heights. For **28**, the largest deviation was found with $U_{\text{eff, calc}}$ approximately 50% larger than the value extracted from the ac SQUID measurements. The calculations for the other complexes show deviations of $\leq 25\%$.

For all Dy(III) complexes, a strong mixing of the two lowest spin-free sextet wave functions is observed with weights of ≈ 0.45 in the lowest spin-orbit wave functions (see Table 6.2), leading to an overall contribution of ≥ 0.9 . The ground KDs do also involve the first two quartet CASSCF functions with weights close to 0.02. Mixing of other spin-free states into the ground state doublets is not observed.

At first, the differences between the calculated and measured relaxation barriers seem large, but considering the necessary negligence of other relaxation pathways, this maybe also a good indication for the existence of such channels. Hence, only processes relying on the thermal population of the first excited KD of single ions (Orbach relaxation, TAQT) can be accounted for in the CASSCF/RASSI-SO method. The interactions themselves are addressed later in Section 6.2.2 for the interpretation of the dc SQUID measurements.

Table 6.3.: Measured and calculated thermal relaxation barriers U_{eff} , and parameters used for the correlation.

	U_{eff} [K]		$\angle(\text{O-Dy-O})$ [°]	g_{\perp}
	exp.	calc.		
28	131	250	113.3	0.0051
29	262	292	115.1	0.0039
30	251	326	112.6	0.0014
31	222	241	105.1	0.0020
32	311	402	126.3	0.0011

To explain the differences within the series of Dy(III) complexes, additional structural and electronic properties were considered for correlations with U_{eff} (see Table 6.3). A coordination environment involving 8 donor atoms offers a large degree of freedoms for different distortions. The Continuous Shape Measure^[170] (CShM) was employed to characterize the coordination polyhedra of all Dy(III) complexes, but no significant differences manifested in the similarities S_i for all considered geometries (see Appendix C.2). In addition, it does not account for the different charges localized on the donor atoms.

Ruiz *et al.* proposed the evaluation of the electrostatic potential for statements concerning the SMM behavior.^[169] Only the phenolate-oxygen atoms carry a negative charge and therefore, should have the largest influence on the potential interacting with the Dy(III) ion. Thus, the angle between the Dy(III) ion and the two phenolate oxygens $\angle(\text{O-Dy-O})$ (listed in Table 6.3) might be correlated with the relaxation barrier. The largest $\angle(\text{O-Dy-O}) = 126.3^\circ$ is found for complex **32**, coinciding with the largest measured and calculated relaxation barrier. **31** shows the smallest angle of 105.1° , correlating with the smallest calculated U_{eff} , but not with the minimum experimental U_{eff} . The remaining three complexes exhibit a $\angle(\text{O-Dy-O})$ rather close to each other, but with no clear trend concerning their SMM behavior. Hence, a magnetostructural correlation with this simple parameter does not yield meaningful statements

To unravel the nature of the SO wave functions, the g -tensors of the eight lowest KDs were calculated using a pseudospin formalism for eight pseudospins $\tilde{S} = \frac{1}{2}$, one for each KD. It is clearly seen in Fig. 6.5, that the main anisotropy axis of the ground state KD is similarly orientated for all Dy(III) complexes. They are best described as parallel to the vector defined by the two phenolate-oxygens. All complexes exhibit a strong axially of the g -tensor of the ground state. Nonetheless, all Dy(III) complexes

6. Multiconfigurational Calculations on Lanthanide(III) SMMs

Table 6.4.: Energies and g-values of the spin-orbit states belonging to the ${}^6\text{H}_{15/2}$ multiplet.

	KD	ΔE [cm^{-1}]	ΔE [K]	g_1	g_2	g_3	g_{\perp}	$\angle(\vec{g}_3(1) - \vec{g}_3(i))$ [$^{\circ}$]
28	1	0	0.0	0.0015	0.0049	19.4944	0.0051	0.0
	2	174	250	0.0568	0.1348	15.7786	0.1463	10.7
	3	265	381	0.2761	0.4231	13.2474	0.5052	8.3
	4	375	539	2.1366	2.5683	11.4461	3.3408	16.1
	5	447	643	3.2282	6.0101	9.4867	6.8222	54.3
	6	512	737	1.4309	4.0833	13.8368	4.3268	89.3
	7	560	805	0.6006	1.4831	18.3676	1.6001	86.7
	8	620	892	0.1332	0.1841	18.3233	0.2272	87.9
29	1	0	0	0.0017	0.0035	19.6662	0.0039	0.0
	2	203	292	0.0746	0.1757	16.2917	0.1909	14.6
	3	293	421	0.1515	0.2845	13.3116	0.3223	5.8
	4	385	554	1.7212	2.2261	11.2495	2.8139	12.8
	5	455	655	3.9199	5.9987	9.4616	7.1659	53.2
	6	517	744	1.2363	3.8596	14.1672	4.0528	84.3
	7	560	806	0.9091	1.5079	18.4718	1.7607	89.8
	8	639	919	0.0835	0.1517	18.7401	0.1732	90.9
30	1	0	0	0.0006	0.0013	19.6877	0.0014	0.0
	2	227	326	0.0319	0.0772	16.1105	0.0835	9.4
	3	320	461	0.0824	0.1465	13.3992	0.1681	6.4
	4	417	600	0.3808	0.5946	12.0080	0.7061	12.3
	5	487	700	2.4051	3.1542	10.2629	3.9665	26.6
	6	534	768	1.5757	5.4651	9.5749	5.6877	63.7
	7	560	805	2.6370	3.8435	14.9751	4.6611	85.1
	8	702	1010	0.0026	0.0309	18.9659	0.0310	89.1
31	1	0	0	0.0003	0.0020	19.6727	0.0020	0.0
	2	167	241	0.1751	0.3651	16.2328	0.4049	22.6
	3	218	314	0.1966	0.6686	14.6618	0.6969	33.9
	4	311	448	0.9866	1.7602	11.4802	2.0178	12.8
	5	415	598	1.9088	4.2251	8.4083	4.6363	22.1
	6	505	727	1.9937	3.6907	10.9072	4.1948	68.9
	7	569	819	0.9702	3.5866	14.9369	3.7155	89.1
	8	662	953	0.2217	0.5321	19.3581	0.5764	63.4
32	1	0	0	0.0007	0.0008	19.8227	0.0011	0.0
	2	280	402	0.0775	0.1005	16.8140	0.1269	7.5
	3	435	627	0.6560	0.7840	13.5342	1.0222	5.5
	4	553	795	1.7508	2.6505	10.2336	3.1765	13.0
	5	638	918	4.6692	5.7758	9.2760	7.4271	75.4
	6	748	1076	0.5552	1.9509	14.8547	2.0284	86.3
	7	833	1199	0.8481	3.0483	13.4828	3.1641	81.2
	8	852	1226	0.8063	3.8707	14.7310	3.9538	88.1

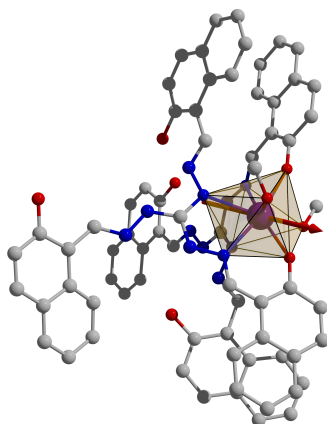


Figure 6.6.: Structure of **33**. The arrow designates the main anisotropy axis of the ground state KD (easy-axis of magnetization).

show small non-axial components of the ground state g -value, that might cause the relaxation barrier height U_{eff} to be reduced by tunneling processes. Transversal elements (also listed as geometric mean $g_{\perp} = \sqrt{g_1^2 + g_2^2}$) show a magnitude of ≤ 0.0051 . The largest g_{\perp} is found for **28**, which is one possible reason for the lowering of U_{eff} in case of the real compound compared to the calculated monomeric species. For the remaining complexes, no clear correlation of the size of transverse elements of g and U_{eff} is observed. Relatively small differences of $\approx 10\%$ between $U_{\text{eff,exp}}$ and $U_{\text{eff,calc}}$ for **29** ($g_{\perp} = 0.0039$) and **31** ($g_{\perp} = 0.0020$) are in contrast with larger errors ($> 20\%$) for **32** and **30** despite having the smallest g_{\perp} -values. g_3 is close to 20 for all complexes, which is typical for a $|M_J = \pm \frac{15}{2}\rangle$ doublet.

The angles between the g_3 -axis of the SO ground states and the other KDs were also calculated (listed in Table 6.4), but no clear correlations with the measured or calculated relaxation barriers were found.

Erbium(III) TAG Complex

CASSCF calculations for **33** considering 35 quartet states and 112 doublet states yield a ^4I ground term, which is split by $\approx 500\text{ cm}^{-1}$. The two lowest quartet states are almost degenerate with a separation of 5 cm^{-1} . The lowest excited multiplets are of ^4F and ^2H character, found both at $\approx 18000\text{ cm}^{-1}$. From RASSI-SO calculations, a $^4\text{I}_{15/2}$ ground multiplet is obtained. Relative energies and main values of the g -tensors of the spin-orbit states are listed in Table 6.5. The orientation of the main anisotropy

6. Multiconfigurational Calculations on Lanthanide(III) SMMs

Table 6.5.: Energies and g-values of the lowest Kramers doublets of **33**.

KD	ΔE [cm ⁻¹]	ΔE [K]	g_1	g_2	g_3	g_{\perp}	$\angle(\vec{g}_3(1) - \vec{g}_3(i))$ [°]
1	0	0	0.9872	3.4341	13.1879	3.5732	0.0
2	30	43	0.1737	2.8325	10.7769	2.8378	87.3
3	62	89	2.9682	4.6355	7.5788	5.5044	77.8
4	130	188	1.5844	3.6129	10.4462	3.9450	55.4
5	185	267	0.0999	5.3473	6.5634	5.3482	39.7
6	230	331	1.0492	4.6819	12.3933	4.7980	49.1
7	319	459	0.0321	0.2086	15.2309	0.2111	48.5
8	380	546	0.0657	0.1102	15.5803	0.1283	67.4

Table 6.6.: Decomposition of the RASSI wave functions corresponding to the lowest ⁴I_{15/2} multiplet in wave functions with definite projection of the total angular momentum $|M_J\rangle$.

M_J	w.f. 1	w.f. 2	w.f. 3	w.f. 4
-15/2	0.592	0.000	0.066	0.000
-13/2	0.119	0.000	0.003	0.010
-11/2	0.120	0.004	0.012	0.065
-9/2	0.020	0.001	0.048	0.104
-7/2	0.018	0.023	0.001	0.249
-5/2	0.044	0.018	0.095	0.102
-3/2	0.016	0.000	0.088	0.044
-1/2	0.021	0.004	0.078	0.036
1/2	0.004	0.021	0.036	0.078
3/2	0.000	0.016	0.044	0.088
5/2	0.018	0.044	0.102	0.095
7/2	0.023	0.018	0.249	0.001
9/2	0.001	0.020	0.104	0.048
11/2	0.004	0.120	0.065	0.012
13/2	0.000	0.119	0.010	0.003
15/2	0.000	0.592	0.000	0.066

axis is depicted in Fig. 6.6. Since Er(III) is a half-integer spin system, all SO states are doubly degenerate. Ground and first excited KD, both composed of more than five CASSCF states (weight > 0.05), are separated by 30 cm^{-1} . The large transversal elements of the g -tensor ($g_1 = 0.9872$, $g_2 = 3.4341$) of the ground state KD suggest, that the $|\pm \frac{15}{2}\rangle$ KD strongly mixes with the other $|M_J\rangle$ states. The easy-axis of magnetization (g_3) is aligned between the two negatively charged phenolate-oxygens, almost perpendicular to the orientation found in the Dy(III) complexes. A mixed nature of the RASSI-SO wave functions is further confirmed by their decomposition in definite $|M_J\rangle$ wave functions. Instead of the complex coefficients c obtained from the SINGLE_ANISO routine, the real values of the weights $w = c^* \cdot c$ are listed in Table 6.6, revealing a pronounced mixing of the $|\pm \frac{15}{2}\rangle$ KD, mainly with the $|\pm \frac{13}{2}\rangle$ and $|\pm \frac{11}{2}\rangle$ doublets. The first excited SO wave function is also a mixture of several $|M_J\rangle$ states, primarily the $|\pm \frac{9}{2}\rangle$, $|\pm \frac{7}{2}\rangle$, and $|\pm \frac{5}{2}\rangle$ functions. Hence, the mixing of the $|\pm \frac{15}{2}\rangle$ state with other $|M_J\rangle$ states allows tunneling between the two degenerate ground state functions, thus preventing SMM behavior without applied magnetic field. The orientation of the easy-axis of magnetization may be qualitatively explained with the charge distributions depicted in Fig. 6.2. The two peaks along the z -axis will experience the strongest electrostatic repulsion from the negative charges of the phenolate-oxygens, thus turning the ions z -axis to the lowest electrostatic potential, which is obviously found between the two mentioned donor atoms. Due to the non-specific shapes of the other $|M_J\rangle$ states, they readily mix into the ground state SO wave function.

6.2.2. Simulations of $\chi_M T$

Unlike susceptibility measurements for 3d metal ions, where they readily yield valuable information of the electronic structure, static dc measurements for lanthanide ions are hard to analyze due to the large number of parameters and uncharacteristic shapes of the plots. Hence, a way to decrease the number of parameters would be very useful for the interpretation of the susceptibility data. As aforementioned, it has been shown, that the energy ladder and g -values of low-lying spin-orbit states can be calculated in the framework of CASSCF and RASSI-SO methodologies. Estimating the dynamic properties e.g. U_{eff} and the possibility of tunneling processes, proved to be challenging. But nevertheless, the results may enable one to gain more insight into the static magnetic properties. The obtained SO wave functions can be used to calculate the static magnetic properties like $\chi_M T(T)$ and $M(H)$ with a procedure implemented in the SINGLE_ANISO module of the MOLCAS program package.

6. Multiconfigurational Calculations on Lanthanide(III) SMMs

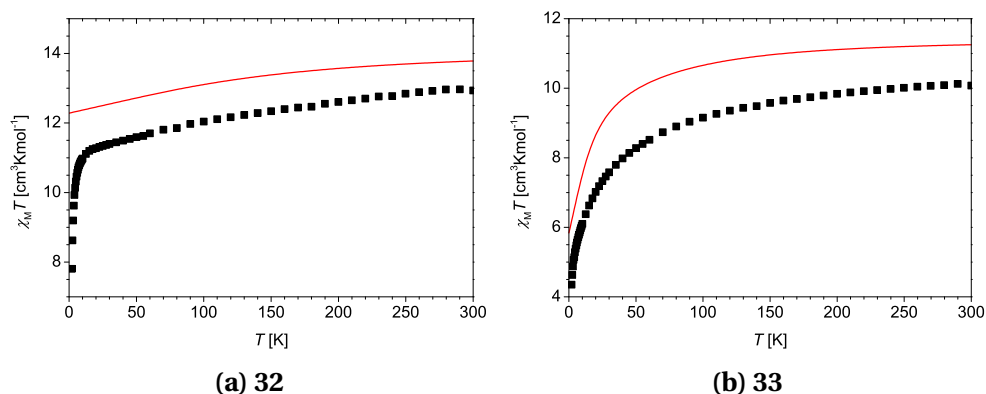


Figure 6.7.: Measured and calculated values for the complexes containing monomeric units. The black squares represent the measured data, the lines are simulated values using the RASSI spin-orbit functions.

Monomeric Complexes

For the monomeric complexes **32** and **33**, no strong magnetic interactions between paramagnetic ions are expected. Therefore, a simulation only considering a single complex molecule is expected to give a reasonable approximation for the solid state. The $\chi_M T$ values calculated for **32** and **33** are depicted in Fig. 6.7 together with the experimental values. The theoretical values overestimate the measured $\chi_M T$ values by $\approx 10\%$, but the temperature dependence is met to a reasonable degree. For **32**, the decrease of $\chi_M T$ below 10 K is not reproduced, but since for higher temperatures the shape fits well, neglected weak intermolecular interactions should be responsible for the low-temperature behavior. The theoretical $\chi_M T$ values for **33** model well the decrease for low temperatures. Since a steady decrease upon cooling is found for the entire temperature range, the origin of this behavior has to lie within the electronic structure of the single Er(III) ions. A small energy gap of the lowest KDs of **33** explains the population of smaller magnetic moments already at higher temperatures, thus decreasing $\chi_M T$ at higher temperatures. Due to the good agreement of theory and experiment considering the temperature dependence, intermolecular interactions are assumed to have a small influence on the magnetic behavior of **33**.

Dimeric Complexes

As mentioned above, the four complexes **28**, **29**, **30**, and **31** involve dimeric units of the complex cations, that are connected by hydrogen bonds between the methanol

coligands. The structures of these dimers are depicted in Fig. 6.8. Due to the considerably smaller Ln–Ln distances found in the dimeric complexes compared to the monomeric complexes, significant magnetic interactions have to be expected. This might also explain the systematically overestimated U_{eff} values for the dimeric species. Here, the magnetic dipole-dipole interaction as well as the exchange interaction were included into the considerations, due to their similar magnitude in lanthanide chemistry. Within the POLY_ANISO module developed by Chibotaru *et al.*,^[98] it is possible to calculate the exact dipolar interaction using the SO wave functions, with the classic expression:

$$E = \frac{\mu_0}{4\pi r^3} \left(\boldsymbol{\mu}_1 \cdot \boldsymbol{\mu}_2 - \frac{3}{r^2} (\boldsymbol{\mu}_1 \cdot \mathbf{r})(\boldsymbol{\mu}_2 \cdot \mathbf{r}) \right). \quad (6.1)$$

The calculation of the exact exchange interaction, however, would demand the CASSCF calculations to be carried out with an active space including the 4f-orbitals of interacting lanthanide ions and a particular number of ligand orbitals. With $14 + x$ active orbitals, this would easily exceed available computational resources, since the number of CSFs scales factorially. Therefore, the exchange interaction is treated with an Ising Hamiltonian, where ideal axuality of the pseudospins \tilde{S} is assumed:

$$\hat{H}_{\text{Ising}} = - \sum_{i=1}^N \sum_{j>i}^N J_{ij} \hat{S}_{iz} \hat{S}_{jz}. \quad (6.2)$$

Although the arbitrarily chosen exchange parameter J_{ij} is isotropic, the anisotropic exchange interactions can be modeled by the inclusion of several KDs for each ion. In this investigation, the eight lowest KDs were included. Furthermore, the separate treatments of the dipolar and exchange interaction gives the possibility to deduce their influences on the exchange spectrum, which is not possible by experimental static SQUID measurements.

6. Multiconfigurational Calculations on Lanthanide(III) SMMs

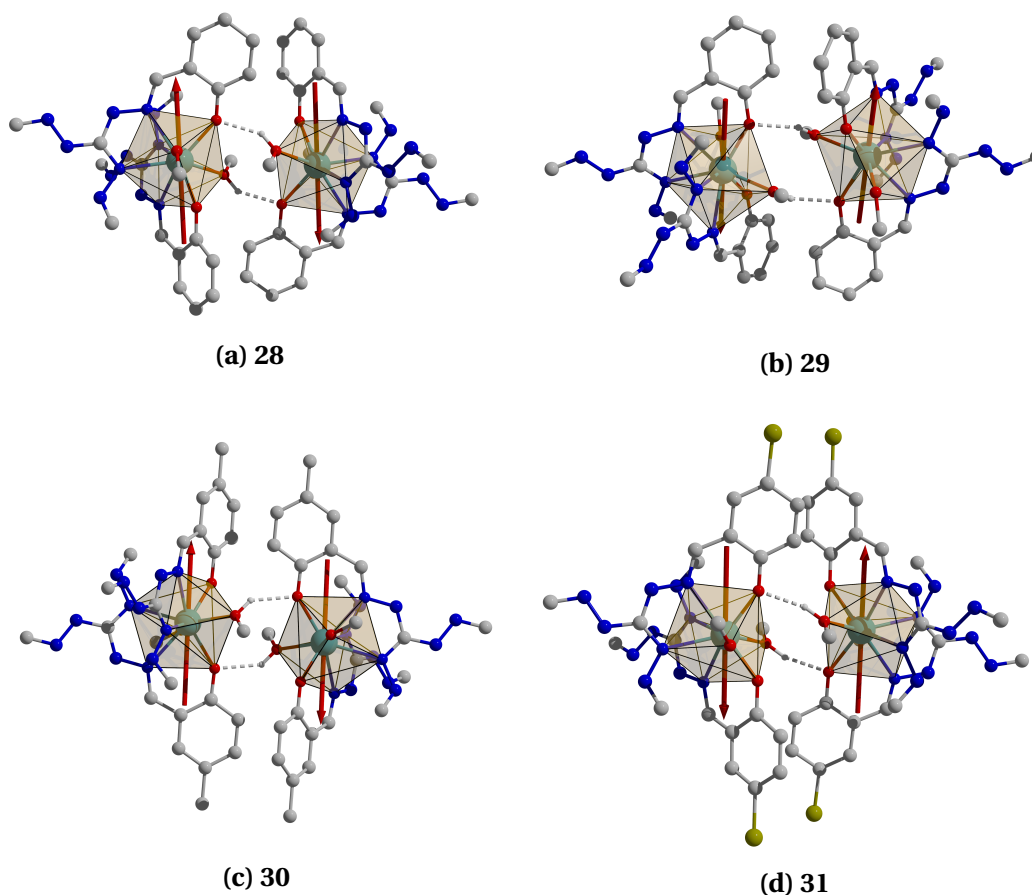


Figure 6.8.: Dimeric units calculated with the POLY_ANISO module.

The calculated $\chi_M T$ values including dipolar interactions and arbitrary magnitudes of the exchange interaction ($J = 0, \dots, -0.2 \text{ cm}^{-1}$) are depicted in Fig. 6.9. Theoretical $\chi_M T$ values were found to be smaller than experimental values, if the molar mass of the dimer from the crystal structure was used to process the measured data. But from previous works, it proved to be very difficult to determine the exact molar weights for the used powder samples due to the loss of co-crystallized solvent molecules. Therefore, the experimental data was plotted using the molar weights from the single crystal structures multiplied with a scaling factor f to match the height of the calculated $\chi_M T$ curves (see captions in Fig. 6.9 for f). In the temperature range above 100 K, the results for all simulations do not differ much for all of the complexes. But for low temperatures, the decrease of the $\chi_M T$ values cannot be reproduced with the theoretical results for the mononuclear units. Purely dipolar interaction significantly improves the agreement with the experiment. Additional inclusion of the exchange interaction

6.2. Dy(III) and Er(III) Complexes with Triaminoguanidine-Based Ligands

further improves the theoretical description for some of the complexes. For **29** and **30**, an exchange parameter of $J = -0.05 \text{ cm}^{-1}$ gives the best result, **28** is best described with $J = -0.1 \text{ cm}^{-1}$. Simulations for complex **31**, however, already yield the best agreement with pure dipolar interaction. Since the dipolar interactions are represented by a matrix, it cannot be represented by a single value like the exchange parameter J , but the energy difference between the two lowest antiferromagnetic and ferromagnetic exchange states illustrates its magnitude. This difference is for all complex dimers close to $\Delta E = 0.4 \text{ cm}^{-1}$. If an exchange interaction of $J = -0.05 \text{ cm}^{-1}$ is included, ΔE increases to $\approx 1 \text{ cm}^{-1}$. Calculations for **28** showed the largest overestimation of the thermal relaxation barrier, that is likely to be caused by exchange interactions according to the largest estimated value of $J = -0.1 \text{ cm}^{-1}$ of the Dy(III) complexes.

6. Multiconfigurational Calculations on Lanthanide(III) SMMs

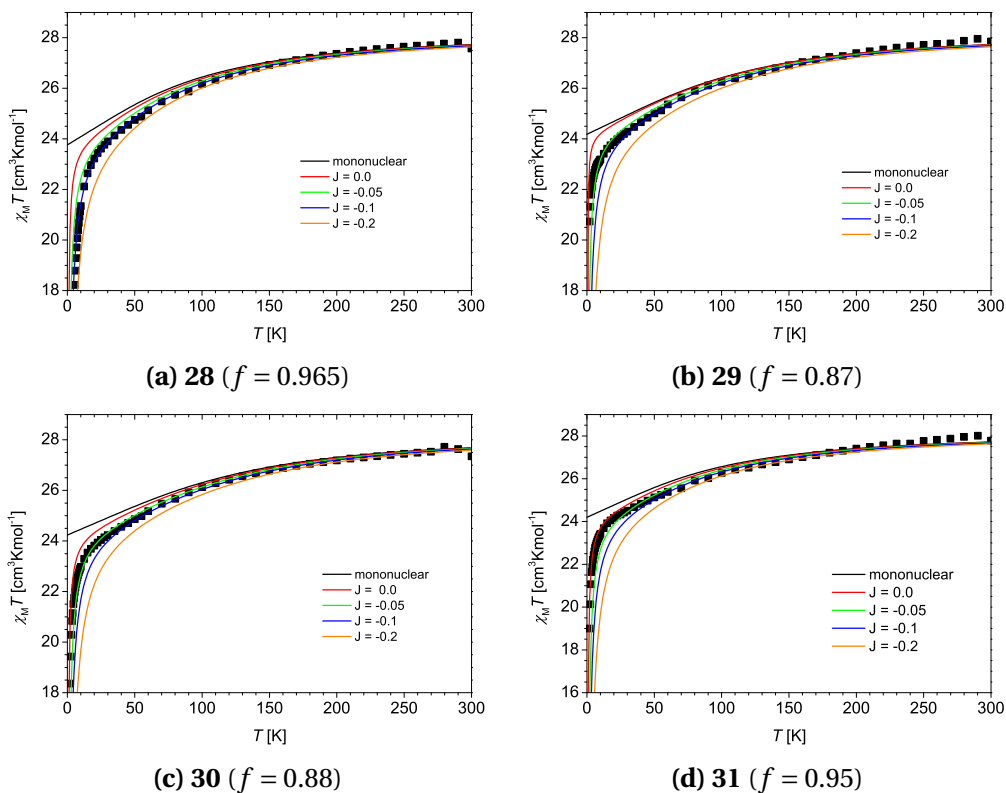


Figure 6.9.: Measured and calculated values for the complexes containing hydrogen-bonded dimers. The black squares represent the measured data scaled by the factor f , the lines are simulated values using the RASSI spin-orbit functions considering exact dipolar interaction as well as an exchange parameter J of given magnitude [cm^{-1}].

BROKEN-SYMMETRY DFT CALCULATIONS ON OLIGONUCLEAR TRANSITION METAL COMPLEXES

7.1. Exchange Coupling in Cu_4O_4 Cubanes with Sugar-Ligands

In coordination chemistry, chiral ligands may serve a large variety of purposes. In catalytic processes, for instance, chiral ligands may promote an enantiomeric excess if a prochiral educt is employed. The asymmetric variants of the epoxidation (Sharpless) and hydrogenation (Knowles and Noyori), who were all awarded the Nobel prize in 2001,^[171–173] are among the most well-known examples. Also, the magnetic properties of transition metal complexes might become even more interesting when involving chiral ligands due to magnetochirality.^[174] An obvious synthetic approach for obtaining chiral ligand molecules is to make use of the chiral pool given by nature.

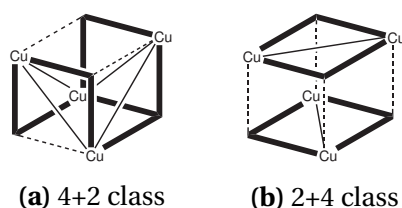


Figure 7.1.: Classification of tetranuclear cubane $\text{Cu}(\text{II})$ complexes according to $\text{Cu}-\text{O}$ and $\text{Cu}\cdots\text{O}$ distances of the Cu_4O_4 core. Thick lines represent short and broken lines long $\text{Cu}-\text{O}$ distances. Short $\text{Cu}\cdots\text{Cu}$ distances are indicated by a connecting line.

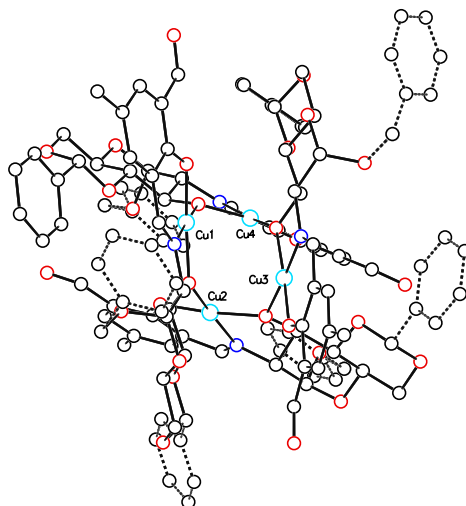


Figure 7.2.: Molecular structure of **35**. Hydrogen atoms were omitted for the sake of clarity.

Hence, during the work of Burkhardt,^[56] the monomer of chitosan (2-amino-2-deoxy-glucose) and derivatives thereof were employed to prepare chiral ligands. The Cu_4O_4 cubane core is a commonly found structural motif for complexes of these ligands. The complexes from the thesis of Burkhardt exhibiting this substructure are listed in Table 7.1. Depending on the number of short and long $\text{Cu}\cdots\text{Cu}$ distances, the Cu_4O_4 cubanes are divided into two main classes, namely the 4+2 class (Fig. 7.1a) and the 2+4 class (Fig. 7.1b).

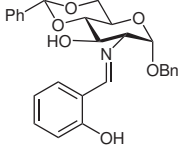
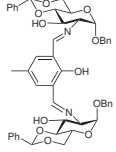
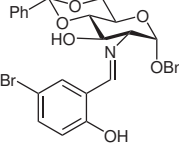
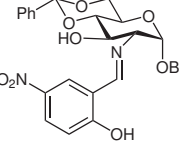
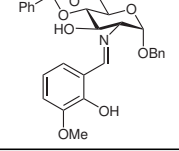
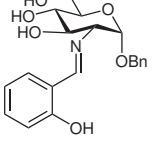
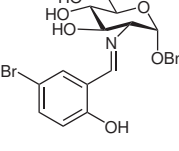
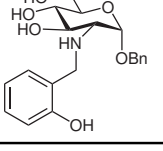
For Schiff bases of benzyl 2-amino-4,6-*O*-benzylidene-2-deoxy- α -D-glucopyranose with salicylic aldehyde derivatives, 4+2 class cubanes were obtained. Representative for these compounds, the structure of **35** is depicted in Fig. 7.2. Within their structure, the Cu(II) ions are embedded in a square-planar environment with a $[\text{NO}_3]$ donor set. Neighboring metal ions share one coordinating oxygen atom with $\text{Cu}-\text{O}-\text{Cu}$ bridging angles of $> 120^\circ$, causing antiferromagnetic exchange interactions.

Ligands derived from benzyl 2-amino-2-deoxy- α -D-glucopyranose, on the other side, form 2+4 cubanes. The molecular structure of **39** is shown in Fig. 7.3 with **40** and **41** structural closely related. The 2+4 cubanes involve square-pyridal coordination of the Cu(II) ions, with two pairs of metal ions sharing the xy -plane*, that contains the magnetic orbital of the d^9 metal ions. Thus, the magnetic behavior of 2+4 cubanes is mainly governed by the interaction within these Cu(II) pairs. Especially **41** might be magnetically very interesting, since, according to Crawford,^[177] the two Cu_2O_2 pairs

*The xy -plane is the mean plane defined by the atoms of the basal $[\text{NO}_3]$ donor set and the Cu atom itself.

7.1. Exchange Coupling in Cu_4O_4 Cubanes with Sugar-Ligands

Table 7.1.: Investigated Cu_4O_4 cubane complexes.

Complex	Ligand	Reference	J_{exp} [cm^{-1}]	
4+2 cubanes	34		[175]	-130
	35		[56]	-183
	36		[56]	-167
	37		[56]	-147
	38		[56]	-207
2+4 cubanes	39		[176]	+64, +4
	40		[56]	-
	41		[56]	-

7. BS-DFT Calculations on Oligonuclear Transition Metal Complexes

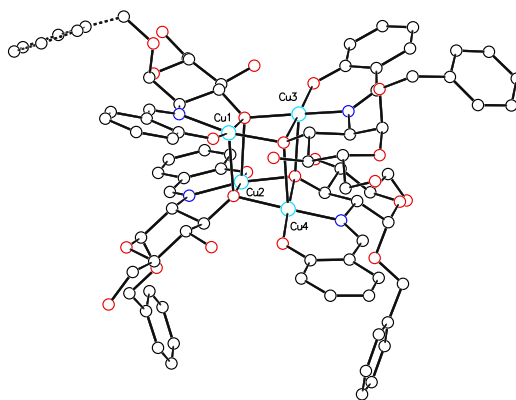


Figure 7.3.: Molecular structure of **39**. Hydrogen atoms were omitted for the sake of clarity.

exhibit bond angles below ($\approx 91.2^\circ$) and above ($\approx 98.5^\circ$) the boundary angle of 97.5° , where the sign of the exchange interaction is expected to switch. Unfortunately, not all of these complexes were fully characterized.

Nevertheless, BS-DFT calculations offer the possibility to explore the magnetic behavior. Different approaches for the prediction of the particular coupling constant of Cu_4O_4 cubanes have been described.^[178] Here, only the substitution of two Cu(II) ions with paramagnetic Zn(II) was employed, giving access to all pairwise Cu–Cu exchange interactions with the six possible substitution patterns. This way, the exchange interaction is directly accessible *via* Eq. (2.43).

The numeration scheme of the Cu(II) ions was chosen with respect to Fig. 7.2 for the 4+2 cubanes and with respect to Fig. 7.3 for the 2+4 cubanes. This is in accordance with the numeration scheme used by Burkhardt.^[56] Small deviations of the structural parameters from the values given there are due to the measurement of the parameters in the xyz-files generated from the crystallographic data. The xyz-files lack thermal displacement parameters, that have an influence on the calculated mean value of structural parameters, if crystallographic data are used.

7.1.1. 4 + 2 Cubanes

As stated by Burkhardt in Ref. [56], the magnetic behavior of the 4+2 cubanes was entirely interpreted employing the Hamiltonian shown in Eq. (7.1).

$$\hat{H} = -J(\hat{S}_1\hat{S}_2 + \hat{S}_2\hat{S}_3 + \hat{S}_3\hat{S}_4 + \hat{S}_1\hat{S}_4) \quad (7.1)$$

As mentioned above, complexes **34-38** show moderate antiferromagnetic exchange interactions between -130 and -207 cm^{-1} (see Table 7.1). [56,175] The results from the BS-DFT calculations for the pairwise coupling constants are listed in Table 7.2 together with the angle $\angle(\text{Cu} - \text{O} - \text{Cu})$ and the angle between the xy -planes of the Cu(II) ions $\angle(\text{Cu}_{xy} - \text{Cu}_{xy})$. Obviously, the magnetic interactions between Cu(II) ions without a bridging oxygen atom ($J_{1,3}$ and $J_{2,4}$) are small ($|J| < 10 \text{ cm}^{-1}$) and preferably antiferromagnetic. The magnitude of the exchange interaction between oxo-bridged Cu(II) ions is found between -26 and -183 cm^{-1} . Furthermore, it is easily seen, that for all complexes except **35**, $J_{2,3}$ and $J_{1,4}$ show significantly stronger antiferromagnetic coupling than $J_{1,2}$ and $J_{3,4}$. From two-dimensional scatter plots of J vs $\angle(\text{Cu} - \text{O} - \text{Cu})$ (Fig. 7.4, left) and J vs $\angle(\text{Cu}_{xy} - \text{Cu}_{xy})$ (Fig. 7.4, right), no clear correlations are found. While for **34**, **36**, **37**, and **38**, larger values of $\angle(\text{Cu}_{xy} - \text{Cu}_{xy})$ correlate with a more positive J , **35** shows a the decreasing J with increasing $\angle(\text{Cu}_{xy} - \text{Cu}_{xy})$. The J vs $\angle(\text{Cu} - \text{O} - \text{Cu})$ plot for **35**, however, is distributed linearly, whereas the other 4+2 cubanes exhibit no connection of these values. It is worth noting, that **35** is the only complex with $\angle(\text{Cu} - \text{O} - \text{Cu}) > 130^\circ$ for two Cu(II) pairs. The contour plot of J in dependence of $\angle(\text{Cu} - \text{O} - \text{Cu})$ and $\angle(\text{Cu}_{xy} - \text{Cu}_{xy})$ shown in Fig. 7.5, however, is able to predict a general trend of an increasing antiferromagnetic $|J|$ for increasing $\angle(\text{Cu} - \text{O} - \text{Cu})$ and decreasing $\angle(\text{Cu}_{xy} - \text{Cu}_{xy})$. Nevertheless, the data set is too small to deduce a quantitative expression.

Comparing the DFT results with the experimental data turns out to be ambiguous, since higher symmetry than really present in the structure was assumed for the Hamiltonian in the least-squares fits. Hence, the average of the four exchange parameters $J_{1,2}$, $J_{2,3}$, $J_{3,4}$, and $J_{1,4}$ listed in Table 7.2 are used for comparison. For the complexes **34**, **35**, and **37**, theoretical results are in good agreement with experiment, whereas for **36** and **38**, J is underestimated by up to 50%. Furthermore, the theoretical results for the exchange interactions for all 4+2 cubanes were used for simulations of the thermal dependence of χ_M and $\chi_M T$. Therefore, the full spin Hamiltonian from Eq. (7.2) was employed, regarding all calculated J -values.

7. BS-DFT Calculations on Oligonuclear Transition Metal Complexes

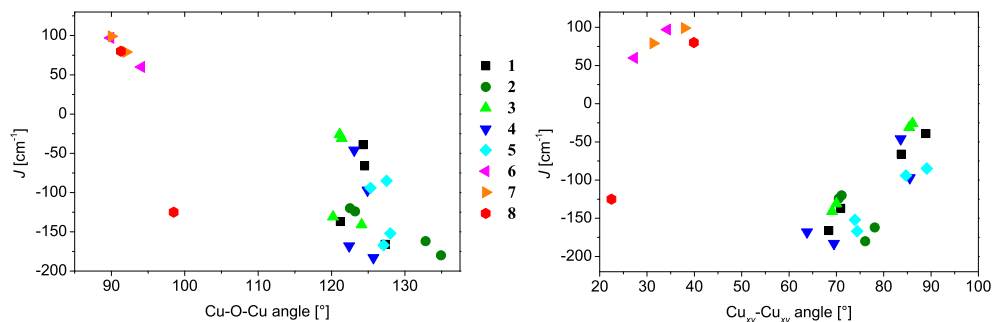


Figure 7.4.: Plots of the calculated exchange interactions J between the Cu–Cu pairs with short distances in dependence of the Cu–O–Cu angle (left) and of the angle between the Cu_{xy} -planes.

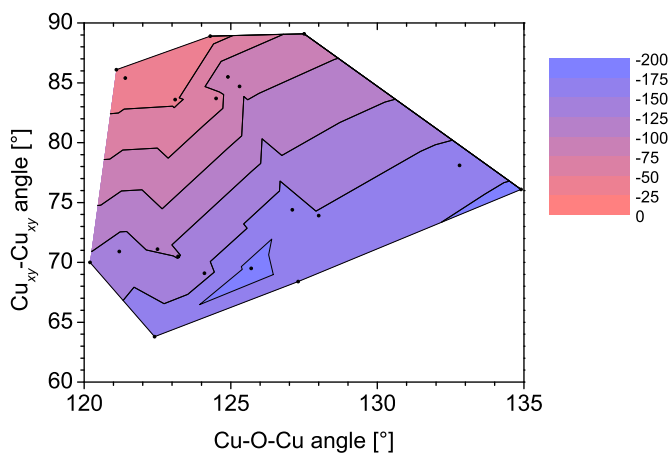


Figure 7.5.: Contour plot of J_{calc} both with respect to $\angle(\text{Cu} - \text{O} - \text{Cu})$ and $\angle(\text{Cu}_{xy} - \text{Cu}_{xy})$ for the 4+2 cubanes. The dots represent the used data points to extrapolate the contours.

7.1. Exchange Coupling in Cu_4O_4 Cubanes with Sugar-Ligands

Table 7.2.: Bond angles, angles between the Cu_{xy} -planes and calculated coupling constants of Cu(II) ions for the 4+2 cubanes.

Complex	$J_{i,j}$	$\angle(\text{Cu}_i - \text{O} - \text{Cu}_j)$ [°]	$\angle(\text{Cu}_{xy,i} - \text{Cu}_{xy,j})$ [°]	J_{calc} [cm^{-1}]	$J_{\text{av.}}^a$ [cm^{-1}]
34	$J_{1,2}$	124.5	83.7	-66	-102
	$J_{2,3}$	127.3	68.4	-166	
	$J_{3,4}$	124.3	88.9	-39	
	$J_{1,4}$	121.2	70.9	-137	
	$J_{1,3}$	–	45.7	-5	
	$J_{2,4}$	–	43.0	1	
35	$J_{1,2}$	132.8	78.1	-162	-146
	$J_{2,3}$	123.2	70.5	-124	
	$J_{3,4}$	134.9	76.1	-180	
	$J_{1,4}$	122.5	71.1	-120	
	$J_{1,3}$	–	27.0	-4	
	$J_{2,4}$	–	26.4	-9	
36	$J_{1,2}$	121.4	85.4	-31	-82
	$J_{2,3}$	124.1	69.1	-141	
	$J_{3,4}$	121.1	86.1	-26	
	$J_{1,4}$	120.2	70.0	-131	
	$J_{1,3}$	–	45.8	-4	
	$J_{2,4}$	–	41.4	1	
37	$J_{1,2}$	123.1	83.6	-46	-123
	$J_{2,3}$	122.4	63.8	-168	
	$J_{3,4}$	124.9	85.5	-97	
	$J_{1,4}$	125.7	69.5	-183	
	$J_{1,3}$	–	46.3	-5	
	$J_{2,4}$	–	44.9	1	
38	$J_{1,2}$	125.3	84.7	-94	-125
	$J_{2,3}$	128.0	73.9	-152	
	$J_{3,4}$	127.5	89.1	-85	
	$J_{1,4}$	127.1	74.4	-167	
	$J_{1,3}$	–	45.0	-8	
	$J_{2,4}$	–	35.9	0	

^a $J_{\text{av.}}$ is the average of $J_{1,2}$, $J_{2,3}$, $J_{3,4}$, and $J_{1,4}$.

7. BS-DFT Calculations on Oligonuclear Transition Metal Complexes

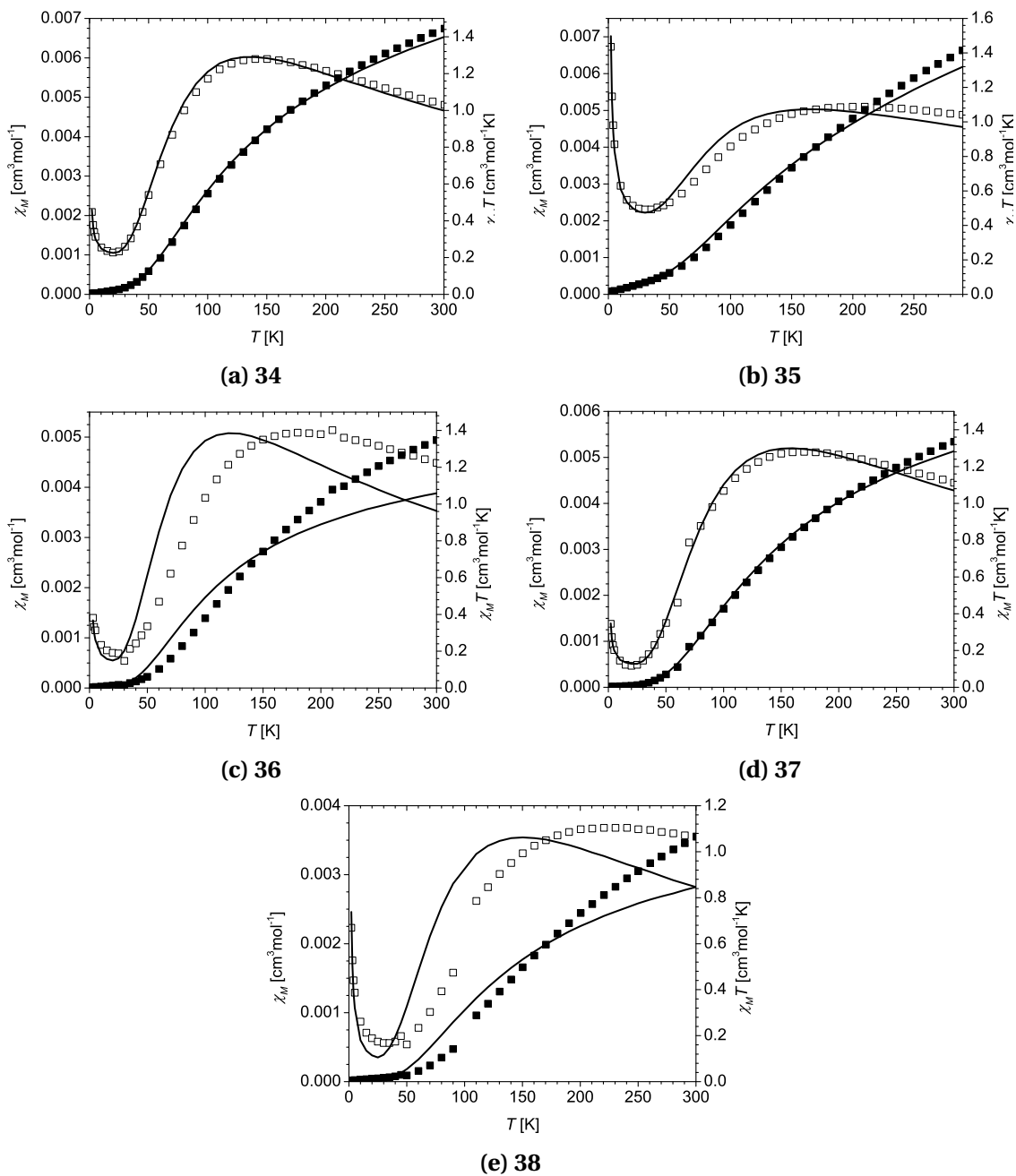


Figure 7.6.: χ_M vs T (empty squares) and $\chi_M T$ vs T plots (black squares) values for the 4+2 cubane complexes. The lines are simulations with the calculated values listed in Tables 7.2 and 7.3.

Table 7.3.: g , χ_{TIP} , and ρ for complexes **34-38** used for the plots of the χ_M and $\chi_M T$ with the theoretical J -values.

Complex	g	$\chi_{\text{TIP}} [\text{cm}^3\text{mol}^{-1}]$	ρ [%]
34	2.01	$9.2 \cdot 10^{-4}$	0.66
35	1.82	$1.9 \cdot 10^{-3}$	2.78
36	1.78	$3.9 \cdot 10^{-4}$	0.76
37	2.11	$4.1 \cdot 10^{-4}$	0.52
38	1.76	$1.4 \cdot 10^{-4}$	1.24

$$\hat{H} = -J_{1,2}\hat{S}_1\hat{S}_2 - J_{1,3}\hat{S}_1\hat{S}_3 - J_{1,4}\hat{S}_1\hat{S}_4 - J_{2,3}\hat{S}_2\hat{S}_3 - J_{2,4}\hat{S}_2\hat{S}_4 - J_{3,4}\hat{S}_3\hat{S}_4 \quad (7.2)$$

The remaining parameters g , χ_{TIP} , and ρ necessary for meaningful susceptibility simulations were obtained by least-squares fits with fixed J s. Obtained values are listed in Table 7.3. Only the fitted g -values for **34** and **37** are larger than 2.0, while this is not the case for the complexes **35**, **36**, and **38**. χ_{TIP} and ρ exhibit reasonable magnitudes. Plots of the experimental and simulated data for complexes **34-38** are depicted in Fig. 7.6. The simulations for **34** (Fig. 7.6a) and **37** (Fig. 7.6d) reproduce remarkably well the experimental χ_M vs T plots. While **35** still shows a good agreement of simulation and experiment, significant deviations are found for **36** and **38**. The maximum of the χ_M vs T plot for the two latter compounds is shifted to lower temperatures compared to experiment, confirming the underestimation of the calculated J -values. The g -values below 2.0 are then just a consequence of the least-squares fit.

7.1.2. 2 + 4 Cubanes

The 2+4 cubanes show a general structural difference compared to the 4+2 cubanes, since the Cu(II) ions share two μ_2 -O-bridges. Hence, two Cu–O–Cu bond angles are listed in Table 7.4 with the results from BS-DFT. $\angle(\text{Cu}_{xy} - \text{Cu}_{xy})$ is in general below the values found for the 4+2 cubanes. Calculated exchange interactions mediated by axial coordination of oxygen atoms ($J_{1,2}$, $J_{2,3}$, $J_{3,4}$, and $J_{1,4}$) are throughout found between 3 and 10 cm^{-1} due to the small spatial overlap of the magnetic orbitals. Complexes **39** and **40** exclusively show Cu–O–Cu bond angles of $< 95^\circ$, giving rise to ferromagnetic interactions. The average of $J_{1,3}$ and $J_{2,4}$ is $J_{\text{av.}} = 78 \text{ cm}^{-1}$ for **39**, which is in good

7. BS-DFT Calculations on Oligonuclear Transition Metal Complexes

Table 7.4.: Bond angles, dihedral angles and calculated coupling constants of Cu(II) ions in 2+4 cubanes.

Complex	$J_{i,j}$	$\angle(\text{Cu}_i - \text{O} - \text{Cu}_j)$ [°]	$\angle(\text{Cu}_{xy,i} - \text{Cu}_{xy,j})$ [°]	J_{calc} [cm ⁻¹]
39	$J_{1,3}$	93.9	94.3	29.5
	$J_{2,4}$	89.7	90.1	35.6
	$J_{1,2}$	99.4	97.0	24.1
	$J_{2,3}$	104.1	101.8	19.5
	$J_{3,4}$	99.8	96.6	25.4
	$J_{1,4}$	104.5	99.7	22.4
40	$J_{1,3}$	92.8	91.2	32.5
	$J_{2,4}$	89.7	90.1	39.5
	$J_{1,2}$	98.7	97.5	28.4
	$J_{2,3}$	103.7	103.1	18.6
	$J_{3,4}$	95.2	100.3	29.9
	$J_{1,4}$	102.1	106.8	25.5
41	$J_{1,3}$	98.3	98.7	22.5
	$J_{2,4}$	91.3	91.2	39.9
	$J_{1,2}$	91.8	102.5	26.6
	$J_{2,3}$	105.7	97.1	21.7
	$J_{3,4}$	94.7	98.2	24.5
	$J_{1,4}$	102.5	99.4	17.9

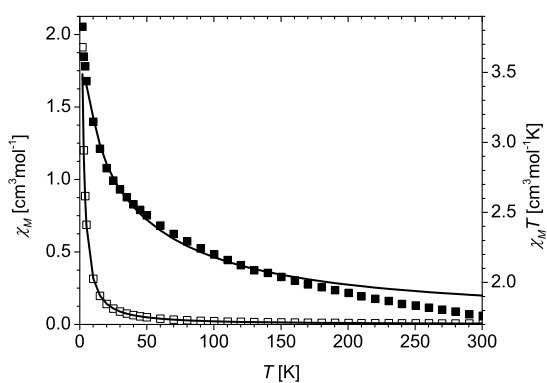


Figure 7.7.: Plots of χ_M vs. T (empty boxes) and $\chi_M T$ vs. T (black squares) of **39**. The solid lines are simulations using the theoretical J -values and g -value obtained from a least-squares fit.

7.2. Hexanuclear Copper(II) Metallocrown with Hydronium Guests

agreement with the experimental value of $J_1 = 64 \text{ cm}^{-1}$, obtained from a least-squares fit utilizing the Hamiltonian:

$$\hat{H} = -J_1 (\hat{S}_1 \hat{S}_3 + \hat{S}_2 \hat{S}_4) - J_2 (\hat{S}_1 + \hat{S}_3) (\hat{S}_2 + \hat{S}_4). \quad (7.3)$$

A least-squares fit with the fixed theoretical J -values afforded $g = 2.15$, which is close to the experimental value of 2.23, while χ_{TIP} and ρ were neglected. The χ_M vs T and $\chi_M T$ vs T simulations depicted in Fig. 7.7 also show a very good agreement with experiment. Unfortunately, reliable susceptibility data for **40** and **41** was not available, and, hence, no comparison of the calculated values is given. BS-DFT results for **40** suggest a similar ferromagnetic behavior as already found for **39**, but with a slightly larger $J_{1,3}$, correlating with a smaller $\angle(\text{Cu} - \text{O} - \text{Cu})$. A completely different picture was found for **41**, where the two strongly interacting Cu(II) pairs exhibit a large difference between the bond angles (91.3 and 91.2° for Cu_1Cu_2 , 98.3 and 98.7° for Cu_3Cu_4), giving rise to different signs of the exchange parameters.^[177] The calculated values of $J_{1,3} = -125 \text{ cm}^{-1}$ and $J_{2,4} = 80 \text{ cm}^{-1}$ confirm the predictions.

While the J vs $\angle(\text{Cu}_{xy} - \text{Cu}_{xy})$ plot shown in Fig. 7.4 (right) does not reveal a clear correlation, the J vs $\angle(\text{Cu} - \text{O} - \text{Cu})$ plot suggests a roughly linear relation. Linear regression of the values for the 2+4 cubanes yields the function $J(x) = -24.8x + 2341$ with a rather low correlation coefficient of $R^2 = 0.892$. Including all values shown in Fig. 7.4 affords an even worse correlation of $R^2 = 0.696$. It should be noted, that not only are there different bridging modes ($\mu_2\text{-O}$ for 4+2 cubanes, $\mu_2\text{-(O)}_2$ for 2+4 cubanes), but also does $\angle(\text{Cu}_{xy} - \text{Cu}_{xy})$ vary over a wide range. Hence, due to a sum of structural parameters changing for the Cu_2 pairs, the small data pool forbids quantization of the magnetostructural correlation. But, nonetheless, the partially excellent agreement between theory and experiment, in particular found for **34**, **37**, and **39**, suggests, that the obtained values for **40** and **41** draw generally the right picture of the magnetic behavior.

7.2. Hexanuclear Copper(II) Metallocrown with Hydronium Guests

Since the first metallocrown complex was reported in 1989 by Lah and Pecoraro,^[179] this class of compounds has grown into a vivid research area.^[180] While the early def-

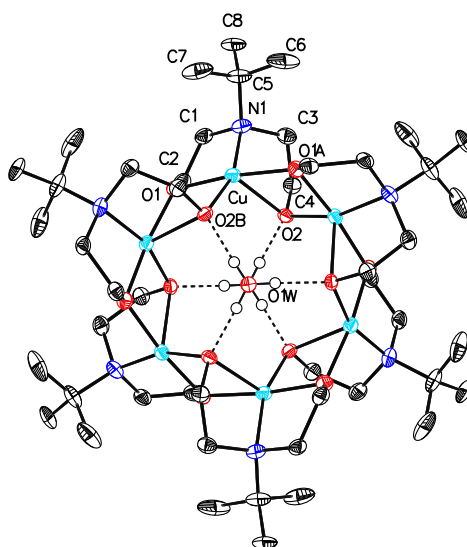


Figure 7.8.: Molecular structure of the complex cation $[(\text{H}_3\text{O})_2\text{Cu}_6(\text{tbdea})_6]^{2+}$ of compound **42**, viewing along the [111] axis of the crystal. Aliphatic hydrogen atoms are omitted for clarity. The thermal ellipsoids are drawn at a probability level of 50%.

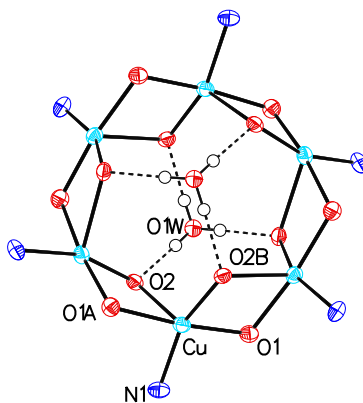


Figure 7.9.: Non-carbon atoms of the complex cation $[(\text{H}_3\text{O})_2\text{Cu}_6(\text{tbdea})_6]^{2+}$ with a view angle slightly twisted to the [111] axis .

7.2. Hexanuclear Copper(II) Metallacrown with Hydronium Guests

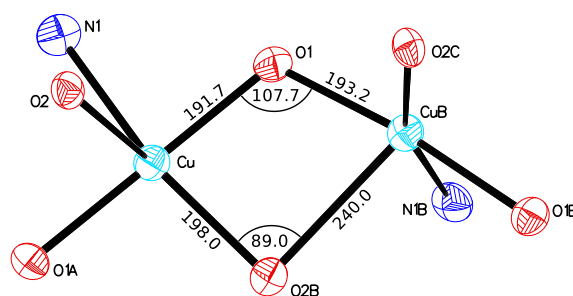


Figure 7.10.: Coordination environment of two neighboring Cu(II) ions in **42** with the bond lengths [pm] and angles [°] of the two μ_2 -O-bridges.

inition of metallacoronates only incorporated a $-\text{[M-N-O]}_n-$ repeating unit, later definitions also included for example $-\text{[M-N-C-O]}_n-$, $-\text{[M-N-N]}_n-$, or, even more general, $-\text{[M-X]}_n-$ repeating units (where X is a nonmetal atom) in a cyclic arrangement. Within the PhD thesis of Zharkuskaya, the hexanuclear copper coronate $[\text{NHEt}_3][(\text{H}_3\text{O})_2\text{Cu}_6(\text{tbdea})_6](\text{ClO}_4)_3$ (**42**) was prepared employing *N-tert*-butyl diethanolamine and copper(II) perchlorate in acetonitrile under the addition of triethylamine.

The molecular structure of the complex cation $[(\text{H}_3\text{O})_2\text{Cu}_6(\text{tbdea})_6]^{2+}$ is depicted in Fig. 7.8. In Fig. 7.9, the non-carbon backbone of **42** is depicted with a slightly different viewing angle. The metallacrown complex exhibits a cyclic $-\text{[Cu-O]}_6-$ substructure, and, therefore, may be counted to the 12-MC-6 class. It is not uncommon for metallacoronates to contain guest ions (easily seen from the tables in^[180]), but to our knowledge, H_3O^+ ions in such a cavity were not yet reported. In the closely related octanuclear complex $[\text{Cu}_8(\text{tbdea})_6(\text{H}_2\text{O})_2](\text{BF}_4)_2 \cdot 3 \text{CH}_3\text{OH}$ (**43**),^[181] where the same ligand was employed, six Cu(II) ions are assembled in a similar fashion as in **42**, but with a two μ_2 -O-bridged Cu(II) ions found in the cavity. In complex **42**, each Cu(II) ion is coordinated by a $[\text{NO}_4]$ donor set in a distorted square-pyramidal coordination environment. Important bond lengths and angles are listed in Table 7.5. The basal plane is formed by the atoms N1, O1, O2B, and O1A with bond lengths between 191 and 210 pm. O2 is coordinated in the apical position with an elongated bond length of 240 pm, as expected due to the Jahn-Teller distortion. CShMs calculated for trigonal-bipyramidal (D_{3h}) and square-pyramidal coordination (C_{4v}) suggest a closer relation to the first ($S_{C_{3h}} = 3.91$) than the latter symmetry ($S_{C_{4v}} = 6.13$). Neighboring Cu(II) ions share two μ_2 -bridging oxygen atoms (O1 and O2), with O1 being part of both ions basal plane, while O2 is found in the apical position of one Cu(II) ions (see Fig. 7.10).

7. BS-DFT Calculations on Oligonuclear Transition Metal Complexes

Table 7.5.: Selected bond lengths [pm] and angles [°] of **42**.

Cu–O1	191.7(4)	Cu–O1A	193.2(4)
Cu–O2	240.0(4)	Cu–O2B	198.0(4)
Cu–N1	210.4(5)		
O1–Cu–O1A	172.98(19)	O1–Cu–O2	100.68(15)
O1–Cu–O2B	84.13(16)	O1–Cu–N1	84.82(18)
O1A–Cu–O2	73.25(14)	O1A–Cu–O2B	95.24(16)
O1A–Cu–N1	97.37(18)	O2–Cu–O2B	115.62(19)
O2–Cu–N1	80.01(16)	O2B–Cu–N1	162.33(18)
Cu–O1–CuB	107.72(18)	Cu–O2–CuA	89.87(14)

Atoms with the suffixes A and B were generated by the following symmetry operations:

A: $-z, -x + 1, -y + 1$

B: $-y + 1, -z + 1, -x$.

For the magnetic interaction between direct neighbors, the bridging angles $\angle(\text{Cu–O1–CuB}) = 107.7^\circ$ and $\angle(\text{Cu–O2B–CuB}) = 89.9^\circ$ might be of crucial importance. Due to the high symmetry of the complex **42**, interesting magnetic properties like frustration phenomena^[182] might be found, given certain requirements concerning the exchange interactions are met. Here, at first, the experimental susceptibility data of **42** is reinvestigated utilizing different spin Hamiltonians including more than one exchange parameters. Furthermore, BS-DFT calculations were performed to verify the interpretations of the magnetic measurements.

7.2.1. Magnetic Properties

The interpretation of the susceptibility data of **42** was performed by Zharkuskaya^[38] employing only a single exchange interaction parameter and the Weiss temperature θ for modeling an intermolecular interaction. Due to the maximum visible in the χ_M vs T plot depicted in Fig. 7.12, dominating antiferromagnetic exchange interaction is assumed. While θ is only a correction term and $\theta \ll J$ should apply, the value $\theta = -117\text{K}$ ($\hat{=} -81\text{cm}^{-1}$) tremendously exceeds the magnitude of the coupling constant $J = -15.5\text{cm}^{-1}$. Hence, the meaning of this fit remains questionable.

The magnetic properties of **42** were reinvestigated employing different Hamiltonians, namely the $1J$ -model shown in Eq. (7.4), the $2J$ -model in Eq. (7.5), and the $3J$ -

7.2. Hexanuclear Copper(II) Metallacrown with Hydronium Guests

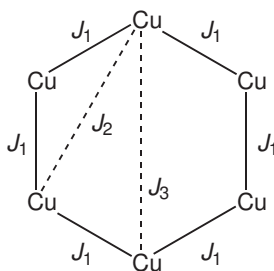


Figure 7.11.: Exchange interactions considered for the simulations of the magnetic properties. For J_2 and J_3 , lines for the symmetrically equivalent interactions were omitted.

model in Eq. (7.6).

$$\hat{H} = g\mu_B \mathbf{H} \sum_i^6 \hat{S}_i - J_1 \left(\sum_{i=1}^5 \hat{S}_i \hat{S}_{i+1} + \hat{S}_1 \hat{S}_6 \right) \quad (7.4)$$

$$\hat{H} = g\mu_B \mathbf{H} \sum_i^6 \hat{S}_i - J_1 \left(\sum_{i=1}^5 \hat{S}_i \hat{S}_{i+1} + \hat{S}_1 \hat{S}_6 \right) - J_2 \left(\sum_{i=1}^4 \hat{S}_i \hat{S}_{i+2} + \hat{S}_1 \hat{S}_5 + \hat{S}_2 \hat{S}_6 \right) \quad (7.5)$$

$$\hat{H} = g\mu_B \mathbf{H} \sum_i^6 \hat{S}_i - J_1 \left(\sum_{i=1}^5 \hat{S}_i \hat{S}_{i+1} + \hat{S}_1 \hat{S}_6 \right) - J_2 \left(\sum_{i=1}^4 \hat{S}_i \hat{S}_{i+2} + \hat{S}_1 \hat{S}_5 + \hat{S}_2 \hat{S}_6 \right) - J_3 \sum_{i=1}^3 \hat{S}_i \hat{S}_{i+3} \quad (7.6)$$

A graphical representation of the exchange interactions J_1 , J_2 , and J_3 is shown in Fig. 7.11. Unfortunately, least-squares fits of these spin Hamiltonians to the experimental χ_M values led to g -values of ≈ 1.50 , which is far too low for Cu(II) ions. Therefore, the parameters were chosen manually to reproduce best the shape of the experimental χ_M vs T plots (e.g. position and height of the maximum). In addition, a paramagnetic impurity ρ modeling a single $S = \frac{1}{2}$ ion and temperature independent paramagnetism χ_{TIP} were introduced. The magnitudes of both parameters were estimated from the low-temperature region, where the χ_M values increase upon cooling below 4.5 K, leading to $\chi_{\text{TIP}} = 0.0011 \text{ cm}^3 \text{ mol}^{-1}$ and $\rho = 0.03$. The parameters obtained from simulations with the three models are listed in Table 7.6. Experimental χ_M data of **42** together with the simulated values are depicted in Fig. 7.12. The obtained g -values lie in the typical range for Cu(II) ions, while the exchange interaction J_1 between nearest neighbors is antiferromagnetic and of intermediate size (-50 cm^{-1} for 1 J -model, $\approx -70 \text{ cm}^{-1}$ for 2 J - and 3 J -model). This is also in good agreement with the correlations found by Ruiz *et al.*,^[178] predicting antiferromagnetic exchange for

7. BS-DFT Calculations on Oligonuclear Transition Metal Complexes

Table 7.6.: Parameters and sums of square of errors χ^2 for the simulation of the χ_M data of **42** with the different model Hamiltonians.

model	1J Eq. (7.4)	2J Eq. (7.5)	3J Eq. (7.6)	1J-MFT Eq. (7.4) + MFT
g	2.02	2.05	2.02	2.05
J_1 [cm^{-1}]	-50	-70	-72	-44
J_2 [cm^{-1}]	-	-30	-25	-
J_3 [cm^{-1}]	-	-	3	-
λ [cm^{-3}mol]	-	-	-	-33
χ_{TIP} [$\text{cm}^3\text{mol}^{-1}$]	0.0011	0.0011	0.0011	0.0018
ρ	0.03	0.03	0.03	0.02
χ^2	$2.89 \cdot 10^{-4}$	$6.68 \cdot 10^{-5}$	$9.87 \cdot 10^{-5}$	$3.94 \cdot 10^{-6}$

$\angle(\text{Cu}-\text{O}-\text{Cu}) > 89.5^\circ$. Thus, the 1J-model is not sufficient to describe the magnetic interactions encountered in **42**. For complex **43**, a positive J was found for the interaction between the Cu(II) ions in the hexanuclear ring, probably owed to the smaller Cu–O–Cu bond angles (104.1° and 85.9°). χ_M -fits for **42** with the 2J- or 3J-model afford J_2 -values of -30 and -25 cm^{-1} , respectively. J_3 only shows a small value of $+3 \text{ cm}^{-1}$ in the 3J-model between the opposite Cu(II) ions. Judging by the similarity of the χ_M plots, the 2J- and the 3J-model reproduce the shape of the experimental χ_M vs T plot considerably better than the 1J-model. Nevertheless, the introduction of a third exchange interaction J_3 does not yield a significant improvement with experimental χ_M data, and, hence, the 2J-model is assumed to give the best agreement with experiment. However, the exchange interaction between next-to-nearest neighbors (J_2) seems a bit large, particularly because no bridging ligands able to promote superexchange are present.

To overcome the above mentioned drawbacks of the 2J-model, also the modeling of a second exchange interaction by means of molecular field theory (MFT) using the parameter λ is introduced as shown in Eq. (7.7). λ gives an average estimation of the interaction with the eight surrounding complex cations and is defined in 7.8.^[22] Similar to the parameter Θ_p in the Curie-Weiss law given in 1.4, λ causes a parallel shift of the $\chi_M^{-1}(T)$ plot. Already the use of a single intramolecular interaction J_1 (1J-MFT-model) is sufficient to yield a better description of the experimental χ_M values, as seen from the lower χ^2 values in Table 7.6.

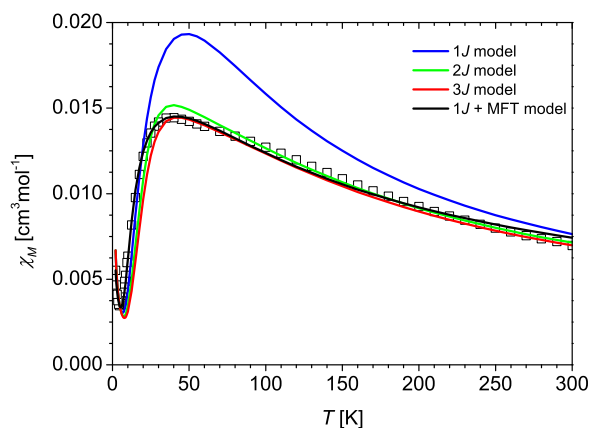


Figure 7.12.: Experimental χ_M values (empty squares) for **42**. The colored lines represent simulations for the $1J$ -, $2J$ -, and $3J$ -model. The parameters used are listed in Table 7.6.

$$\frac{1}{\chi_M} = \frac{1}{\chi_{M,s}} - \lambda \quad (7.7)$$

$$\lambda = \frac{2 \sum z_i J_{\text{ex},i}}{\mu_0 N_A \mu_B^2 g^2} \quad (7.8)$$

From a least-squares fit, $J_1 = -44 \text{ cm}^{-1}$ was obtained, if $\chi_{\text{TIP}} = 0.018 \text{ cm}^3 \text{ mol}^{-1}$ and $\rho = 0.02$ were held constant. With $\lambda = -33 \text{ cm}^{-3} \text{ mol}$, an additional intermolecular anti-ferromagnetic exchange interaction is present. The simulated χ_M vs T plot in Fig. 7.12 matches remarkably well the experimental data and shows an even lower sum of the squares of errors χ^2 . Since each the $2J$ -model as well as the $1J$ -MFT-model give reasonable descriptions of the magnetic properties of **42**, no clear statement which one is closer to reality may be given. To clarify this ambiguity, BS-DFT calculations were performed as described in the following section.

7.2.2. Broken-Symmetry DFT calculations

For the DFT treatment of **42**, only the complex cation $[(\text{H}_3\text{O})_2\text{Cu}_6(\text{tbdea})_6]^{2+}$ as obtained from the crystal structure was considered (referred to as $\text{Cu}_6/\text{H}_3\text{O}^+$). The coordinates of the hydrogen atoms were optimized utilizing the GGA functional BP86. Also, the influence of the hydronium ions on the magnetic behavior was investigated by performing analogue calculations on the metallacrown without the H_3O^+ ions present (referred to as Cu_6). Similar cyclic hexanuclear systems containing Cu(II) and Ni(II) have already been investigated by means of BS-DFT by Ruiz *et al.*^[183] Assuming S_6 symme-

7. BS-DFT Calculations on Oligonuclear Transition Metal Complexes

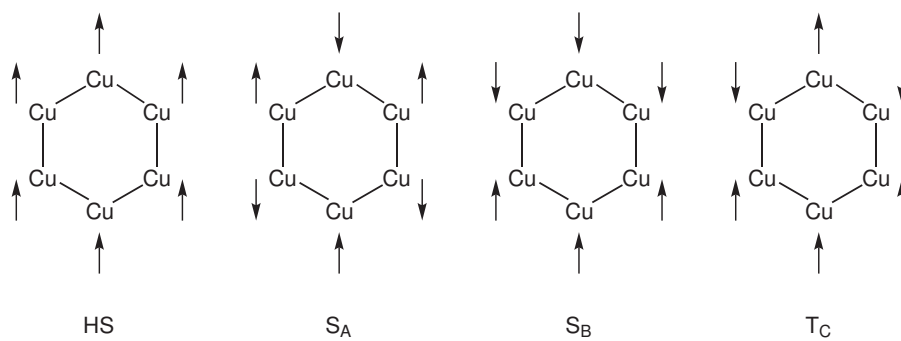


Figure 7.13.: Spin states necessary for the calculation of all exchange interaction parameters of a symmetric hexanuclear cyclic complexes.

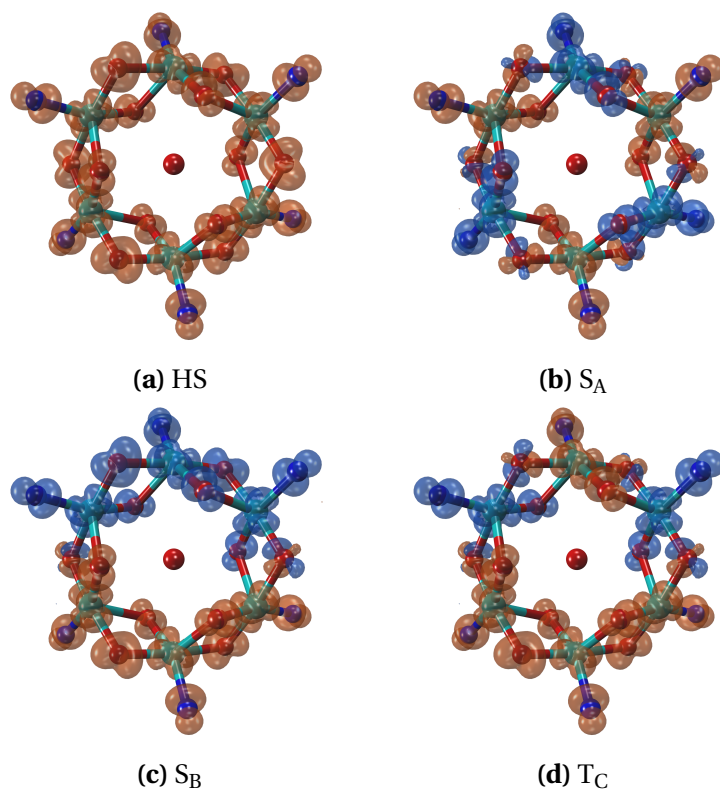


Figure 7.14.: Spin densities of all calculated spin states of Cu₆/H₃O⁺ in the BS-DFT calculations. Isosurfaces were drawn at a spin density of 0.003 e/Å³. α -spin density is depicted orange and β -spin density blue, respectively. Carbon and hydrogen atoms were omitted for clarity.

try, three non-equivalent exchange interactions J_1 , J_2 , and J_3 arise (see Fig. 7.11). To obtain all three coupling constants, the single point energies of the four spin states shown in Fig. 7.13 have to be calculated. Upon neglecting the interaction between opposite metal ions (J_3), Eqs. (7.9a) and (7.9b) arise:

$$J_1 = \frac{E_{SA} - E_{FM}}{6} \quad (7.9a)$$

$$J_2 = \frac{3E_{SB} - 2E_{HS} - E_{SA}}{12} \quad (7.9b)$$

If all three interactions are considered, Eqs. (7.10a) to (7.10c) are obtained.

$$J_1 = \frac{6E_{TC} - 2E_{FM} - E_{SA} - 3E_{SB}}{12} \quad (7.10a)$$

$$J_2 = \frac{3E_{TC} - E_{FM} - 2E_{SA}}{6} \quad (7.10b)$$

$$J_3 = \frac{E_{SA} + E_{SB} - 2E_{TC}}{2} \quad (7.10c)$$

Furthermore, substitution of all but two Cu(II) ions with diamagnetic Zn(II) ions was used to calculate pairwise exchange interactions with Eq. (2.43), similar to the methodology used in Section 7.1.

The convergence of the desired spin states was verified by Mulliken population analysis and isosurface plots of the spin density, which are shown in Fig. 7.14. The single point energies and spin expectation values are listed in Table 7.7 for $\mathbf{Cu}_6/\text{H}_3\text{O}^+$ and Table 7.8 for \mathbf{Cu}_6 , respectively. For the high-spin state, providing the maximal spin multiplicity, the relation $\langle \hat{S}^2 \rangle = S(S+1)$ holds true. The broken-symmetry states show spin contamination due to the mixing of wave functions of different spin multiplicities. For these states, Eq. (7.11) is obeyed.^[63]

$$\langle \hat{S}^2 \rangle_{\text{UHF}} = \langle \hat{S}^2 \rangle_{\text{exact}} + N^\beta - \sum_i^N \sum_j^N |S_{ij}^{\alpha\beta}|^2 \quad (7.11)$$

The spin contamination is owed to the monodeterminantal ansatz of density functional theory. To overcome this problem, a multiconfigurational method like CASSCF would be necessary, but due to the large active space required, this is not performed routinely yet.

Employing either Eq. (7.9) or Eq. (7.10) the calculated value of $J_1 = -63 \text{ cm}^{-1}$ for $\mathbf{Cu}_6/\text{H}_3\text{O}^+$ is obtained. The interaction between next-nearest neighbors J_2 , however,

7. BS-DFT Calculations on Oligonuclear Transition Metal Complexes

Table 7.7.: Energies and spin expectation values $\langle \hat{S}^2 \rangle$ of the high-spin state and the broken-symmetry states for $\mathbf{Cu}_6/\mathbf{H}_3\mathbf{O}^+$.

State	Energy [a.u.]	ΔE [cm^{-1}]	$\langle \hat{S}^2 \rangle$
HS ($S = 3$)	-13117.54943712	380.1	12.01
S _A ($S = 0$)	-13117.55116896	0.0	2.95
S _B ($S = 0$)	-13117.55003279	249.4	2.99
T _C ($S = 1$)	-13117.55060076	124.7	3.97

Table 7.8.: Energies and spin expectation values $\langle \hat{S}^2 \rangle$ of the high-spin state and broken-symmetry states for \mathbf{Cu}_6 .

State	Energy [a.u.]	ΔE [cm^{-1}]	$\langle \hat{S}^2 \rangle$
HS ($S = 3$)	-12963.78384644	323.4	12.02
S _A ($S = 0$)	-12963.78531996	0.0	2.96
S _B ($S = 0$)	-12963.78435012	212.9	3.00
T _C ($S = 1$)	-12963.78483512	106.4	3.98

Table 7.9.: Calculated exchange interactions parameters [cm^{-1}] for $\mathbf{Cu}_6/\mathbf{H}_3\mathbf{O}^+$ and \mathbf{Cu}_6 .

	$\mathbf{Cu}_6/\mathbf{H}_3\mathbf{O}^+$			\mathbf{Cu}_6		
	Eq. (7.9)	Eq. (7.10)	Eq. (2.43) ^a	Eq. (7.9)	Eq. (7.10)	Eq. (2.43) ^a
J_1	-63.3	-63.3	-59.1	-53.9	-53.9	-50.1
J_2	-1.0	-1.0	0.6	-0.9	-0.7	0.8
J_3	-	0.0	0.0	-	0.0	0.0

^aAll but the two Cu(II) ions involved in the interaction were replaced by Zn(II) ions.

7.2. Hexanuclear Copper(II) Metallocrown with Hydronium Guests

is found to be -1 cm^{-1} , which is several magnitudes smaller. The exchange interaction J_3 calculated with Eq. (7.10) is zero. Calculations on Zn-substituted structures with 2.43 yielded a slightly smaller J_1 of -59 cm^{-1} , whereas the sign of J_2 changes to ferromagnetic interaction (state energies are listed in Appendix D.3). The contradicting sign of J_2 from the different calculations and the very small magnitude indicate, that the boundary of accuracy of the method is reached. J_3 remains zero. In general, the picture does not change drastically for Cu_6 , where the interactions $J_1 = -54 \text{ cm}^{-1}$ and $J_2 = -1 \text{ cm}^{-1}$ are found, while J_3 remains zero. Results for the Zn-substituted species exhibit the same trends as above, predicting $J_1 = -50 \text{ cm}^{-1}$ and a small ferromagnetic J_2 .

A closer look on the spin density distributions of $\text{Cu}_6/\text{H}_3\text{O}^+$ in Fig. 7.14 does not show any spin density at the hydronium ion. Hence, no superexchange pathway involving the guest molecule is proposed. Mulliken population analysis reveals, how the spin density changes upon the loss of the hydronium ion in Cu_6 . While the spin density at the Cu(II) ions does not change upon removing the H_3O^+ ions, the spin density located at the oxygen atoms experiences moderate changes. For the oxygen atoms O1 (atom numbering as depicted in Figs. 7.8 and 7.9 is used), all pointing away from the H_3O^+ ion, the spin density is decreased from $0.171 e$ to $0.159 e$, whereas the bridging oxygens O2, that point towards the center of the metallocrown, is increased from 0.082 to 0.139 . Also, the spin density at the coordinating nitrogen atoms decreases from 0.093 to 0.058 . Thus, the hydrogen bonds between the hydronium ions and O2 decrease the spin density at O1, which lies in the xy -plane of both coordinated Cu(II) ions, and has therefore a larger influence on the Cu–Cu exchange interaction J_1 . The increased spin density at O2 is not similarly decisive for the exchange coupling, since the magnetic orbitals of neighboring do reside in their xy -planes, that intersect at the ligand atom O1.

From the calculated values of the exchange interactions, conclusions for the quality of the aforementioned $2J$ - and $1J$ -MFT-models for the description of the experimental data in Section 7.2.1 can be made. The DFT results, especially for J_2 , are in direct contrast the results from the $2J$ -model. While BS-DFT predicts almost zero exchange coupling, the $2J$ -model demands an interaction of almost half the size of μ_2 -O-bridged neighbors, which is rather counter-intuitive. The $1J$ -MFT-model, however, yields a J_1 of -44 cm^{-1} , which is overestimated in both models $\text{Cu}_6/\text{H}_3\text{O}^+$ and Cu_6 . It is worth noting that the position of the hydrogen atoms of the H_3O^+ guest ion were also optimized in the structure of $\text{Cu}_6/\text{H}_3\text{O}^+$. Furthermore, the very small second intramolecular exchange interaction found from DFT is confirmed with the $1J$ -model including MFT.

Unfortunately, the intermolecular interaction cannot be investigated by similar techniques.

7.3. Ferromagnetic Trinuclear Chromium(III) Complexes

C_3 -symmetric systems of non-integer spin centers are interesting research subjects for chemists and physicists. For the case of antiferromagnetic exchange interaction between the paramagnetic centers, a degenerate $S = \frac{1}{2}$ ground state arises. In contrast, integer-spin centers would lead to an $S = 0$ ground state if antiferromagnetically coupled. For example, the extensively studied triaminoguanidine complex $[\text{Cu}_3(\text{TAG}^{\text{H}})(\text{bipy})_3](\text{ClO}_4)$ (**44**) and its derivatives show a strong antiferromagnetic exchange interaction with $J < -300 \text{ cm}^{-1}$,^[19,38] leading to a large energetic separation of the degenerated ground state. Coherence time measurements revealed outstanding properties of **44** for the application as Qubit. Other non-integer spin ions that might be suitable candidates for potential Qubits include cobalt(II) ($S = \frac{3}{2}$), iron(III) ($S = \frac{5}{2}$), and chromium(III) ($S = \frac{3}{2}$). While the iron(III) complexes exhibit antiferromagnetic coupling of intermediate magnitude,^[38,184] the magnetic behavior of the cobalt(II) complex is hard to interpret due to the strong zero-field splitting intrinsic for high-spin d^7 ions. Hence, no clear value could be assigned for J of the trinuclear cobalt(II) complex.^[38]

For different complexes of the constitution $[\text{Cr}_3(\text{TAG}^{\text{R}})(\text{bipy})_3(\text{Cl})_3]\text{Cl}$ (**45**) however, an increasing $\chi_M T$ value was measured in the low temperature range, indicating ferromagnetic coupling between the Cr(III) ions.^[54] Three different TAG ligand derivatives were used to synthesize C_3 symmetric complexes, but despite numerous crystallization attempts, no crystals of suitable quality for single-crystal diffraction were obtained. The isotope patterns available from mass spectrometry undoubtedly identified $[\text{Cr}_3(\text{TAG}^{\text{R}})(\text{bipy})_3(\text{Cl})_3]^+$ cations.^[54] The results from elemental analysis however, do not give a meaningful result due to the formation of carbides and nitrides. TGA and SQUID magnetometry, however, reasonably confirm the hypothesis of the constitution $[\text{Cr}_3(\text{L})(\text{bipy})_3(\text{Cl})_3]\text{Cl}$ for all complexes.^[54] Least-squares fits of the $\chi_M T$ data with the C_3 symmetric spin-Hamiltonian

$$\hat{H} = \sum_{i=1}^3 g_i \mu_B \hat{S}_i \mathbf{H} - J(\hat{S}_1 \hat{S}_2 + \hat{S}_2 \hat{S}_3 + \hat{S}_1 \hat{S}_3) \quad (7.12)$$

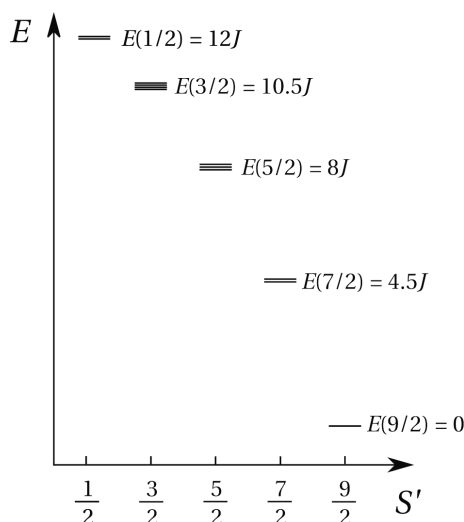


Figure 7.15.: Energy spectrum of a C_3 -symmetric triangular system of $S = \frac{3}{2}$ ions. Assuming a positive sign of J , the energy of the ferromagnetic state was arbitrarily chosen to be zero.

yielded isotropic exchange interaction parameters between $+2.3$ and $+2.6 \text{ cm}^{-1}$ for these complexes. To clear the origin of the ferromagnetic exchange interaction, **45** was investigated with BS-DFT calculations.

7.3.1. Energy Spectrum of $[\text{Cr}_3(\text{TAG}^{\text{R}})(\text{bipy})_3(\text{Cl})_3]\text{Cl}$

For the understanding of the electronic structure of **45**, the energy spectrum of the exchange states is briefly described. For the construction of the energy ladder, the operator $\hat{S}' = \hat{S}_1 + \hat{S}_2 + \hat{S}_3$ is substituted into the exchange part of the Hamiltonian from Eq. (7.12), leading to the Hamiltonian in Eq. (7.13). Eliminating the constant terms \hat{S}_i^2 , the energies of the states described by S' can be calculated by Eq. (7.14). After arbitrarily choosing $E(\frac{9}{2}) = 0$, the distribution of the spin states is illustrated in Fig. 7.15.

$$\hat{H} = -\frac{J}{2} (\hat{S}'^2 - \hat{S}_1^2 - \hat{S}_2^2 - \hat{S}_3^2) \quad (7.13)$$

$$E(S') = -\frac{J}{2} S'(S' + 1) \quad (7.14)$$

The $S' = \frac{1}{2}$ state shows a twofold degeneracy, but lies on the top of the energy spectrum due to the positive sign of J . It is therefore very unlikely to exhibit any properties of a Qubit. The origin of the ferromagnetic interaction within **45** still remains unclear

and thus, BS-DFT calculations were performed to unravel the nature of the magnetic behavior.

7.3.2. Broken-Symmetry DFT Calculations

Due to the lack of a crystal structure for all Cr(III) complexes, the coordinates were generated by the manipulation of the crystal structure of **44**. The structure was then fully optimized using GGA-DFT (RI-BP86, def2-TZVP). Only the complex cation with the unsubstituted ligand TAG^H was investigated since the structural differences found in the solid state are most likely governed by the peripheral substituents. The differences of the crystal packing caused by these packing effects cannot be accounted for in the optimization procedure of a single molecule. The single point energies of **45** calculated using the B3LYP functional and a def2-TZVP basis set are listed in Table 7.10). Both the results for the ferromagnetic state and for the broken-symmetry state were checked for the right spin state of the Cr(III) ions utilizing the Mulliken population analysis.

Assuming the weak interaction limit with the corresponding expression from Eq. (2.43), the formula shown in Eq. (7.15) for the exchange interaction parameter in **45** was deduced. Employing the DFT energies of the high-spin and broken-symmetry states listed in Table 7.10, a value of $J = +3.8 \text{ cm}^{-1}$ is obtained. Considering that no crystal structure of the complexes were available and an optimized structure had to be used, this is in very good agreement with the experimental results.

$$J = \frac{E_{\text{BS}} - E_{\text{HS}}}{12} \quad (7.15)$$

To explain the origin of the ferromagnetic ground state of **45**, the spin densities of the high-spin state and the broken-symmetry state depicted in Fig. 7.16 were inspected. The spin density is mainly located in a cube-shaped space around the Cr(III) ions. This is the expected spatial distribution of electron density for a t_{2g}^3 configuration, where the d_{xy} , d_{xz} , and d_{yz} orbitals are singly occupied. Due to the imine nitrogens of the TAG

Table 7.10.: Single point energies of HS and BS state of **45**.

State	Energy [a.u.]	rel. Energy [cm^{-1}]	$\langle \hat{S}^2 \rangle$
HS ($S = 9/2$)	-7401.1072755083	0.0	24.84
BS ($S = 3/2$)	-7401.1070668901	45.8	6.84

7.3. Ferromagnetic Trinuclear Chromium(III) Complexes

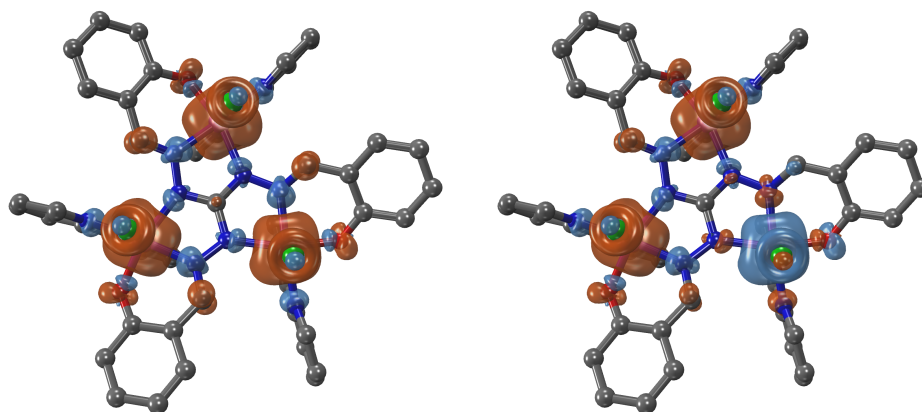


Figure 7.16.: Plots of spin density of the high-spin state (left) and the broken-symmetry state (right) of **45**. Isosurfaces were drawn at $0.003 e/\text{\AA}^3$ with α -spin depicted by orange surfaces and β -spin depicted by blue surfaces.

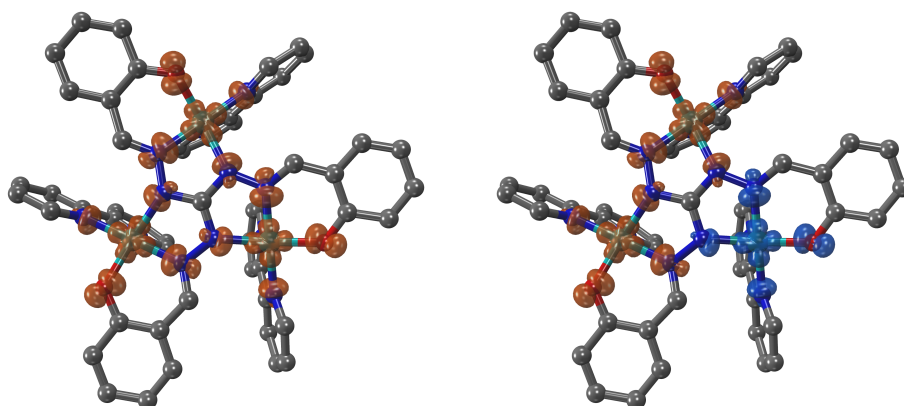


Figure 7.17.: Plots of the spin density for the high-spin state (left) and the broken-symmetry state (right) of **44**. Isosurfaces were drawn at $0.005 e/\text{\AA}^3$ with α -spin depicted by orange surfaces and β -spin depicted by blue surfaces.

7. BS-DFT Calculations on Oligonuclear Transition Metal Complexes

ligand being primarily σ -donors, non-zero spin density is found at the ligand backbone only to a small degree. The t_{2g} symmetry of the singly occupied orbitals at the Cr(III) ions and the lack of the TAG ligands π -donor properties cause a small overlap between the ligand MOs and the d-orbitals. The empty e_g -orbitals are of suitable symmetry, but are found at significantly higher energy. For comparison, also the spin densities for the high-spin and broken-symmetry states of **44** are depicted in Fig. 7.17. There, the $d_{x^2-y^2}$ -orbital is singly occupied, and thus, antiferromagnetic exchange is effectively mediated by the TAG backbone *via* superexchange. Other late transition metals show a similar sign of to exchange interaction as Cu(II) when coordinated with this ligand system. If the TAG ligand is defined as the xy -plane of the Cr(III) in **45**, the d_{xz} - and d_{yz} -orbital show a pronounced mixing with the p_x - and p_y -orbital of the chloro ligand, explaining the ring-like spin distribution in Fig. 7.16 in the apical position. The d_{xy} -orbital shows significant overlap of π -character with the p -orbital of the phenolate oxygen.

Corresponding Orbitals

For a better understanding of the orbital interactions, that lead to ferromagnetic interaction, the diamagnetically substituted structure **Cr₂Zn** was investigated with the corresponding orbital transformation.^[87] The coupling constant calculated directly with Eq. (2.43) from the energy difference of the HS and BS state reproduces the value given above within the computational errors ($J = +4.1 \text{ cm}^{-1}$). The non-orthogonal corresponding orbitals are depicted in Fig. 7.18 together with the spatial overlap integrals $S = \langle \phi^\alpha | \phi^\beta \rangle$. The magnitude of the overlap of the magnetic orbitals is rather small with $S < 0.05$ for all SOMO pairs. Values reported in the literature suggest significantly larger overlap necessary for antiferromagnetic exchange interaction.^[91] In general, the visualization of the corresponding orbitals confirm the conclusions obtained from the spin density distributions.

7.3. Ferromagnetic Trinuclear Chromium(III) Complexes

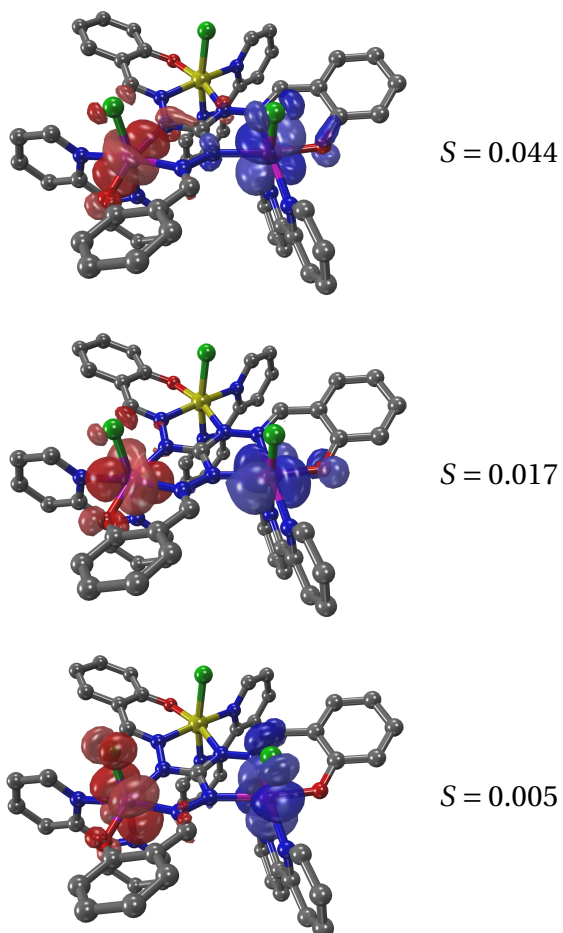


Figure 7.18.: Corresponding Orbitals obtained from the BS determinant of Cr_2Zn . α -spin-orbitals are depicted blue, β -spin-orbitals red, darker (lighter) lobes resemble positive (negative) sign of the wf (isosurface value $0.03 e/\text{\AA}^3$). On the right, values for the spatial overlap integrals are given.

CONCLUSION

In this work, several aspects of molecular magnetism were investigated. Synthetic works led to dinuclear complexes of transition metal ions, which, in the case of Co(II) exhibited slow magnetic relaxation properties. Multiconfigurational calculations on Co(II) complexes with different structural motifs gave insight into the ZFS in tetrahedral environments as well as into potentially high-performing SMMs due to linear coordination. The magnetic properties of lanthanide(III) complexes with the TAG ligand system were calculated with the CASSCF/RASSI methodology, and simulations of the susceptibilities were used for the interpretation of hydrogen-bond mediated interactions. A few open questions concerning exchange coupled systems were addressed with BS-DFT calculations.

Carbazole-Based Dinuclear Metallamacrocycles

The Schiff-base ligands **4** and **5** involving a substituted carbazole moiety were employed to prepare the five transition metal complexes **6-10** with the general constitution $[M_2(L)_2]$. The metal ions are coordinated in a strongly distorted (Cu(II)) or almost ideally tetrahedral (Co(II), Zn(II)) $[N_2O_2]$ environment. For the Cu(II) complexes **6** and **7**, measurements of the magnetic properties yielded weak antiferromagnetic exchange interactions of -2.3 and -2.4 cm^{-1} , respectively, which was also confirmed by BS-DFT. EPR measurements revealed axially of the g -tensor with a small rhombic distortion for **6**, and considerable hyperfine splitting for **7**. The Co(II) complexes **8** and **9** exhibited a rather large ZFS of $D = -37$ and -38 cm^{-1} , respectively, as determined by fits of the magnetization data. Furthermore, slow magnetic relaxation behavior was observed for both complexes, with **8** even showing an out-of-phase signal at zero applied field.

Electronic Structure of Tetrahedral Cobalt(II) SMMs

Eight tetrahedral and four square-planar Co(II) complexes with $[\text{N}_2\text{O}_2]$ donor sets were calculated with the CASSCF/CASPT2/RASSI-SO protocol. It was shown, that the correct prediction of the ground state multiplicity demanded the inclusion of dynamical correlation effects *via* CASPT2. Calculated spin-orbit energies are overestimated compared to measured relaxation barrier heights by 20-25%. In general, a larger distortion angle δ goes along with larger ZFS parameters and U_{eff} values, respectively. To further evaluate the connection between the distortion and spin-orbit interactions, calculations on a model complex with respect to the distortion angle δ were performed. The transition between quartet and doublet ground state was predicted for $20^\circ < \delta < 25^\circ$. Distortion angles below 60° cause significant mixing of the two lowest quartet states, which is accompanied by larger axial ZFS, but also increasing rhombicity.

Linear Cobalt(II) Complexes

Co(II) ions in a linear coordination environment were subject to multiconfigurational calculations. The small molecule CoCl_2 ($D_{\infty h}$ symmetry) was briefly investigated to get a general picture of the energy spectrum of linear Co(II) compounds. In contrast to earlier reports, sophisticated *ab initio* methods predicted a $^4\Phi_g$ ground state. This gives rise to a large overall angular momentum of $\Omega = \frac{9}{2}$ for the lowest SO state. The expected spin reversal barrier heights for the reported linear Co(II) complexes were found to be above 500 K for all complexes except one. Based on these results, dynamic susceptibility measurements are very likely to reveal SMM behavior with U_{eff} magnitudes not yet reported for Co(II) complexes.

Multiconfigurational Calculations on Lanthanide(III) SMMs

TAG ligands were shown to form complexes with lanthanide(III) ions in the works of Daus,^[185] Schuch,^[54] and Möller.^[55] Five Dy(III) and one Er(III) complexes have been investigated with the CASSCF/RASSI-SO methodology concerning their spin-orbit states. For the Dy(III) complexes, a well separated $|M_J = \pm \frac{15}{2}\rangle$ KD was found to be the ground state, which exhibits only small transversal elements of the g -tensor. A clear correlation between structural parameters and spin reversal barriers was not found. Intra-dimer interactions were treated considering the exact dipole-dipole interactions as well as arbitrary magnitudes of the exchange interactions, neatly explaining

the $\chi_M T$ data, that would otherwise be inaccessible for interpretation. The absence of slow magnetic relaxation at zero applied dc field for the Er(III) complex may be caused by the mixing of the different $|M_J\rangle$ states belonging to the $^4I_{15/2}$ ground term, as shown by decomposition of the SO wave functions.

Broken-Symmetry DFT Calculations on Oligonuclear Transition Metal Complexes

Cu₄O₄ Cubanes Eight complexes with a Cu₄O₄ cubane substructure employing sugar-derived ligand systems were investigated with the BS-DFT method. The two classes of 4+2 and 2+4 cubanes show different magnetic behavior due to their bridging motifs between Cu(II) ions. The antiferromagnetic exchange interaction in the 4+2 class cubanes between all nearest neighbors found by experiment is confirmed by the calculations. Furthermore, it was found, that the magnitude of J may vary with respect to the parameters $\angle(\text{Cu}-\text{O}-\text{Cu})$ and $\angle(\text{Cu}_{xy}-\text{Cu}_{xy})$. The susceptibility data for the calculated values was simulated with satisfying agreement with the experiment. 2+4 class cubanes exhibit preferably ferromagnetic exchange between Cu(II) ions close to each other, which was confirmed by BS-DFT. For complex **41**, however, one ferromagnetic and one antiferromagnetic J was found. This is in accordance to transition angle of $\angle(\text{Cu}-\text{O}-\text{Cu}) = 97.5^\circ$ suggested by Crawford.^[177]

Hexanuclear Copper(II) Metallacoronate The S_6 -symmetric hexanuclear Cu(II) metallacrown **42** was prepared earlier by Zharkuskaya. So far, the interpretation of the magnetic data gave unrealistic values for intra- and intermolecular exchange interactions. A reinvestigation of the experimental χ_M data showed, that, if intermolecular interactions are included, only the interaction between nearest neighbors has to be considered in order to describe the magnetic behavior. Intermediate antiferromagnetic exchange of $J_1 = -44 \text{ cm}^{-1}$ and a $\lambda = -33 \text{ cm}^{-3} \text{ mol}$ were found. Two approaches have been used to calculate the exchange interaction parameters with the BS-DFT: calculating $N + 1$ spin states to extract N interactions, and the substitution of paramagnetic Cu(II) ions with diamagnetic Zn(II). Both approaches confirmed antiferromagnetic exchange between neighboring Cu(II) ions, while the other interactions were also found to be close to zero. The superexchange pathway is mainly mediated by the shared μ_2 -oxo bridge in the xy -plane of neighboring Cu(II) ions. The magnitude of the exchange interaction is increased to a small extent by H_3O^+ guest ions due to the

8. Conclusion

hydrogen bonds, that cause an increase of spin density at the bridging oxygen atom.

Ferromagnetic Exchange in Chromium(III) Trimers The TAG ligand system forms trinuclear complexes with many transition metals in the oxidation states +2 and +3. Cr(III) complexes, in contrast to most other known complexes, exhibited small ferromagnetic exchange interactions. This behavior was confirmed by BS-DFT calculations on an optimized model complex, since no crystal structure data was available. An exchange interaction of $J = 3.8 \text{ cm}^{-1}$ was in good agreement with experimental values. Due to the symmetry of the singly occupied t_{2g} orbitals, an efficient superexchange pathway over the TAG ligand backbone is denied, and, hence, only a very small overlap of the magnetic orbitals is achieved. Corresponding orbital transformation yielded spatial overlap integrals below 0.02 of the SOMOs, which further confirms the findings.

ZUSAMMENFASSUNG

Im Laufe dieser Arbeit wurden diverse Aspekte des molekularen Magnetismus untersucht. Im synthetischen Teil wurden dinukleare Komplexe von Übergangsmetallen dargestellt, die im Falle der Cobalt(II)komplexe langsame magnetische Relaxation aufwiesen. Quantenchemische Rechnungen mit Multikonfigurationsmethoden an Cobalt(II)komplexen mit unterschiedlichen Strukturmotiven ermöglichten neue Erkenntnisse zur Nullfeldaufspaltung in tetraedrischen Koordinationsumgebungen sowie zu möglichem SMM-Verhalten von linearen Komplexen mit sehr hohen Relaxationsbarrieren. Das magnetische Verhalten von Lanthanoid(III)komplexen mit triaminoguanidin-basierten Liganden wurde mit der CASSCF/RASSI-SO Methodik berechnet. Die Simulation der Suszeptibilität lieferte Einblicke in die Wechselwirkungen innerhalb der wasserstoffverbrückten Dimere. Bisher noch nicht geklärte Fragen zu diversen austauschgekoppelten Systemen mit Übergangsmetallen wurden mit *Broken-Symmetry*-DFT-Rechnungen untersucht.

Carbazol-Basierte Dinukleare Metallmakrozyklen

Die Schiffbase-Liganden **4** und **5** mit Carbazolgrundgerüst wurden zur Synthese der fünf Übergangsmetallkomplexe **6-10** mit der allgemeinen Struktur $[M_2(L)_2]$ eingesetzt. Die Metallionen befanden sich in einer stark verzerrten (Cu(II)) oder nahezu ideal tetraedrischen (Co(II), Zn(II)) $[N_2O_2]$ -Koordinationsumgebung. Magnetische Messungen an den Kupfer(II)komplexen **6** und **7** lieferten schwache antiferromagnetische Wechselwirkungen von -2.3 und -2.4 cm^{-1} innerhalb der Dimere. Mit BS-DFT-Rechnungen konnte dies bestätigt werden. EPR-Messungen an den Kupfer-

9. Zusammenfassung

fer(II)komplexen zeigten axiale g -Tensoren mit kleiner rhombischer Verzerrung für **6** und deutlicher Hyperfeinstruktur für **7**. Die Cobalt(II)komplexe **8** und **9** wiesen einen relativ großen Nullfeldaufspaltungsparameter von $D < -35 \text{ cm}^{-1}$ auf, wie Anpassungen der Magnetisierungsdaten ergaben.

Elektronische Struktur von Tetraedrischen Cobalt(II)komplexen

Acht tetraedrische und vier quadratisch-planare Cobalt(II)komplexe mit $[\text{N}_2\text{O}_2]$ Donorsätzen wurden mit dem CASSCF/CASPT2/RASSI-SO-Protokoll berechnet. Es wurde gezeigt, dass die korrekte Vorhersage der Grundzustandsmultiplizität die Einbeziehung von dynamischen Korrelationseffekten *via* CASPT2 erfordert. Die berechneten Spin-Bahn-Energien überschätzen die gemessenen Relaxationsbarrieren um 20-25%. Tendenziell verursacht ein größerer Verzerrungswinkel δ eine größere Nullfeldaufspaltung und damit einhergehend größer Spinumkehrbarrieren U_{eff} . Um den Zusammenhang zwischen Verzerrung und Spin-Bahn-Wechselwirkungen zu erforschen, wurden Rechnungen an einem Modellkomplex in Abhängigkeit zum Winkel δ durchgeführt. Ein Übergang von einem Quartet- zu einem Dublettgrundzustand wird im Bereich $20^\circ < \delta < 25^\circ$ vorausgesagt. Für Verzerrungswinkel unter 60° zeigt sich signifikantes Mischen der zwei niedrigsten Quartetzustände, das von steigender Nullfeldaufspaltung, aber auch erhöhter Rhombizität begleitet wurde.

Lineare Cobalt(II)komplexe

Cobalt(II)ionen in einer linearen Koordinationsumgebung wurden mit Multikonfigurationsmethoden untersucht. Die Elektronenstruktur des Moleküls CoCl_2 (D_{2h} -Symmetry) wurde berechnet, um einen Überblick über die Zustandsstruktur in linearen Cobalt(II)verbindungen zu gewinnen. Anders als in einigen früheren Arbeiten wurde mit leistungsfähigen *ab initio* Methoden ein $^4\Phi_g$ Grundzustand gefunden. Dies gibt Grund zu der Annahme, dass der Spin-Bahn-Grundzustand einen sehr großen Gesamtdrehimpuls von $\Omega = \frac{9}{2}$ aufweist. Es wurden Relaxationsbarrieren von mehr als 500 K für alle bis auf einen zweifach koordinierten Cobalt(II)komplex berechnet. Aufgrund dieser Ergebnisse werden bei dynamischen Suszeptibilitätsmessungen an diesen Komplexen sehr hohe Werte für U_{eff} erwartet, die in dieser Größe noch nicht bei Cobalt(II) beobachtet wurden.

Multikonfigurationsrechnungen an Lanthanoid(III)-SMMs

Triaminoguanidin-basierte Liganden können zur Synthese von Lanthanoid(III)komplexen eingesetzt, wie in den Arbeiten von Daus,^[185] Schuch,^[54] und Möller^[55] nachgewiesen wurde. Fünf Dysprosium(III)- und ein Erbium(III)komplex waren Gegenstand von CASSCF/RASSI-SO-Rechnungen. Die Dysprosium(III)komplexe wiesen ein energetisch isoliertes $|M_J = \pm \frac{15}{2}\rangle$ Kramer-Dublett im Grundzustand auf, dass nur kleine Transversalelemente des g -Tensors zeigte. Zwischen den strukturellen Parametern und der Höhe der Relaxationsbarriere konnte kein klarer Zusammenhang nachgewiesen werden. Wechselwirkungen innerhalb der Dimere, einschließlich der Dipol-Dipol-Wechselwirkung als auch Austauschwechselwirkung festgelegter Größe, wurden mit Hilfe von Simulation der Suszeptibilitätsdaten untersucht. Damit konnte das Verhalten bei statischen SQUID-Messungen erklärt werden, das normalerweise einer Interpretation unzugänglich ist. Die Abwesenheit von langsamer magnetischer Relaxation ohne angelegtes externes Feld beim Erbium(III)komplex wird sehr wahrscheinlich durch das Mischen mehrerer $|M_J\rangle$ -Zustände des $^4I_{15/2}$ -Grundterms verursacht, wie in der Zerlegung der Spin-Bahn-Wellenfunktion gezeigt wurde.

Broken-Symmetry-DFT-Rechnungen an Oligonuklearen Übergangsmetallkomplexen

Cu₄O₄-Cubane Acht Komplexe mit Cu₄O₄-Substruktur und zuckerhaltigen Liganden wurden mit der BS-DFT Methode untersucht. Die zwei Unterklassen von 4+2- sowie 2+4-Cubanen zeigen unterschiedliches magnetisches Verhalten aufgrund ihrer Verbrückungsmotive zwischen den Kupfer(II)ionen. Die antiferromagnetische Austauschwechselwirkung zwischen benachbarten Kupfer(II)ionen in den 4+2-Cubanen konnte durch die Rechnungen bestätigt werden. Desweiteren wurde gezeigt, dass die Größe von J von den Strukturparametern $\angle(\text{Cu}-\text{O}-\text{Cu})$ und $\angle(\text{Cu}_{xy}-\text{Cu}_{xy})$ abhängt. Die Suszeptibilitätsdaten wurden mit den berechneten Kopplungskonstanten simuliert und zeigten zufriedenstellende Übereinstimmung mit dem Experiment. Die 2+4-Cubane zeigten vornehmlich ferromagnetischen Austausch zwischen nahe liegenden Kupfer(II)ionen. Nur für Komplex **41** wurde eine ferromagnetische und eine antiferromagnetische Wechselwirkung berechnet. Dies stimmt überein mit einem Übergangswinkel von $\angle(\text{Cu}-\text{O}-\text{Cu}) = 97.5^\circ$, der von Crawford postuliert wurde.^[177]

Hexanukleares Kupfer(II)metallacoronat Der S_6 -symmetrische hexanukleare Kupfer(II)metallakronenether **42** wurde in früheren Arbeiten von Zharkuskaya synthetisiert. Vorhergehende Untersuchungen der magnetischen Eigenschaften ergaben allerdings unrealistische Werte für die intra- und intermolekularen Austauschwechselwirkungen. Eine erneute Interpretation der χ_M -Messungen ergab, dass nur der Austausch zwischen direkt benachbarten Kupfer(II)ionen beachtet werden muss, sofern auch intermolekulare Wechselwirkung berücksichtigt werden. Es wurde ein antiferromagnetisches Verhalten mit $J_1 = -44 \text{ cm}^{-1}$ innerhalb des Cu_6 -Ringes sowie ein intermolekularer Austausch von $\lambda = -33 \text{ cm}^{-3} \text{ mol}$ ermittelt. Zwei verschiedene Ansätze zur Berechnung der Austauschparameter wurden verwendet: Berechnen der Energien von $N + 1$ Spinzuständen, um N Kopplungskonstanten zu erhalten, als auch das Ersetzen von allen außer zwei Kupfer(II)ionen mit diamagnetischem Zink(II). Beide Methoden bestätigten Antiferromagnetismus als dominierende Wechselwirkung. Zwischen übernächsten Nachbarn und gegenüberliegenden Ionen wurde keine Kooperativität gefunden. Der Superaustausch verläuft über eine μ_2 -Oxo-Verbrückung, die die xy -Ebenen benachbarter Kupfer(II)ionen verknüpft. Die Größe der Wechselwirkung wird zu einem Teil durch die H_3O^+ -Gastionen über Wasserstoffbrücken verstärkt, da diese eine Erhöhung der Spindichte an den verbrückenden Sauerstoffatomen verursachen.

Ferromagnetischer Austausch in Chrom(III)trimeren Die TAG-Liganden bilden mit zahlreichen Übergangsmetallen in den Oxidationsstufen +2 und +3 trinukleare Komplexe. Im Gegensatz zum Großteil der bekannten Komplexe zeigen die Chrom(III)komplexe ferromagnetisches Verhalten. Mit BS-DFT-Rechnungen konnte das Vorzeichen der Wechselwirkung unter Verwendung einer optimierten Modellstruktur bestätigt werden, da keine Kristallstrukturdaten erhalten werden konnten. Mit $J = 3.8 \text{ cm}^{-1}$ lag die Kopplungskonstante im Rahmen der rechnerischen Genauigkeit nah bei der experimentellen Größe. Aufgrund der Symmetrie der einfach besetzten t_{2g} -Orbitale des Chrom(III) kann über das TAG-Gerüst der Superaustausch nicht effektiv vermittelt werden, was zu einem sehr kleinen Überlapp der magnetischen Orbitale führt. Die *Corresponding Orbital Transformation* lieferte Überlappintegrale von weniger als 0.02, was auch auf Ferromagnetismus hindeutet.

Part III

Experimental Part

PHYSICAL MEASUREMENTS

10.1. Instruments

^1H and ^{13}C NMR spectra were recorded on a Bruker Avance 200 and 400 spectrometer. IR spectra for samples prepared as KBr pellets were measured on a Bruker IFS55/Equinox spectrometer with a Raman unit FRA 106/S. IR spectra of pure samples were measured with an additional Specac Golden Gate ATR unit. Thermogravimetric analysis (TGA) for powdered samples was performed on a NETZSCH STA409PC Luxx apparatus under constant flow of air ranging from room temperature up to 1000 °C with a heating rate of 1 °C/min. Mass spectra were measured on a Bruker MAT SSQ 710 spectrometer for FAB ionization and on a MAT 95XL Finnigan spectrometer for electrospray ionization. Elemental analysis (C, H, and N) was performed with a LECO CHNS/932 analyzer and a VARIO EL III analyzer. EPR spectra were recorded on a Bruker ESP300E using X-Band (9 GHz). Magnetic susceptibilities and magnetization data were measured on powdered samples prepared from crystalline complexes in gelatin capsules using a Quantum-Design MPMS-5 SQUID magnetometer equipped with a 5 T magnet in the temperature range from 300 to 2 K. The measured data were corrected for diamagnetism of the capsule and the intrinsic diamagnetism of the sample, estimated by measurements on a similar ligand system.

Cyclic voltammetric measurements were conducted in 3-electrode technique using a Reference 600 potentiostat (Gamry Instruments, Warminster, USA). The instrument was controlled by the DigiElch 7 software available from the same company. This program provides not only routines for the digital simulation of electrochemical ex-

10. Physical Measurements

periments but also those for performing the measurements in a consistent way making use of the Gamry Electrochemical Toolkit™ library. The CVs were measured in dichloromethane (containing 0.25M tetra-n-butylammonium- hexafluorophosphate) under a blanket of solvent-saturated argon. The ohmic resistance which had to be compensated for was determined by measuring the impedance of the system at potentials where the faradaic current was negligibly small. Background correction was accomplished by subtracting the current curves of the blank electrolyte (containing the same concentration of supporting electrolyte) from the experimental CVs. The working electrode was a 1.6 mm (Figure 1) or 3 mm (Figure 2) carbon disk electrode (ALS Japan). As reference electrode served a Ag/AgCl electrode in acetonitrile containing 0.25M tetra-n-butylammonium chloride. The potentials reported refer to the ferrocenium/ferrocene couple which was measured at the end of a series of experiments.

10.2. Crystal Structure Determination

Single crystals were selected from the mother liquor under a polarizing microscope and fixed on fine glass fibers. Crystallographic data was collected on a Nonius KappaCCD diffractometer employing graphite-monochromated Mo-K α radiation ($\lambda = 71.073$ pm). Summaries of the crystallographic and structure refinement data are given in Appendix B. The data was corrected for Lorentz and polarization effects, but not for absorption effects. Structures were solved by direct methods with SHELXS-97 and refined by full-matrix least-squares techniques against F_0^2 using SHELXL-97.^[186] Non-hydrogen atoms were refined anisotropically, while hydrogen atoms were calculated and treated as riding atoms with fixed thermal parameters. To model heavily disordered solvent molecules in the structures of **7**, **8**, and **9**, the SQUEEZE/BYPASS procedure was employed.^[114] Therein, disordered solvent molecules are only described as solvent containing voids, whose electron density is not used for refining the position of distinct atoms. Potential solvent containing areas are assigned automatically from the areas of the structure, that are outside of the van-der-Waals sphere of atoms belonging to the ordered part of the structure. Among these areas, only those able to contain at least one solvent molecule defined by the radius r are considered. The contribution of the solvent molecules is then subtracted from the observed data. The resulting file with the intensity of the reflexes is then used for the subsequent refinement procedure. Structure representations were done with the program OLEX2.^[187]

COMPUTATIONAL DETAILS

11.1. Broken-Symmetry Calculations

DFT calculations were performed using the TURBOMOLE 6.5 program package.^[188] For all atoms the triple- ζ basis set def2-TZPV proposed by Ahlrichs et al.^[189] was used. If not stated otherwise, hydrogen atoms were optimized prior to single point calculations and were carried out using the B88 exchange functional^[78] and the correlation functionals VWN(V)^[77] and P86^[80]. The geometry optimizations were accelerated further by employing the resolution of identity approximation. Single Point energies for estimating the exchange coupling constants were calculated using Becke's three parameter functional B3LYP.^[190] Tight convergence criteria were applied (`$scfconv = 8`).

11.2. Multiconfigurational Calculations

Crystal structures with optimized hydrogen atoms (RI-BP86, def2-SVP) were used. For the optimization, paramagnetic lanthanide(III) ions were replaced by the diamagnetic La(III) ion to achieve convergence of the SCF steps.

CASSCF,^[67] CASPT2^[191] and RASSI-SO^[104] calculations were carried out using MOLCAS 7.8.^[105] ANO-RCC type basis sets^[192–194] were used for all atoms (contractions: Ln ions –8s7p5d4f2g1h, Co–6s5p4d2f1g, coordinating O and N –4s3p2d1f, peripheral N and C–3s2p, H–2s). To save time and disk space, the Choleski decomposition was used.

Calculations on Cobalt(II) involved a (7,10) active space with a double d-set of orbitals. 10 quartet states and 40 doublet states were calculated within the CASSCF pro-

11. Computational Details

cedure to account for all states arising from a d^7 configuration. CASPT2 calculations were done on all quartet states and on the 12 lowest doublet states. Otherwise, intruder states were regularly encountered. RASSI-SO calculations were performed on the CASPT2 wave functions for the states calculated.

For lanthanide complexes, a CAS(n , 7) was chosen, with n being the number of f-electrons for the lanthanide(III) ion. The CASSCF calculations were performed including on a number of states depending of the specific lanthanide(III) ion. CASPT2 calculations were omitted for lanthanide(III) complexes. The RASSI procedure included all calculated states of all multiplicities.

Calculations of the magnetic properties for mononuclear complexes were done using the SINGLE_ANISO^[96] module. Magnetic properties of the hydrogen-bridged Dy(III) dimers were calculated with the POLY_ANISO^[98] module.

12.1. Materials

Raney nickel was stored under water and was washed with ethanol and ethyl acetate prior to usage. All solvents and reagents were used as received without further purification.

12.2. Preparation

1,3,6,8-Tetra-*tert*-butyl-9*H*-cabazole (1)

This compound was synthesised according to a reported procedure.^[111]

Sum formula: C₂₈H₄₁N, 391.63 g/mol.

Yield: 72%, colorless crystals, mp. 191°C.

¹H-NMR (400 MHz, CDCl₃, ppm): δ = 8.17 (s, 1H, NH), 7.97 (s, 2H, CH), 7.43 (d, 2H, CH, ⁴J = 1.6 Hz), 1.62 (s, 18H, H^{tBu}), 1.49 (s, 18H, H^{tBu}).

¹³C-NMR (100 MHz, CDCl₃, ppm): δ = 142.0, 135.2, 131.6, 123.8, 120.1, 113.9, 34.8, 34.7, 32.1, 30.4.

12. Synthesis

1,8-Di-*tert*-butyl-3,6-dinitro-9*H*-carbazole (2)

Copper(II) nitrate trihydrate (1.74 g, 7.2 mmol) was solved in a mixture of glacial acetic acid (5 ml) und acetic acid anhydride (15 ml) at 55 °C. Then **1** (2.34 g, 6.0 mmol) was added to the solution as well as additional acetic acid (5 ml) and acetic acid anhydride (25 ml). This mixture was stirred for 15 minutes at 70 °C. After the solution was allowed to cool to room temperature, it was poured into water (200 ml), yielding a yellow precipitate. The solid was filtered off, washed with water and heated with ethanol (150 ml). After the suspension cooled down to room temperature, the product was filtered off and washed several times with ethanol to give a pale yellow solid.

Sum formula: C₃₀H₂₃N₃O₄, 369.41 g/mol.

Yield: 69%, colorless crystals, mp. 292°C.

¹H-NMR (400 MHz, CDCl₃, ppm): δ = 8.93–9.02 (m, 3H, CH, NH), 8.40 (d, 2H, CH), 1.68 (s, 18H, H^{*t*Bu}).

¹³C-NMR (100 MHz, CDCl₃, ppm): δ = 142.3, 140.9, 134.1, 123.6, 119.7, 115.5, 34.9, 30.3.

MS (DED): 369 [M⁺], 354, 339, 326, 308, 293, 247, 204, 170.

IR (ATR, cm⁻¹): $\tilde{\nu}$ = 3508 w (NH), 2965 w (CH₃, $\tilde{\nu}_{\text{as}}$), 1587 w, 1521 m, 1487 m, 1396 w, 1370 w, 1324 s, 1304 m, 1261 w, 1221 w, 1185 w, 1125 w, 1068 w, 924 w, 897 m, 881 w, 828 w, 746 s, 664 w, 588 w, 552 w, 461 m, 409 m.

Elemental analysis for C₃₀H₂₃N₃O₄ (369.41 g/mol): calculated (%) = C 65.03, H 6.28, N 11.37; found (%) = C 65.28, H 6.14, N 11.39.

3,6-Diamino-1,8-di-*tert*-butyl-9*H*-carbazole (3)

2 (3.7 g, 10.0 mmol) was suspended in ethyl acetate (50 ml). A spatula of Raney nickel was added to the suspension. This mixture was heated to 80 °C in an autoclave with a hydrogen atmosphere (60 bar). After 8 hours the solution was allowed to cool to room temperature and the excess of hydrogen was released. The Raney nickel was filtered off and the solvent was removed from the filtrate by distillation *in vacuo*. The product **3** was obtained as a colorless powder. It was used without further purification.

General Synthesis of the Ligands

To a methanolic solution (10 ml) of **3** (1.33 g, 4.3 mmol), the desired derivative of salicylic aldehyde (9.2 mmol) was added. The solution turned instantly yellow and after 10 to 30 minutes, a yellow solid precipitated. The reaction mixture was refluxed for an additional hour. After allowing the reaction mixture to cool down, the solid was collected by filtration and washed with a few ml of methanol.

$\text{H}_2\text{L}^{\text{H}}$ (**4**)

Salicyl aldehyde (1.0 ml, 9.2 mmol) was added.

Sum formula: $\text{C}_{34}\text{H}_{35}\text{N}_3\text{O}_2$, 517.66 g/mol.

Yield: 89%, yellow crystals, mp. 259°C.

$^1\text{H-NMR}$ (400 MHz, CDCl_3 , ppm): δ = 8.83 (s, 1H, CH), 8.45 (s, 1H, NH), 7.96 (s, 2H, CH), 7.35-7.55 (m, 6H, CH, H^{imin}), 7.05-7.12 (m, 2H, CH), 6.94-7.03 (m, 2H, CH), 1.67 (s, 18H, H^{tBu}).

$^{13}\text{C-NMR}$ (100 MHz, CDCl_3 , ppm): δ = 161.1, 160.4, 141.3, 136.5, 133.8, 132.6, 131.9, 124.6, 119.6, 118.4, 117.2, 109.3 (CH), 34.7 ($\text{C}(\text{CH}_3)_3$), 30.4 (CH_3).

MS (FAB): 518 [M^+], 502, 468, 475, 460, 446, 424, 413, 398, 382, 367, 339, 325, 307, 289, 259, 242, 230, 204.

IR (KBr, cm^{-1}): $\tilde{\nu}$ = 3523 m (NH), 3447 wb (OH), 3055 w (CH^{ar}), 2963 s, 2933 w, 2906 w, 2870 w (all CH_3), 1617 s, 1572 m, 1498 m, 1458 m, 1420 m, 1396 m, 1369 m, 1320 w, 1294 m, 1279 m, 1234 w, 1196 w, 1177 w, 1152 m, 1115 m, 1034 w, 974 w, 955 w, 944 w, 905 w, 883 w, 876 w, 853 w, 768 m, 752 s, 738 w, 626 w, 585 w.

Elemental analysis for $\text{H}_2\text{L}^{\text{H}}$ [$\text{C}_{34}\text{H}_{35}\text{N}_3\text{O}_2$] (517.66 g/mol): calculated (%) = C 78.89, H 6.81, N 8.12; found (%) = C 78.50, H 6.97, N 8.08.

$\text{H}_2\text{L}^{\text{tBu}}$ (**5**)

3,5-Di-*tert*-butyl salicyl aldehyde (2.15 g, 9.2 mmol) was added.

Sum formula: $\text{C}_{50}\text{H}_{67}\text{N}_3\text{O}_2$, 742.09 g/mol.

Yield: 78%, yellow needles, mp. 322 (dec.)°C.

$^1\text{H-NMR}$ (400 MHz, CDCl_3 , ppm): δ = 14.12 (s, 2H, OH), 8.83 (s, 2H, H^{imin}), 8.39 (s, 1H, NH), 7.93 (d, 2H, CH, 4J = 1.4 Hz), 7.45 (d, 2H, CH, 4J = 2.2 Hz), 7.41 (d, 2H, CH, 4J =

12. Synthesis

1.6 Hz), 7.29 (d, 2H, CH, $^4J = 2.2$ Hz), 1.64 (s, 18H, H^{tBu}), 1.51 (s, 18H, H^{tBu}), 1.36 (s, 18H, H^{tBu}).

¹³C-NMR (50 MHz, CDCl₃, ppm): $\delta = 161.4, 158.1, 141.3, 140.4, 136.8, 133.6, 127.4, 126.6, 124.6, 118.7, 118.5, 109.0, 35.1, 34.2, 31.5, 30.4, 29.5$.

MS (FAB): 742 [M⁺], 726, 686, 670, 630, 612, 552, 536, 525, 494, 438, 407, 379, 332, 321, 307, 289, 244, 218.

IR (ATR, cm⁻¹): $\tilde{\nu} = 3529$ w (NH), 2954 s, 2905 m, 2869 m (all CH₃), 1614 m, 1573 m, 1471 s, 1392 m, 1361 w, 1249 m, 1170 s, 944 w, 879 m, 853 m, 773 w, 733 w, 660 w, 634 w, 506 w, 440 w, 417 w.

Elemental analysis for H₂L^{tBu} [C₅₀H₆₇N₃O₂] (742.09 g/mol): calculated (%) = C 80.93, H 9.10, N 5.66; found (%) = C 80.77, H 9.21, N 5.58.

General Synthesis of the Complexes

A solution of the ligand (0.25 mmol) in chloroform (3 ml) in a test tube was overlaid with a solvent mixture (methanol/chloroform 1:1, 4 ml). A solution of the metal acetate (0.25 mmol) in methanol (3 ml) was added as the third layer. The test tube was sealed with a glass stopper and after one week single crystals of the complex were filtered off and washed with methanol/chloroform 1:1.

[Cu₂(L^H)₂] (6)

Cu(OAc)₂ · H₂O (50 mg, 0.25 mol) and ligand H₂L^H (129 mg, 0.25 mol) were used.

Sum formula: C₆₈H₆₆Cu₂N₆O₄, 1158.38 g/mol.

Yield: 54%, brown crystals, mp. > 300 (dec.)°C.

MS (Micro-ESI): 1157 [M⁺], 413.

IR (KBr, cm⁻¹): $\tilde{\nu} = 3522$ m (NH), 3073 w, 3054 w, 3019 m (all CH^{ar}), 2962 w, 2907 w, 2869 w (all CH₃), 1619 s, 1603 s, 1533 m, 1492 w, 1465 w, 1438 m, 1420 w, 1407 w, 1395 w, 1367 w, 1344 m, 1320 m, 1295 w, 1234 w, 1177 m, 1148 m, 1123 w, 1030 w, 945 w, 912 w, 877 w, 862 w, 751 m, 737 m.

Elemental analysis for [Cu₂(L^H)₂] [C₆₈H₆₆Cu₂N₆O₄] (1158.38 g/mol): calculated (%) = C 70.51, H 5.74, N 7.25; found (%) = C 70.28, H 5.73, N 7.04.

X-Ray Structure: fo4112.

[Cu₂(L^{tBu})₂] (7)

Cu(OAc)₂ · H₂O (50 mg, 0.25 mol) and ligand H₂L^{tBu} (183 mg, 0.25 mol) were used.

Sum formula: C₁₀₀H₁₃₀Cu₂N₆O₄, 1607.23 g/mol.

Yield: 40%, brown crystals, mp. > 300 (dec.)°C.

MS (Micro-ESI): 1605 [M⁺], 742, 615, 587, 559, 413, 301, 273, 255.

IR (KBr, cm⁻¹): $\tilde{\nu}$ = 3528 w (NH), 2959 s, 2907 w, 2870 w (all CH₃), 1615 s, 1596 s, 1525 m, 1492 w, 1428 m, 1385 w, 1362 w, 1325 w, 1296 w, 1254 w, 1166 s, 1132 w, 879, w, 856 w, 835 w, 789 w, 745 w, 535 w, 520 w.

Elemental analysis for [Cu₂(L^{tBu})₂] [C₁₀₀H₁₃₀Cu₂N₆O₄] (1607.23 g/mol): calculated (%) = C 74.73, H 8.15, N 5.23; found (%) = C 74.64, H 8.28, N 5.15.

X-Ray Structure: fo4111.

[Co₂(L^H)₂] (8)

Co(OAc)₂ · 4 H₂O (63 mg, 0.25 mol) and ligand H₂L^H (129 mg, 0.25 mol) were used.

Sum formula: C₆₈H₆₆Co₂N₆O₄, 1148 g/mol.

Yield: 60%, red crystals, mp. > 300 (dec.)°C.

MS (ESI): 1149 [M⁺], 1171 [M + Na⁺], 518.

IR (ATR, cm⁻¹): $\tilde{\nu}$ = 3526 w (NH), 2960 w, 2871 w (all CH₃), 1593 s, 1532 s, 1438 s, 1298 s, 1147 s, 853 m, 754 vs, 574 m, 520 m, 477 m, 440 m.

Elemental analysis for [Co₂(L^H)₂]·4CHCl₃·MeOH [C₇₃H₇₄Co₂N₆O₅Cl₁₂] (1658.7 g/mol): calculated (%) = C 52.86, H 4.50, N 5.06; found (%) = C 52.84, H 4.25, N 5.03.

X-Ray Structure: fo4385.

[Co₂(L^{tBu})₂] (9)

Cu(OAc)₂ · H₂O (63 mg, 0.25 mol) and ligand H₂L^{tBu} (183 mg, 0.25 mol) were used.

Sum formula: C₁₀₀H₁₃₀Co₂N₆O₄, 1598.0 g/mol.

Yield: 57%, red crystals, mp. > 300 (dec.)°C.

MS (ESI): 1598 [M⁺], 1620 [M + Na⁺], 1541, 742.

IR (ATR, cm⁻¹): $\tilde{\nu}$ = 3526 v (NH), 2957 s, 2904 m, 2869 m (all CH₃), 1585 s, 1525 s, 1490 w, 1421 s, 1383 m, 1320 w, 1296 w, 1253 m, 1163 vs, 1133 w, 883 w, 853 w, 837 w, 787 w,

12. Synthesis

751 vs, 550 m, 521 m, 482 w, 440 w.

Elemental analysis for $[\text{Co}_2(\text{L}^{\text{tBu}})_2]$ $[\text{C}_{100}\text{H}_{130}\text{Co}_2\text{N}_6\text{O}_4]$ (1598.0 g/mol): calculated (%) = C 75.16, H 8.20, N 5.26; found (%) = C 74.69, H 8.19, N 5.35.

X-Ray Structure: fo4384.

$[\text{Zn}_2(\text{L}^{\text{H}})_2]$ (10)

$\text{Zn}(\text{OAc})_2 \cdot 2\text{H}_2\text{O}$ (55 mg, 0.25 mol) and ligand $\text{H}_2\text{L}^{\text{H}}$ (129 mg, 0.25 mol) were used.

Sum formula: $\text{C}_{68}\text{H}_{66}\text{Zn}_2\text{N}_6\text{O}_4$, 1162.07 g/mol.

Yield: 38%, yellow crystals, mp. > 300 (dec.)°C.

MS (Micro-ESI): 1159 $[\text{M}^+]$, 587, 518, 414.

IR (ATR, cm^{-1}): $\tilde{\nu}$ = 3522 w (NH), 3435 wb (OH), 3051 w, 3018 w (all CH^{ar}), 2961 m, 2907 w, 2871 w (all CH_3), 1618 s, 1603 vs, 1533 s, 1493 m, 1464 s, 1443 s, 1419 m, 1386 w, 1368 w, 1346 m, 1320 m, 1295 w, 1248 w, 1235 w, 1174 m, 1148 s, 1124 w, 1031 w, 983 w, 962 w, 946 w, 914 w, 881, w, 854 m, 755 s, 740 m, 663 w, 607 w, 568 w, 520 w, 476 w, 432 w.

Elemental analysis for $[\text{Zn}_2(\text{L}^{\text{H}})_2] \cdot 1.5\text{CHCl}_3$ $[\text{C}_{69.5}\text{H}_{67.5}\text{Zn}_2\text{N}_6\text{O}_4\text{Cl}_{4.5}]$ (1341.14 g/mol): calculated (%) = C 62.24, H 5.07, N 6.26; found (%) = C 61.87, H 5.24, N 5.99.

X-Ray Structure: fo4113.

Appendix

STRUCTURAL DETAILS

A.1. Carbazole-Based Complexes

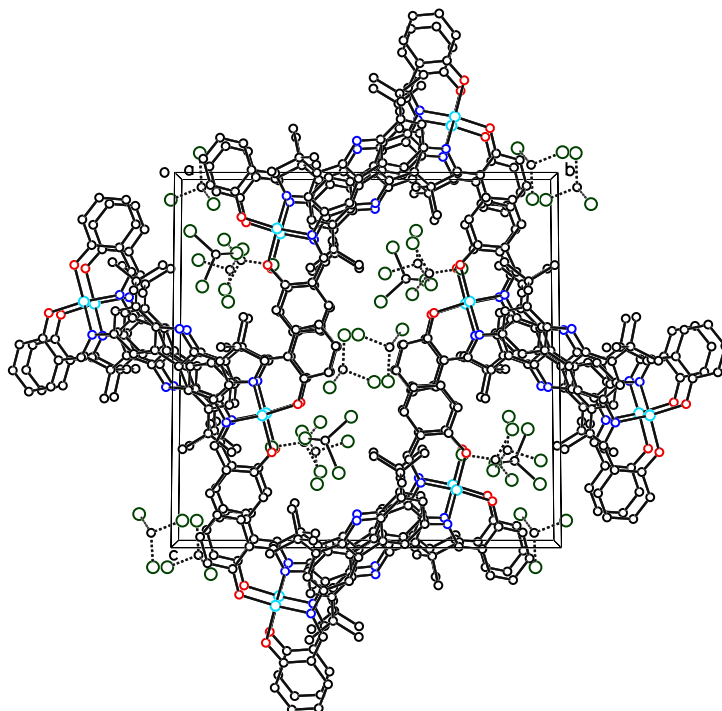


Figure A.1.: Packing diagram of $[\text{Cu}_2(\text{L}^{\text{H}})_2] \cdot 5 \text{CHCl}_3$ (**6**), viewing along $[100]$ direction of the crystal lattice. Although this view seemingly shows π - π stacking between the salicylidene moieties, the molecules are translated by $1a = 1096.47 \text{ pm}$. Hydrogen atoms were omitted for the sake of clarity.

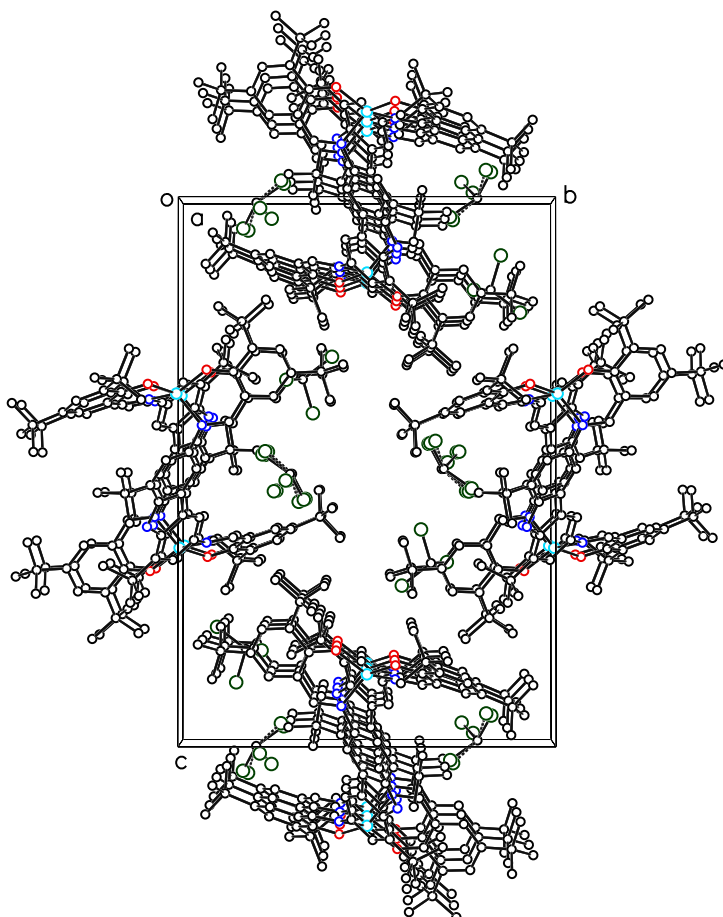


Figure A.2.: Packing diagram of $[\text{Cu}_2(\text{L}^{\text{tBu}})_2] \cdot 2.75 \text{CHCl}_3$ (**7**), viewing along $[100]$ direction of the crystal lattice. Although this view seemingly shows π - π stacking between the salicylidene moieties, the molecules are translated by $1a = 1230.77 \text{ pm}$. Hydrogen atoms were omitted for the sake of clarity.

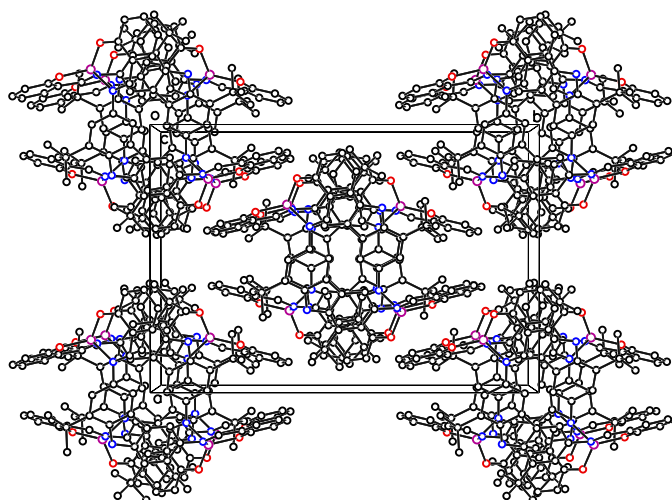


Figure A.3.: Packing diagram of $[\text{Co}_2(\text{L}^{\text{H}})_2] \cdot 2.67 \text{CHCl}_3$ (**8**), viewing along $[001]$ direction of the crystal lattice. Hydrogen atoms were omitted for the sake of clarity.

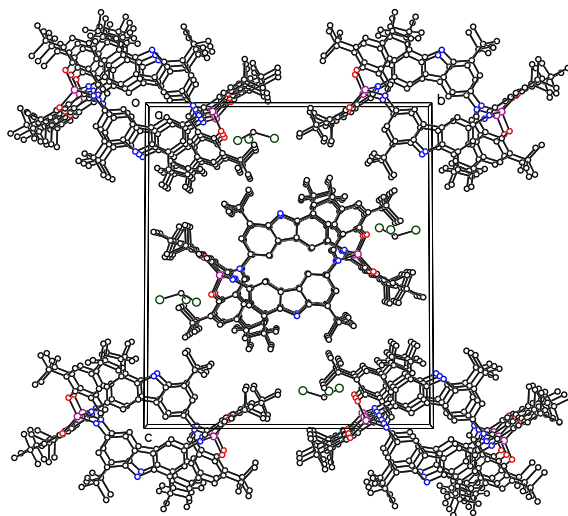


Figure A.4.: Packing diagram of $[\text{Co}_2(\text{L}^{\text{tBu}})_2] \cdot 4.75 \text{CHCl}_3$ (**9**), viewing along $[100]$ direction of the crystal lattice. Although this view seemingly shows π - π stacking between the salicylidene moieties, the molecules are translated by $1a = 1230.77 \text{ pm}$. Hydrogen atoms were omitted for the sake of clarity.

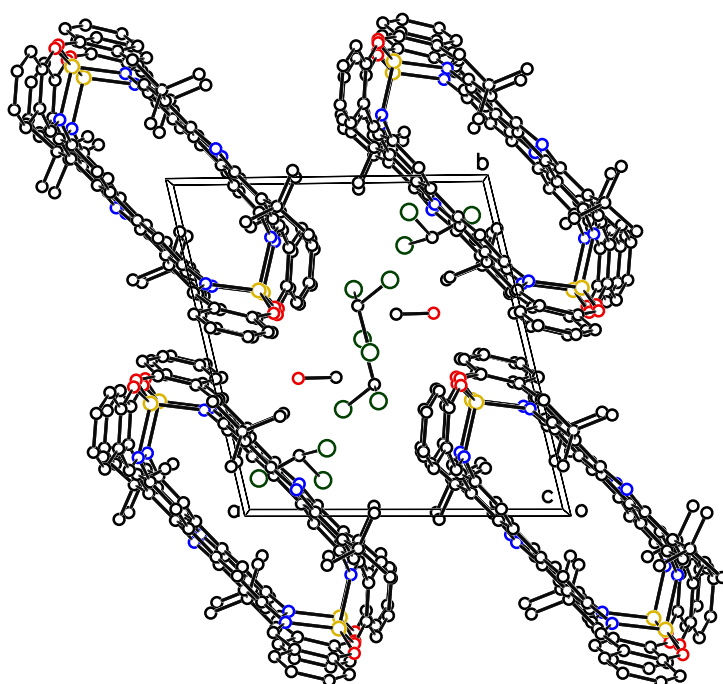


Figure A.5.: Packing diagram of $[\text{Zn}_2(\text{L}^{\text{H}})_2] \cdot 4 \text{CHCl}_3 \cdot 2 \text{MeOH}$ (**10**), viewing along $[001]$ direction of the crystal lattice. Hydrogen atoms were omitted for the sake of clarity.

APPENDIX

B

CRYSTALLOGRAPHIC DETAILS

B. Crystallographic Details

Table B.1.: Crystallographic data and structure refinement parameters for compound $[\text{Cu}_2(\text{L}^{\text{H}})_2] \cdot 5\text{CHCl}_3$ (**6**). Internal structure code: fo4112.

Formula	$\text{C}_{73}\text{H}_{71}\text{Cl}_{15}\text{Cu}_2\text{N}_6\text{O}_4$
Formular weight [g/mol]	1755.18
Crystal size [mm^3]	0.6x0.6x0.3
Crystal system	monoclinic
Space group	$P2_1/c$
Lattice parameters	
<i>a</i> [pm]	1096.470(10)
<i>b</i> [pm]	1922.12(3)
<i>c</i> [pm]	1932.45(3)
α [°]	90
β [°]	105.2680(10)
γ [°]	90
Cell volume <i>V</i> [10^6 pm^3]	3928.98(10)
<i>Z</i>	2
Δ_{calc} [g cm^{-3}]	1.484
$\mu(\text{Mo K}\alpha)$ [mm^{-1}]	1.103
θ data collection range [°]	$2.718 \leq \theta \leq 27.514$
Reflection measured	24604
unique reflections / R_{int}	8937/0.0201
Goodness-of-fit on F^2	1.053
<i>R</i> indices (all data)	$R_1 = 0.0529, wR_2 = 0.1187$
final <i>R</i> indices ($F > ((2\sigma(F))^2)^2$)	$R_1 = 0.0439, wR_2 = 0.1104$
$R = \sum (F_0 - F_c) / \sum F_0 , wR = (\sum w(F_0^2 - F_c^2)^2 / \sum w(F_0^2)2)^{1/2}$	

Table B.2.: Crystallographic data and structure refinement parameters for compound $[\text{Cu}_2(\text{L}^{\text{tBu}})_2] \cdot 2.75\text{CHCl}_3$ (7). Internal structure code: fo4111.

Formula	$\text{C}_{104}\text{H}_{134}\text{Cl}_{12}\text{Cu}_2\text{N}_6\text{O}_4$
Formular weight [g/mol]	2084.64
Crystal size [mm^3]	0.6x0.6x0.5
Crystal system	monoclinic
Space group	$P2_1/n$
Lattice parameters	
<i>a</i> [pm]	1230.77(5)
<i>b</i> [pm]	1780.55(7)
<i>c</i> [pm]	2596.54(9)
α [°]	90
β [°]	92.768(2)
γ [°]	90
Cell volume <i>V</i> [10^6 pm^3]	5683.5(4)
<i>Z</i>	2
Δ_{calc} [g cm^{-3}]	1.218
$\mu(\text{Mo K}\alpha)$ [mm^{-1}]	0.705
θ data collection range [°]	$1.570 \leq \theta \leq 27.510$
Reflection measured	21272
unique reflections / R_{int}	11176/0.0254
Goodness-of-fit on F^2	1.091
<i>R</i> indices (all data)	$R_1 = 0.0929, wR_2 = 0.2473$
final <i>R</i> indices ($F > (2\sigma(F))^2$)	$R_1 = 0.0807, wR_2 = 0.2364$
$R = \frac{\sum (F_0 - F_c)}{\sum F_0 }, wR = \frac{(\sum w(F_0^2 - F_c^2)^2)}{\sum w(F_0^2)^2}^{1/2}$	

B. Crystallographic Details

Table B.3.: Crystallographic data and structure refinement parameters for compound $[\text{Co}_2(\text{L}^{\text{H}})_2] \cdot 2.67\text{CHCl}_3$ (**8**). Internal structure code: fo4385.

Formula	$\text{C}_{68}\text{H}_{66}\text{Co}_2\text{N}_6\text{O}_4$
Formular weight [g/mol]	1149.12
Crystal size [mm^3]	0.5x0.6x0.5
Crystal system	monoclinic
Space group	$C2/c$
Lattice parameters	
a [pm]	1589.24(3)
b [pm]	2305.17(4)
c [pm]	1802.97(3)
α [°]	90
β [°]	91.7510(10)
γ [°]	90
Cell volume V [10^6 pm^3]	6602.0(2)
Z	4
Δ_{calc} [g cm^{-3}]	1.156
$\mu(\text{Mo K}\alpha)$ [mm^{-1}]	0.551
θ data collection range [°]	$1.901 \leq \theta \leq 27.501$
Reflection measured	22594
unique reflections / R_{int}	7573/0.0403
Goodness-of-fit on F^2	1.105
R indices (all data)	$R_1 = 0.0631, wR_2 = 0.1634$
final R indices ($F > (2\sigma(F))^2$)	$R_1 = 0.0502, wR_2 = 0.1542$
$R = \sum (F_0 - F_c) / \sum F_0 , wR = (\sum w(F_0^2 - F_c^2)^2 / \sum w(F_0^2)2)^{1/2}$	

Table B.4.: Crystallographic data and structure refinement parameters for compound $[\text{Co}_2(\text{L}^{\text{tBu}})_2] \cdot 4.75\text{CHCl}_3$ (**9**). Internal structure code: fo4384.

Formula	$\text{C}_{102}\text{H}_{132}\text{Cl}_6\text{Co}_2\text{N}_6\text{O}_4$
Formular weight [g/mol]	1836.70
Crystal size [mm^3]	0.6x0.5x0.5
Crystal system	monoclinic
Space group	$P2_1/c$
Lattice parameters	
<i>a</i> [pm]	1025.04(1)
<i>b</i> [pm]	2179.82(2)
<i>c</i> [pm]	2508.82(3)
α [°]	90
β [°]	100.616(1)
γ [°]	90
Cell volume <i>V</i> [10^6 pm^3]	5509.77(10)
<i>Z</i>	2
Δ_{calc} [g cm^{-3}]	1.107
$\mu(\text{Mo K}\alpha)$ [mm^{-1}]	0.493
θ data collection range [°]	$1.868 \leq \theta \leq 27.482$
Reflection measured	39088
unique reflections / R_{int}	12621/0.0362
Goodness-of-fit on F^2	1.085
<i>R</i> indices (all data)	$R_1 = 0.0653, wR_2 = 0.1504$
final <i>R</i> indices ($F > (2\sigma(F))^2$)	$R_1 = 0.0541, wR_2 = 0.1443$
$R = \frac{\sum (F_0 - F_c)}{\sum F_0 }, wR = \frac{(\sum w(F_0^2 - F_c^2)^2)}{\sum w(F_0^2)^2}^{1/2}$	

B. Crystallographic Details

Table B.5.: Crystallographic data and structure refinement parameters for compound $[\text{Zn}_2(\text{L}^{\text{H}})_2] \cdot 4 \text{CHCl}_3 \cdot 2 \text{MeOH}$ (**10**). Internal structure code: fo4113.

Formula	$\text{C}_{74}\text{H}_{78}\text{Cl}_{12}\text{N}_6\text{O}_6\text{Zn}_2$
Formular weight [g/mol]	1703.56
Crystal size [mm^3]	0.6x0.6x0.4
Crystal system	triclinic
Space group	$P\bar{1}$
Lattice parameters	
a [pm]	1231.55(5)
b [pm]	1297.66(3)
c [pm]	1338.58(5)
α [°]	77.092(2)
β [°]	72.586(2)
γ [°]	73.880(2)
Cell volume V [10^6 pm^3]	1937.83(12)
Z	1
Δ_{calc} [g cm^{-3}]	1.460
$\mu(\text{Mo K}\alpha)$ [mm^{-1}]	1.087
θ data collection range [°]	$3.846 \leq \theta \leq 27.533$
Reflection measured	11407
unique reflections / R_{int}	8542/0.0194
Goodness-of-fit on F^2	1.105
R indices (all data)	$R_1 = 0.0537, wR_2 = 0.0969$
final R indices ($F > (2\sigma(F))^2$)	$R_1 = 0.0438, wR_2 = 0.0892$
$R = \sum (F_0 - F_c) / \sum F_0 , wR = (\sum w(F_0^2 - F_c^2)^2 / \sum w(F_0^2))^2)^{1/2}$	

CONTINUOUS SHAPE MEASURES

The Continuous Symmetry Measure (CSM)^[195] and Continuous Shape Measure (CShM)^[196] were introduced to quantify the degree of distortion of a set of atoms from a certain idealized structure, i.e. an ideal polyhedron. The shape measure S of the coordination sphere AB_{N-1} (the polyhedron Q) relative to the ideal polyhedron P requires the N vectors \vec{q}_i . Then, P is rotated, translated, and scaled in such a way, that minimizes the function in Eq. (C.1), yielding the shape measure $S_Q(P)$. \vec{q}_i is the position vector of the center of Q .

$$S_Q(P) = \min \left[\frac{\sum_{i=1}^N |\vec{q}_i - \vec{p}_i|^2}{\sum_{i=1}^N |\vec{q}_i - \vec{q}_0|^2} \right] \times 100 \quad (\text{C.1})$$

Due to the regularly encountered ambiguity of this procedure (similarities to different polyhedra P are almost equal), minimal distortion pathways between such ideal polyhedra were defined,^[197] yielding the deviation from the minimal distortion pathway and the “position” (angular fraction $\Phi_{P1 \rightarrow P2}$ [%]) on this transition. The calculations were performed with the program SHAPE.^[198]

C.1. Similarities for Co(II) Complexes

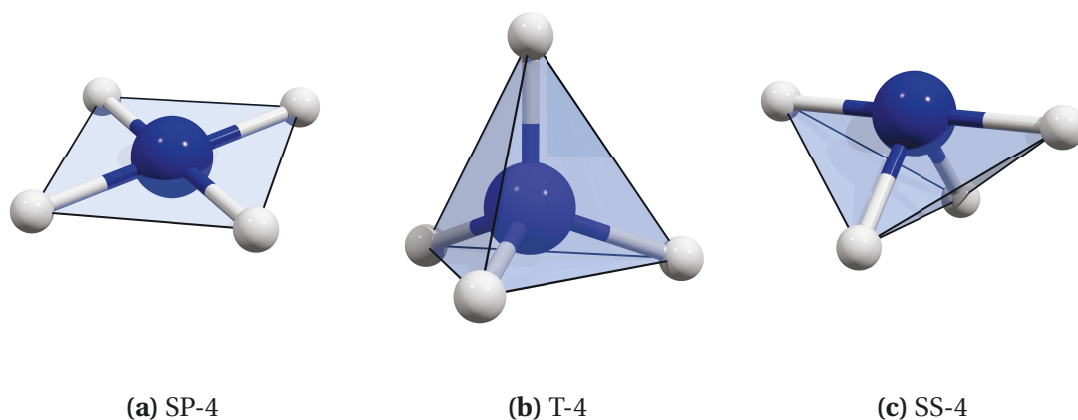


Figure C.1.: Ideal coordination polyhedra used for computing similarities of fourfold coordinated Co(II) complexes.

Complex	S_{SP4}	S_{T4}	S_{SS4}	$\Phi_{SP4 \rightarrow T4}$
8	23.356	1.921	6.275	82.0
9	24.211	1.978	7.006	83.6
11	15.454	4.927	5.510	65.6
12	25.855	1.824	7.717	86.7
13	25.504	1.882	7.608	86.0
14	18.972	3.030	5.229	73.2
15	19.206	3.202	5.127	73.7
16	20.588	2.743	5.739	76.5

Table C.1.: Calculated CShM similarities for Co(II) complexes with $[N_2O_2]$ coordination environment.

C.2. Similarities for Dy(III) Complexes

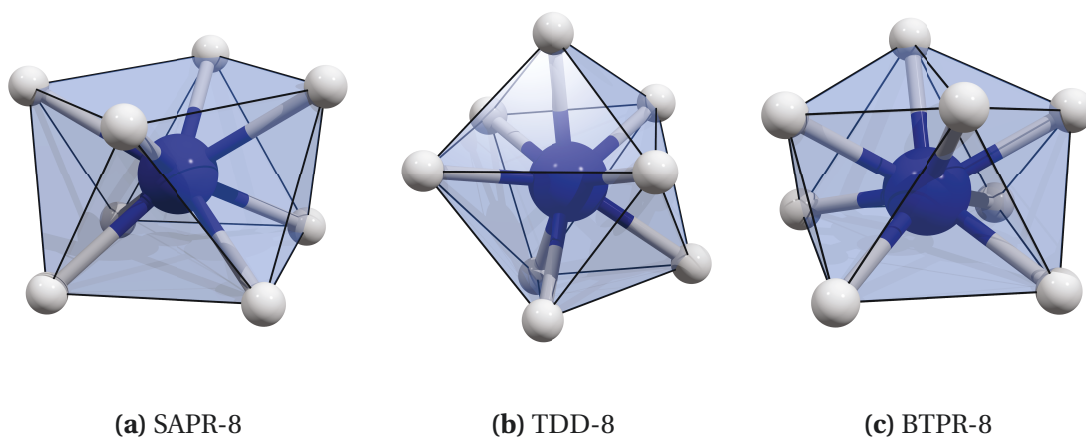


Figure C.2.: Ideal coordination polyhedra used for computing similarities of eightfold coordinated Dy(III) complexes.

Table C.2.: CShMs of the coordination sphere of the Dy(III) ions of the investigated complexes for selected ideal shapes.

Complex	$S_{\text{SAPR-8}}$	$S_{\text{TDD-8}}$	$S_{\text{BTPR-8}}$
28	3.20	0.72	1.63
29	3.51	1.00	1.83
30	3.31	0.80	2.15
31	2.32	2.42	4.10
32	3.15	2.83	2.99

ADDITIONAL DETAILS FOR QUANTUMMECHANICAL
CALCULATIONS

**D.1. CASSCF and CASPT2 Calculations on
Tetrahedral Cobalt(II) SMMs**

D. Additional Details for Quantummechanical Calculations

Table D.1.: CASSCF energies [cm^{-1}] of the ten quartet and the 30 lowest doublet states for the tetrahedral Co(II) complexes investigated in Chapter 4.

	8	9	11	12	13	14	15	16
quartet states	0	0	0	0	0	0	0	0
	2095	2050	1682	2135	2160	2000	1645	1707
	5723	5791	4228	6581	6500	4839	4690	5136
	5940	6315	5836	6586	6661	6141	6048	5840
	7839	7635	8955	7676	7735	9287	8388	7959
	8910	8858	9493	8691	8729	9723	8880	8640
	10784	10965	9923	10145	9976	10454	9799	9944
	21480	21207	22519	22064	22261	22111	22013	21760
	23292	23541	22601	23757	23666	22848	22636	22759
	25639	25933	27260	24984	24891	27244	25527	25064
doublet states	16823	16984	14779	17462	17394	15522	15998	16421
	17990	17535	16656	17942	18095	17742	18208	18669
	19524	19654	16925	19702	19678	17977	18362	18985
	19641	19804	19051	19992	19937	19257	19301	19061
	20212	20244	19623	20340	20332	19432	19527	19772
	20545	20635	20738	20724	20720	20606	20551	20441
	21971	21965	21725	21926	21925	22021	21664	21671
	23415	23357	22910	23713	23721	23333	23173	23243
	24465	24409	23775	24716	24799	24344	24131	24277
	24721	24777	24576	25077	25094	24542	24514	24443
	25772	25613	25298	25681	25688	25838	25711	25884
	26077	25907	25994	25743	25725	26284	26287	25975
	26633	26754	26984	26880	26840	27872	26980	26755
	27855	27829	28390	27269	27228	28035	27467	27296
	28673	28839	28774	29184	29197	28931	28661	28526
	30012	30050	29736	30148	30100	29776	29575	29705
	30246	30213	29985	30289	30317	30481	29867	29950
	30376	30250	30263	30584	30646	30914	30235	30257
	30690	30829	31417	30898	30841	31089	30869	30575
	31363	31291	32558	31146	31169	32128	31613	31238
	31490	31525	32633	31209	31231	32683	31997	31364
	32685	32837	32830	33047	33077	32761	32204	32209
	33087	33210	33102	33167	33195	33164	32862	32878
	33482	33502	34210	33451	33417	34220	33332	33101
	34712	34751	34836	34786	34742	35429	34658	34505
	35584	35574	36190	35801	35794	35995	35288	35085
	35608	35818	36223	35953	35981	36310	35642	35369
	36693	36813	36855	36885	36896	37143	36156	36051
	44013	44014	44612	44097	44125	44325	44098	43896
	44314	44296	44680	44270	44273	44670	44318	44184
...	

Table D.2.: CASPT2 energies [cm^{-1}] of the ten quartet and the twelve lowest doublet states for the tetrahedral Co(II) complexes investigated in Chapter 4.

	8	9	11	12	13	14	15	16
	0	0	0	0	0	0	0	0
quartet states	2263	2272	1904	2366	2401	2219	1750	1828
	6196	6004	5046	6862	6914	5582	5314	5817
	6430	7161	5882	7444	7351	6176	6151	5872
	8411	8110	7998	7580	7680	9921	8805	8519
	9347	9368	9373	9156	9194	10181	9441	8872
	11654	11939	11415	10778	10510	11016	10271	10450
	19001	18697	19874	19772	20088	19791	19518	19219
	20263	20565	20964	20730	20621	19928	20295	19868
	23439	23928	25715	22661	22386	25248	22837	22373
	doublet states	13686	13814	18464	14210	17612	12252	12908
14762		14421	21087	14628	18218	14767	15553	14553
15929		16363	21571	16518	19967	15527	15699	14997
16714		16792	22914	16920	20342	15644	15838	16105
17317		17362	23167	17438	20855	16564	16822	17012
17752		17780	24991	17944	21410	17704	17735	17628
19126		19170	26160	19062	22557	19282	18967	18918
20277		20206	26983	20445	23909	20299	20133	20096
21229		20848	28811	20750	24293	22088	21973	21341
21927		21258	29453	21426	25149	22187	22068	22141
22818		22725	30061	23316	26746	23131	23240	22993
23341		23373	30303	23338	26927	23447	23311	23159

D. Additional Details for Quantummechanical Calculations

Table D.3.: CASSCF energies [cm^{-1}] of the ten quartet and the 30 lowest doublet states for the square-planar Co(II) complexes investigated in Chapter 4.

	17	19	18	20
quartet states	0	0	0	0
	59	154	222	119
	813	1158	810	1052
	1906	2032	1812	1893
	8493	8447	8830	8427
	10300	10307	10056	10320
	19026	19875	19123	20245
	25290	27348	25233	27553
	29454	28471	29253	28572
	38406	38620	38421	38864
doublet states	3574	2792	3654	2393
	3736	3530	4071	3255
	5801	4918	6059	4630
	12971	12814	13209	12673
	18550	18559	18519	18468
	19009	19406	19120	19444
	20213	20409	20277	20290
	20355	21032	20546	21098
	21518	21809	21573	21654
	22382	22275	22504	22247
	23160	22874	23137	22704
	23450	23130	23351	22873
	25825	25842	26206	25890
	26338	26273	26627	26259
	26616	26577	26860	26546
	27689	27672	27546	27700
	28041	27912	27921	27913
	31820	31697	32217	31675
	33815	33576	33661	33570
	38135	38626	38107	38823
	38301	39644	38303	39855
	39261	40039	39374	40463
	39692	40477	39591	40700
	40555	41506	40457	41667
	40631	42193	40659	42583
	41014	42543	40954	42840
	44228	43833	44023	43914
	44440	44174	44224	44258
	49245	50466	49320	50688
	51701	51160	51649	51349
...	

Table D.4.: CASPT2 energies [cm^{-1}] of the ten quartet and the 12 lowest doublet states for the square-planar Co(II) complexes investigated in Chapter 4.

	17	19	18	20
quartet states	591	1167	161	1491
	752	1303	522	1572
	1414	2574	953	2756
	2821	3300	2347	3363
	7424	7444	7439	7771
	9817	10171	9127	10419
	21828	23243	21558	23925
	25931	28281	25526	28793
	30637	30290	30012	30626
	38063	38736	37743	39324
doublet states	0	0	0	0
	1176	521	909	434
	3053	1961	2964	1972
	8152	8246	7994	8354
	15816	16303	15410	16564
	16208	17356	15822	17768
	17364	18742	16106	18846
	17896	18911	17446	19350
	18856	19428	18493	19718
	19076	19760	18873	19971
	20084	21213	20011	21358
	21986	21968	21226	21746

D.2. Linear Cobalt(II) Complexes

Table D.5.: CASSCF energies [cm^{-1}] of the ten quartet and the 30 lowest doublet states for the linear Co(II) complexes investigated in Chapter 5.

	21	22	23	24	25	26	27
quartet states	0	0	0	0	0	0	0
	2	102	86	368	628	110	409
	1494	1765	3793	2934	3562	1778	2254
	1496	2015	5604	4626	4492	2831	3412
	1559	2162	6275	6416	5770	4628	5206
	1817	2291	6903	6614	6778	5310	5551
	2101	2741	7779	6813	7325	5431	5616
	15386	15336	16985	16709	17080	15711	17149
	18648	19343	22380	23110	23479	23012	21265
	19277	20415	26419	24761	25196	24336	21782
doublet states	17084	16890	15903	15432	16835	15504	16654
	17099	17003	16880	15978	17656	15594	16951
	17579	17270	17202	16247	18108	15991	17005
	17627	17486	17585	17632	18596	17493	18096
	18115	18260	17943	18204	18979	19057	18913
	18149	18389	20219	20099	20186	19195	19676
	18380	18407	20420	20180	20702	19337	19838
	20268	20362	21040	20954	21804	20273	21625
	20271	20767	21985	21435	22686	20852	21811
	20921	20823	22597	22720	23215	21589	22148
	21195	20849	23122	22952	23292	22595	22528
	21250	21023	23863	23715	24347	22932	23545
	22948	23019	24066	25106	24549	24812	25620
	23018	23105	25884	26191	25961	24937	25767
	23418	23336	27369	27265	27340	25295	26252
	23755	23875	27547	27435	27567	25934	26407
	24377	24679	27958	27463	27690	26155	26580
	24418	24783	28029	27710	27980	26295	26641
	24607	24847	28391	27757	28264	27125	26839
	24689	24877	28761	28062	28432	27198	27253
	25710	26436	29307	29375	29242	28807	27938
	25738	26546	30281	30034	30040	28872	28717
	25875	26597	30516	30229	30240	29093	29121
	27113	27480	31073	30305	31317	29418	29740
	27259	27926	32104	31187	31984	29926	29967
	27674	28757	32343	32232	32088	31119	30698
	27675	28942	34070	34007	34051	33496	31021
	28072	28944	34106	34009	34135	33496	31038
	39514	39734	41764	41662	42727	41722	41101
	39700	39952	41912	42237	42956	42767	41332
...	

D. Additional Details for Quantummechanical Calculations

Table D.6.: CASPT2 energies [cm^{-1}] of the quartet and the 12 lowest doublet states for the linear Co(II) complexes investigated in Chapter 5.

	21	22	23	24	25	26	27
	0	0	0	0	0	0	0
	121	88	413	71	896	32	197
quartet states	1827	1356	3643	2367	3344	1023	2430
	1855	2111	6812	5506	4870	3138	4105
	2285	2684	7420	7124	6364	5051	6239
	2823	2924	8386	7578	7975	5831	6884
	2828	3285	9515	7983	8183	6174	6925
	12303	12301	13830	13461	13784	12852	12872
	16196	16578	19460	20139	20887	20824	18449
	17183	18249	25600	23389	23427	22195	20089
	13868	14410	12271	12088	13434	13232	12693
	15179	15336	12685	14458	15183	14692	14401
15810	15612	14859	14941	15585	14907	15130	
15903	15880	15346	15280	16174	14996	15219	
16142	15991	16100	15470	16580	15096	15329	
16498	16442	16517	16892	17353	16679	16511	
16724	16604	17471	17093	18014	17167	16673	
16950	17585	17630	17751	18386	17477	18379	
18663	18270	18609	18376	19917	17752	19066	
18962	18667	19641	19448	20205	18809	19755	
18977	18838	19815	21264	20570	19476	20470	
19340	18967	22023	21704	21084	20718	20755	

Table D.7.: ZFS parameters of the CASPT2/RASSI-SO functions obtained with the SINGLE_ANISO.

	21	22	23	24	25	26	27
D	-175	-192	-150	-180	-134	-202	-174
E	2	3	6	-3	17	4	6
$ \frac{E}{D} $	0.01	0.01	0.04	0.02	0.12	0.02	0.03

D.3. DFT Energies for Calculations on 42

Table D.8.: Energies and spin expectation values $\langle \hat{S}^2 \rangle$ of the high-spin state and broken-symmetry state of the Zn-substituted structures of $\text{Cu}_6/\text{H}_3\text{O}^+$.

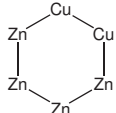
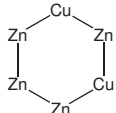
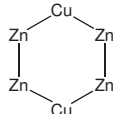
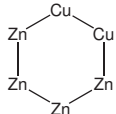
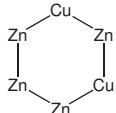
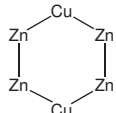
	E_{HS} [a.u.]	E_{BS} [a.u.]	ΔE [cm^{-1}]	$\langle \hat{S}_{\text{HS}}^2 \rangle$	$\langle \hat{S}_{\text{BS}}^2 \rangle$
	-13673.09396841	-13673.09424074	-59.1	2.00	0.99
	-13673.09421864	-13673.09421573	0.6	2.00	1.00
	-13673.09421766	-13673.09421755	0.0	2.00	1.00

Table D.9.: Energies and spin expectation values $\langle \hat{S}^2 \rangle$ of the high-spin state and broken-symmetry state of the Zn-substituted structures of Cu_6 .

	E_{HS} [a.u.]	E_{BS} [a.u.]	ΔE [cm^{-1}]	$\langle \hat{S}_{\text{HS}}^2 \rangle$	$\langle \hat{S}_{\text{BS}}^2 \rangle$
	-13519.33064621	-13519.33087665	-50.1	2.01	1.00
	-13519.33068317	-13519.33067941	0.8	2.01	1.01
	-13519.33071235	-13519.33071243	0.0	2.01	1.01

BIBLIOGRAPHY

- [1] G. E. Moore, *Electronics Magazine* **1965**, 4.
- [2] G. Moore, *Video Transcript Intel* **2005**, 54, 2.
- [3] J. Wang, M. Lundstrom, *Electron Devices Meeting, 2002. IEDM'02. International*, **2002**, pp. 707–710.
- [4] *Molecular Magnets – Physics and Applications*, (Eds.: J. Bartolomé, F. Luis, J. F. Fernández), Springer Berlin Heidelberg, **2014**.
- [5] S. Khizroev, M. Kryder, Y. Ikeda, K. Rubin, P. Arnett, M. Best, D. Thompson, *IEEE Trans. Magn.* **1999**, 35, 2544–2546.
- [6] K. Keng Teo, M. R. Elidrissi, K. S. Chan, Y. Kanai, *Journal of Applied Physics* **2012**, 111, 07B716.
- [7] R. Rottmayer, S. Batra, D. Buechel, W. Challener, J. Hohlfeld, Y. Kubota, L. Li, B. Lu, C. Mihalcea, K. Mountfield, et al., *IEEE Trans. Magn.* **2006**, 42, 2417–2421.
- [8] H. J. Richter, A. Y. Dobin, R. T. Lynch, D. Weller, R. M. Brockie, O. Heinonen, K. Z. Gao, J. Xue, R. J. M. v. d. Veerdonk, P. Asselin, et al., *Appl. Phys. Lett.* **2006**, 88, 222512.
- [9] R. P. Feynman, *International Journal of Theoretical Physics* **1982**, 21, 467–488.
- [10] D. P. DiVincenzo, *Fortschritte der Physik* **2000**, 48, 771–783.
- [11] P. W. Shor, *SIAM journal on computing* **1997**, 26, 1484–1509.
- [12] L. K. Grover, *Proceedings of the twenty-eighth annual ACM symposium on Theory of computing - STOC '96*, **1996**, pp. 212–219.
- [13] L. K. Grover, *Physical Review Letters* **1997**, 79, 325–328.
- [14] T. F. Ronnow, Z. Wang, J. Job, S. Boixo, S. V. Isakov, D. Wecker, J. M. Martinis, D. A. Lidar, M. Troyer, *Science* **2014**, 420–424.
- [15] M. N. Leuenberger, D. Loss, *Nature* **2001**, 410, 789–793.

Bibliography

- [16] F. Troiani, A. Ghirri, M. Affronte, S. Carretta, P. Santini, G. Amoretti, S. Piligkos, G. Timco, R. Winpenny, *Physical review letters* **2005**, *94*, 207208.
- [17] C. J. Wedge, G. A. Timco, E. T. Spielberg, R. E. George, F. Tuna, S. Rigby, E. J. L. McInnes, R. E. P. Winpenny, S. J. Blundell, A. Ardavan, *Physical Review Letters* **2012**, *108*, 107204.
- [18] K.-Y. Choi, Y. H. Matsuda, H. Nojiri, U. Kortz, F. Hussain, A. C. Stowe, C. Ramsey, N. S. Dalal, *Physical review letters* **2006**, *96*, 107202.
- [19] E. T. Spielberg, PhD thesis, Friedrich-Schiller-Universität Jena, **2009**.
- [20] P. Gütlich, H. A. Goodwin in *Spin Crossover in Transition Metal Compounds I*, Springer, **2004**, pp. 1–47.
- [21] M. Mannini, F. Pineider, C. Danieli, F. Totti, L. Sorace, P. Sainctavit, M.-A. Arrio, E. Otero, L. Joly, J. C. Cezar, et al., *Nature* **2010**, *468*, 417–421.
- [22] H. Lueken, *Angewandte Chemie* **2006**, *118*, 8233–8240.
- [23] F. Hund, *Zeitschrift für Physik* **1927**, *40*, 742–764.
- [24] F. Hund, *Zeitschrift für Physik* **1927**, *42*, 93–120.
- [25] H. Lueken, *Magnetochemie*, Teubner, **1999**.
- [26] J. F. Keithley, *The story of electrical and magnetic measurements: from 500 BC to the 1940s*, John Wiley & Sons, **1999**.
- [27] M. N. Leuenberger, D. Loss, *Physical Review B* **2000**, *61*, 1286.
- [28] A. Caneschi, D. Gatteschi, R. Sessoli, A. L. Barra, L. C. Brunel, M. Guillot, *Journal of the American Chemical Society* **1991**, *113*, 5873–5874.
- [29] T. Lis, *Acta Crystallographica Section B Structural Crystallography and Crystal Chemistry* **1980**, *36*, 2042–2046.
- [30] G. Arom, S. M. Aubin, M. A. Bolcar, G. Christou, H. J. Eppley, K. Folting, D. N. Hendrickson, J. C. Huffman, R. C. Squire, H.-L. Tsai, et al., *Polyhedron* **1998**, *17*, 3005–3020.
- [31] G. Aromí, E. K. Brechin in *Structure and Bonding, Vol. 122* (Ed.: R. Winpenny), Springer Berlin Heidelberg, **2006**, pp. 1–67.
- [32] N. Ishikawa, M. Sugita, T. Ishikawa, S.-y. Koshihara, Y. Kaizu, *Journal of the American Chemical Society* **2003**, *125*, 8694–8695.
- [33] F. Branzoli, P. Carretta, M. Filibian, G. Zoppellaro, M. J. Graf, J. R. Galan-Mascaros, O. Fuhr, S. Brink, M. Ruben, *Journal of the American Chemical Society* **2009**, *131*, 4387–4396.

- [34] C. R. Ganivet, B. Ballesteros, G. de la Torre, J. M. Clemente-Juan, E. Coronado, T. Torres, *Chemistry – A European Journal* **2013**, *19*, 1457–1465.
- [35] U. Glebe, T. Weidner, J. E. Baio, D. Schach, C. Bruhn, A. Buchholz, W. Plass, S. Walleck, T. Glaser, U. Siemeling, *ChemPlusChem* **2012**, *77*, 889–897.
- [36] O. Kahn, *Chemical Physics Letters* **1997**, *265*, 109–114.
- [37] J. Yoon, E. I. Solomon, *Coordination Chemistry Reviews* **2007**, *251*, 379–400.
- [38] A. Zharkuskaya, PhD thesis, Friedrich-Schiller-Universität Jena, **2006**.
- [39] L. Cambi, L. Szegö, *Berichte der deutschen chemischen Gesellschaft (A and B Series)* **1931**, *64*, 2591–2598.
- [40] C. D. Coryell, F. Stitt, L. Pauling, *Journal of the American Chemical Society* **1937**, *59*, 633–642.
- [41] E. König, K. Madeja, *Inorg. Chem.* **1967**, *6*, 48–55.
- [42] V. Ksenofontov, A. B. Gaspar, P. Gütlich in *Topics in Current Chemistry, Vol. 235* (Eds.: P. Gütlich, H. Goodwin), Springer Science + Business Media, **2004**, pp. 23–64.
- [43] S. Decurtins, P. Gütlich, C. Köhler, H. Spiering, A. Hauser, *Chemical Physics Letters* **1984**, *105*, 1–4.
- [44] P. Gütlich, A. Hauser, H. Spiering, *Angewandte Chemie* **1994**, *106*, 2109–2141.
- [45] C. Ni, J. C. Fettingner, G. J. Long, P. P. Power, *Inorganic Chemistry* **2009**, *48*, 2443–2448.
- [46] E. W. T. Yemeli, G. R. Blake, A. P. Douvalis, T. Bakas, G. O. R. Alberda van Ekenstein, P. J. van Koningsbruggen, *Chemistry – A European Journal* **2010**.
- [47] S. Hayami, Y. Komatsu, T. Shimizu, H. Kamihata, Y. H. Lee, *Coordination Chemistry Reviews* **2011**, *255*, 1981–1990.
- [48] L. G. Lavrenova, A. V. Virovets, E. V. Peresyphkina, A. D. Strekalova, D. A. Piryazev, V. A. Daletsky, L. A. Sheludyakova, S. F. Vasilevsky, *Inorganica Chimica Acta* **2011**, 1–5.
- [49] V. Ovcharenko, S. Fokin, G. Romanenko, Y. Shvedenkov, V. Ikorskii, E. Tretyakov, S. Vasilevskii, *Journal of Structural Chemistry* **2002**, *43*, 153–167.
- [50] E. T. Spielberg, W. Plass, *European Journal of Inorganic Chemistry* **2011**, *2011*, 826–834.
- [51] A. Buchholz, A. O. Eseola, W. Plass, *Comptes Rendus Chimie* **2012**, *15*, 929–936.
- [52] S. Ziegenbalg, MSc thesis, Friedrich-Schiller-Universität Jena, **2013**.
- [53] J. M. Zadrozny, D. J. Xiao, M. Atanasov, G. J. Long, F. Grandjean, F. Neese, J. R. Long, *Nature Chemistry* **2013**, *5*, 577–581.
- [54] D. Schuch, PhD thesis, Friedrich-Schiller-Universität Jena, **2013**.

Bibliography

- [55] S. Möller, MSc thesis, Friedrich-Schiller-Universität Jena, **2013**.
- [56] A. Burkhardt, PhD thesis, Friedrich-Schiller-Universität Jena, **2008**.
- [57] M. Born, R. Oppenheimer, *Annalen der Physik* **1927**, 389, 457–484.
- [58] W. Pauli, *Zeitschrift für Physik A Hadrons and Nuclei* **1925**, 31, 765–783.
- [59] V. Fock, *Zeitschrift für Physik* **1930**, 61, 126–148.
- [60] J. C. Slater, *Physical Review* **1930**, 35, 210–211.
- [61] C. C. J. Roothaan, *Reviews of modern physics* **1951**, 23, 69–89.
- [62] G. G. Hall, *Proceedings of the Royal Society of London. Series A. Mathematical and Physical Sciences* **1951**, 205, 541–552.
- [63] A. Szabo, N. S. Ostlund, *Modern Quantum Chemistry: Introduction To Advanced Electronic Structure Theory*, Dover publications, **1996**.
- [64] E. Schrödinger, *Annalen der Physik* **1926**, 385, 437–490.
- [65] K. Andersson, P.-A. Malmqvist, B. O. Roos, *The Journal of Chemical Physics* **1992**, 96, 1218–1226.
- [66] L. Brillouin, *Les champs "self-consistents" de Hartree et de Fock*, Paris, **1934**.
- [67] B. O. Roos, P. R. Taylor, P. E. Siegbahn, *Chemical Physics* **1980**, 48, 157–173.
- [68] K. Andersson, P. A. Malmqvist, B. O. Roos, A. J. Sadlej, K. Wolinski, *Journal of Physical Chemistry* **1990**, 94, 5483–5488.
- [69] B. O. Roos, K. Andersson, *Chemical Physics Letters* **1995**, 245, 215–223.
- [70] N. Forsberg, P.-Å. Malmqvist, *Chemical Physics Letters* **1997**, 274, 196–204.
- [71] B. O. Roos, K. Andersson, M. P. Fülcher, L. Serrano-Andrés, K. Pierloot, M. Merchán, V. Molina, *Journal of Molecular Structure: THEOCHEM* **1996**, 388, 257–276.
- [72] W. Kohn, *Rev. Mod. Phys.* **1999**, 71, 1253–1266.
- [73] J. A. Pople, *Angewandte Chemie International Edition* **1999**, 38, 1894–1902.
- [74] P. Hohenberg, W. Kohn, *Physical Review* **1964**, 136, B864–B871.
- [75] W. Kohn, L. J. Sham, *Physical Review* **1965**, 140, A1133–A1138.
- [76] I. N. Levine, *Quantum Chemistry*, Pearson Education, **2009**.
- [77] S. H. Vosko, L. Wilk, M. Nusair, *Canadian Journal of Physics* **1980**, 58, 1200–1211.

- [78] A. D. Becke, *Physical Review A* **1988**, 38, 3098–3100.
- [79] C. Lee, W. Yang, R. G. Parr, *Physical Review B* **1988**, 37, 785–789.
- [80] J. P. Perdew, W. Yue, *Physical Review B* **1986**, 33, 8800–8802.
- [81] C. J. Calzado, D. Maynau, *The Journal of Chemical Physics* **2011**, 135, 194704.
- [82] L. Noodleman, *The Journal of Chemical Physics* **1981**, 74, 5737–5743.
- [83] F. Neese, *Coordination Chemistry Reviews* **2009**, 253, 526–563.
- [84] K. Yamaguchi, T. Tsunekawa, Y. Toyoda, T. Fueno, *Chemical Physics Letters* **1988**, 143, 371–376.
- [85] E. Ruiz, J. Cano, S. Alvarez, P. Alemany, *Journal of Computational Chemistry* **1999**, 20, 1391–1400.
- [86] H. F. King, R. E. Stanton, H. Kim, R. E. Wyatt, R. G. Parr, *The Journal of Chemical Physics* **1967**, 47, 1936–1941.
- [87] F. Neese, *Journal of Physics and Chemistry of Solids* **2004**, 65, 781–785.
- [88] M. M. Khusniyarov, E. Bill, T. Weyhermüller, E. Bothe, K. Harms, J. Sundermeyer, K. Wieghardt, *Chemistry – A European Journal* **2008**, 14, 7608–7622.
- [89] M. M. Khusniyarov, T. Weyhermüller, E. Bill, K. Wieghardt, *Journal of the American Chemical Society* **2009**, 131, 1208–1221.
- [90] M. M. Khusniyarov, E. Bill, T. Weyhermüller, E. Bothe, K. Wieghardt, *Angewandte Chemie* **2011**, 123, 1690–1693.
- [91] D. A. Pantazis, V. Krewald, M. Orio, F. Neese, *Dalton Transactions* **2010**, 39, 4959–4967.
- [92] M. Bühl, H. Kabrede, *Journal of Chemical Theory and Computation* **2006**, 2, 1282–1290.
- [93] F. Neese, T. Schwabe, S. Grimme, *The Journal of Chemical Physics* **2007**, 126, 124115.
- [94] K. Pierloot, E. Tsokos, B. O. Roos, *Chemical Physics Letters* **1993**, 214, 583 – 590.
- [95] F. Habib, O. R. Luca, V. Vieru, M. Shiddiq, I. Korobkov, S. I. Gorelsky, M. K. Takase, L. F. Chibotaru, S. Hill, R. H. Crabtree, M. Murugesu, *Angewandte Chemie* **2013**, 11500–11503.
- [96] L. F. Chibotaru, L. Ungur, *The Journal of Chemical Physics* **2012**, 137, 064112.
- [97] K. C. Mondal, A. Sundt, Y. Lan, G. E. Kostakis, O. Waldmann, L. Ungur, L. F. Chibotaru, C. E. Anson, A. K. Powell, *Angewandte Chemie International Edition* **2012**, 51, 7550–7554.
- [98] L. F. Chibotaru, L. Ungur, C. Aronica, H. Elmoll, G. Pilet, D. Luneau, *Journal of the American Chemical Society* **2008**, 130, 12445–12455.
- [99] L. Ungur, W. Van den Heuvel, L. F. Chibotaru, *New Journal of Chemistry* **2009**, 33, 1224–1230.

Bibliography

- [100] E. v. Lenthe, E. J. Baerends, J. G. Snijders, *The Journal of Chemical Physics* **1993**, *99*, 4597–4610.
- [101] E. van Lenthe, E.-J. Baerends, J. G. Snijders, *The Journal of Chemical Physics* **1994**, *101*, 9783–9792.
- [102] E. Van Lenthe, J. Snijders, E. Baerends, *The Journal of Chemical Physics* **1996**, *105*, 6505–6516.
- [103] M. Reiher, *Theoretical Chemistry Accounts* **2006**, *116*, 241–252.
- [104] P. Å. Malmqvist, B. O. Roos, B. Schimmelpfennig, *Chemical Physics Letters* **2002**, *357*, 230–240.
- [105] F. Aquilante, L. De Vico, N. Ferré, G. Ghigo, P.-å. Malmqvist, P. Neogrády, T. B. Pedersen, M. Pitoňák, M. Reiher, B. O. Roos *et al.*, *Journal of Computational Chemistry* **2010**, *31*, 224–247.
- [106] E. Ruiz, P. Alemany, S. Alvarez, J. Cano, *Journal of the American Chemical Society* **1997**, *119*, 1297–1303.
- [107] L. F. Chibotaru, L. Ungur, A. Soncini, *Angewandte Chemie* **2008**, *120*, 4194–4197.
- [108] A. R. Paital, A.-Q. Wu, Guo, G. Aromí, J. Ribas-Ariño, D. Ray, *Inorganic Chemistry* **2007**, *46*, 2947–2949.
- [109] F. A. Neugebauer, H. Fischer, *Chemische Berichte* **1972**, *105*, 2686–2693.
- [110] F. A. Neugebauer, H. Fischer, *Angewandte Chemie* **1971**, *83*, 756.
- [111] N. V. Moskalev, *Chemistry of Heterocyclic Compounds* **1990**, *26*, 158–160.
- [112] J. E. Kuder, H. W. Gibson, D. Wychick, *The Journal of Organic Chemistry* **1975**, *40*, 875–879.
- [113] H. Zabrodsky, S. Peleg, D. Avnir, *IEEE Transactions on Pattern Analysis and Machine Intelligence* **1995**, *17*, 1154–1166.
- [114] P. Van der Sluis, A. Spek, *Crystallography* **1990**, *46*, 194–201.
- [115] R. Boča, *Coordination Chemistry Reviews* **2004**, *248*, 757–815.
- [116] C. E. Housecroft, A. G. Sharpe, *Inorganic Chemistry*, Prentice Hall, 3rd ed., **2008**.
- [117] *Encyclopedia of Inorganic Chemistry*, (Ed.: R. B. Bruce), John Wiley & Sons, Ltd, **2006**.
- [118] P. V. Bernhardt, G. A. Lawrence in *Comprehensive Coordination Chemistry Part II, Vol. 6* (Eds.: J. McCleverty, T. J. Meyer), Elsevier Pergamon, Oxford, **2004**, Chapter Cobalt, pp. 1–145.
- [119] S. Kremer, W. Henke, D. Reinen, *Inorganic Chemistry* **1982**, *21*, 3013–3022.
- [120] A. B. Gaspar, M. C. Muñoz, V. Niel, J. A. Real, *Inorganic Chemistry* **2001**, *40*, 9–10.
- [121] A. F. Hollemann, E. Wiberg, N. Wiberg, *Lehrbuch der Anorganischen Chemie*, Walter de Gruyter, Berlin, 102nd ed., **2007**.

- [122] E.-C. Yang, D. N. Hendrickson, W. Wernsdorfer, M. Nakano, L. N. Zakharov, R. D. Sommer, A. L. Rheingold, M. Ledezma-Gairaud, G. Christou, *Journal of Applied Physics* **2002**, *91*, 7382–7384.
- [123] M. Murrie, *Chemical Society Reviews* **2010**, *39*, 1986–1995.
- [124] R. Herchel, R. Boča, *Dalton Transactions* **2005**, 1352–1353.
- [125] D. Maganas, S. Sottini, P. Kyritsis, E. J. J. Groenen, F. Neese, *Inorganic Chemistry* **2011**, *50*, 8741–8754.
- [126] J. M. Zadrozny, J. R. Long, *Journal of the American Chemical Society* **2011**, *133*, 20732–20734.
- [127] S. Karasawa, N. Koga, *Inorganic Chemistry* **2011**, *0*, 5186–5195.
- [128] D. Yoshihara, S. Karasawa, N. Koga, *Polyhedron* **2011**, *30*, 3211–3217.
- [129] B. Papánková, R. Boča, L. Dlháč, I. Nemeč, J. Titiš, I. Svoboda, H. Fuess, *Inorganica Chimica Acta* **2010**, *363*, 147–156.
- [130] J. Titiš, R. Boča, *Inorganic Chemistry* **2011**, *50*, 11838–11845.
- [131] J. Titiš, J. Miklovič, R. Boča, *Inorganic Chemistry Communications* **2013**, *35*, 72–75.
- [132] C. Rajnák, J. Titiš, I. Šalitraš, R. Boča, O. Fuhr, M. Ruben, *Polyhedron* **2013**, *65*, 122–128.
- [133] M. Idešicová, J. Titiš, J. Krzystek, R. Boča, *Inorganic Chemistry* **2013**, *52*, 9409–9417.
- [134] E.-F. Dang, X.-W. Wang, Y.-Z. Zhou, G.-P. Han, Q.-C. Yang, *Acta Crystallographica Section E: Structure Reports Online* **2008**, *64*, m1486–m1486.
- [135] Y. N. Belokon, J. Fuentes, M. North, J. W. Steed, *Tetrahedron* **2004**, *60*, 3191–3204.
- [136] K. L. Peretti, H. Ajiro, C. T. Cohen, E. B. Lobkovsky, G. W. Coates, *Journal of the American Chemical Society* **2005**, *127*, 11566–11567.
- [137] W. Hirahata, R. M. Thomas, E. B. Lobkovsky, G. W. Coates, *Journal of the American Chemical Society* **2008**, *130*, 17658–17659.
- [138] C. Fraser, L. Johnston, A. L. Rheingold, B. S. Haggerty, G. K. Williams, J. Whelan, B. Bosnich, *Inorganic Chemistry* **1992**, *31*, 1835–1844.
- [139] A.-X. Li, Y. Yang, J.-L. Wang, *Yingyong Huaxue* **2004**, *49*.
- [140] L. Ungur, M. Thewissen, J.-P. Costes, W. Wernsdorfer, L. F. Chibotaru, *Inorganic Chemistry* **2013**, *52*, 6328–6337.
- [141] M. D. Hanwell, D. E. Curtis, D. C. Lonie, T. Vandermeersch, E. Zurek, G. R. Hutchison, *J. Cheminformatics* **2012**, *4*, 17.
- [142] P. P. Power, *Chemical Reviews* **2012**, *112*, 3482–3507.

Bibliography

- [143] J. M. Zadrozny, M. Atanasov, A. M. Bryan, C.-Y. Lin, B. D. Rekker, P. P. Power, F. Neese, J. R. Long, *Chemical Science* **2013**, *4*, 125–138.
- [144] F. Neese, *Wiley Interdisciplinary Reviews: Computational Molecular Science* **2012**, *2*, 73–78.
- [145] R. A. Bartlett, P. P. Power, *Journal of the American Chemical Society* **1987**, *109*, 7563–7564.
- [146] H. Chen, R. A. Bartlett, M. M. Olmstead, P. P. Power, S. C. Shoner, *Journal of the American Chemical Society* **1990**, *112*, 1048–1055.
- [147] T. Nguyen, A. Panda, M. M. Olmstead, A. F. Richards, M. Stender, M. Brynda, P. P. Power, *Journal of the American Chemical Society* **2005**, *127*, 8545–8552.
- [148] C. Ni, T. A. Stich, G. J. Long, P. P. Power, *Chemical Communications* **2010**, *46*, 4466–4468.
- [149] A. M. Bryan, W. A. Merrill, W. M. Reiff, J. C. Fettinger, P. P. Power, *Inorganic Chemistry* **2012**, *51*, 3366–3373.
- [150] C.-Y. Lin, J.-D. Guo, J. C. Fettinger, S. Nagase, F. Grandjean, G. J. Long, N. F. Chilton, P. P. Power, *Inorganic Chemistry* **2013**, *52*, 13584–13593.
- [151] A. M. Bryan, G. J. Long, F. Grandjean, P. P. Power, *Inorganic Chemistry* **2014**, 2692–2698.
- [152] J. T. Hougen, G. E. Leroi, T. C. James, *The Journal of Chemical Physics* **1961**, *34*, 1670–1677.
- [153] C. W. DeKock, D. M. Gruen, *The Journal of Chemical Physics* **1966**, *44*, 4387–4398.
- [154] R. A. Berg, O. Sinanoglu, *The Journal of Chemical Physics* **1960**, *32*, 1082–1087.
- [155] D. W. Smith, *Inorganica Chimica Acta* **1971**, *5*, 231–240.
- [156] A. B. P. Lever, B. R. Hollebone, *Inorganic Chemistry* **1972**, *11*, 2183–2189.
- [157] S. G. Wang, W. H. E. Schwarz, *The Journal of Chemical Physics* **1998**, *109*, 7252–7262.
- [158] V. V. Sliznev, N. Vogt, J. Vogt, *Molecular Physics* **2004**, *102*, 1767–1776.
- [159] M. Hargittai, *Coordination Chemistry Reviews* **1988**, *91*, 35–88.
- [160] J. D. Rinehart, J. R. Long, *Chemical Science* **2011**, *2*, 2078–2085.
- [161] J. Sievers, *Z. Physik B - Condensed Matter* **1982**, *45*, 289–296.
- [162] C. Loosli, S.-X. Liu, A. Neels, G. Labat, S. Decurtins, *Zeitschrift für Kristallographie-New Crystal Structures* **2006**, *221*, 135–141.
- [163] D. N. Woodruff, R. E. P. Winpenny, R. A. Layfield, *Chemical Reviews* **2013**, *113*, 5110–5148.
- [164] S.-D. Jiang, B.-W. Wang, H.-L. Sun, Z.-M. Wang, S. Gao, *Journal of the American Chemical Society* **2011**, *133*, 4730–4733.

- [165] M. A. AlDamen, J. M. Clemente-Juan, E. Coronado, C. Marti-Gastaldo, A. Gaita-Arino, *Journal of the American Chemical Society* **2008**, *130*, 8874–8875.
- [166] J. D. Rinehart, M. Fang, W. J. Evans, J. R. Long, *Journal of the American Chemical Society* **2011**, *133*, 14236–14239.
- [167] B. H. Koo, K. S. Lim, D. W. Ryu, W. R. Lee, E. K. Koh, C. S. Hong, *Chemical Communications* **2012**, *48*, 2519–2521.
- [168] J. Bauer, PhD thesis, Friedrich-Schiller-Universität Jena, **2009**.
- [169] D. Aravena, E. Ruiz, *Inorganic Chemistry* **2013**, *52*, 13770–13778.
- [170] S. Alvarez, P. Alemany, D. Casanova, J. Cirera, M. Llunell, D. Avnir, *Coordination Chemistry Reviews* **2005**, *249*, 1693–1708.
- [171] K. B. Sharpless, *Angewandte Chemie International Edition* **2002**, *41*, 2024–2032.
- [172] W. S. Knowles, *Angewandte Chemie International Edition* **2002**, *41*, 1998–2007.
- [173] R. Noyori, *Angewandte Chemie International Edition* **2002**, *41*, 2008–2022.
- [174] G. Rikken, E. Raupach, *Nature* **1997**, *390*, 493–494.
- [175] A. Burkhardt, A. Buchholz, H. Görls, W. Plass, *European Journal of Inorganic Chemistry* **2006**, *2006*, 3400–3406.
- [176] A. Burkhardt, E. T. Spielberg, H. Görls, W. Plass, *Inorganic Chemistry* **2008**, *47*, 2485–2493.
- [177] V. H. Crawford, H. W. Richardson, J. R. Wasson, D. J. Hodgson, W. E. Hatfield, *Inorganic Chemistry* **1976**, *15*, 2107–2110.
- [178] E. Ruiz, A. Rodriguez-Fortea, P. Alemany, S. Alvarez, *Polyhedron* **2001**, *20*, 1323–1327.
- [179] M. S. Lah, V. L. Pecoraro, *Journal of the American Chemical Society* **1989**, *111*, 7258–7259.
- [180] G. Mezei, C. M. Zaleski, V. L. Pecoraro, *Chemical Reviews* **2007**, *107*, 4933–5003.
- [181] D. S. Nesterov, J. Jezierska, O. V. Nesterova, A. J. L. Pombeiro, A. Ozarowski, *Chemical Communications* **2014**, *50*, 3431.
- [182] J. Schnack, *Dalton Transactions* **2010**, *39*, 4677–4686.
- [183] E. Ruiz, J. Cano, S. Alvarez, A. Caneschi, D. Gatteschi, *Journal of the American Chemical Society* **2003**, *125*, 6791–6794.
- [184] D. Plaul, PhD thesis, Friedrich-Schiller-Universität Jena, **2009**.
- [185] J. Bauer, MSc thesis, Friedrich-Schiller-Universität Jena, **2006**.

Bibliography

- [186] G. M. Sheldrick, *Acta Crystallographica Section A: Foundations of Crystallography* **2007**, *64*, 112–122.
- [187] O. V. Dolomanov, L. J. Bourhis, R. J. Gildea, J. A. Howard, H. Puschmann, *Journal of Applied Crystallography* **2009**, *42*, 339–341.
- [188] *TURBOMOLE V6.2 2010, a development of University of Karlsruhe and Forschungszentrum Karlsruhe GmbH, 1989-2007, TURBOMOLE GmbH, since 2007; available from <http://www.turbomole.com>.*
- [189] F. Weigend, R. Ahlrichs, *Physical Chemistry Chemical Physics* **2005**, *7*, 3297–3305.
- [190] A. D. Becke, *The Journal of Chemical Physics* **1993**, *98*, 5648–5652.
- [191] J. Finley, P.-A. Malmqvist, B. O. Roos, L. Serrano-Andrés, *Chemical Physics Letters* **1998**, *288*, 299–306.
- [192] B. O. Roos, R. Lindh, P.-Å. Malmqvist, V. Veryazov, P.-O. Widmark, *Journal of Physical Chemistry A* **2004**, *108*, 2851–2858.
- [193] B. O. Roos, R. Lindh, P.-A. Malmqvist, V. Veryazov, P.-O. Widmark, *Journal of Physical Chemistry A* **2005**, *109*, 6575–6579.
- [194] B. O. Roos, R. Lindh, P.-A. Malmqvist, V. Veryazov, P.-O. Widmark, A. C. Borin, *Journal of Physical Chemistry A* **2008**, *112*, 11431–11435.
- [195] H. Zabrodsky, S. Peleg, D. Avnir, *Journal of the American Chemical Society* **1992**, *114*, 7843–7851.
- [196] D. Avnir, O. Katzenelson, S. Keinan, M. Pinsky, Y. Pinto, Y. Salomon, H. Zabrodsky Hel-Or, D. Rouvray in *Concepts in Chemistry: A Contemporary Challenge*, Rouvray, DH, Ed, **1997**.
- [197] D. Casanova, J. Cirera, M. Llunell, P. Alemany, D. Avnir, S. Alvarez, *Journal of the American Chemical Society* **2004**, *126*, 1755–1763.
- [198] M. Llunell, D. Casanova, J. Cicera., *SHAPE 2.1: Program for the Stereochemical Analysis*, <http://www.ee.ub.es/index.php/research/continuous-shape-and-symmetry-measures-applications-in-structural-chemistry>.

CURRICULUM VITAE

Personal Data

Name	David Hornig
Date of birth	October 17, 1984
Place of birth	Werdau
Nationality	German
Personal status	single
Current working address	Friedrich-Schiller-University Jena Humboldtstraße 8 07743 Jena Germany
E-mail	david.hornig@uni-jena.de

Professional Experience

10/2009-present	Scientific coworker in the group of Winfried Plass at the Friedrich-Schiller-University Jena
-----------------	----------------------------------------------------------------------------------------------

Degrees and Education

2009	Diploma in Chemistry Thesis: "Synthese und Eigenschaft neuartiger Fluorubinderivate"
2004-2009	Studies in Chemistry, Friedrich-Schiller-University Jena, Germany
June 2003	Abitur (A-level)
1995-2003	Grammar School "Gerhard Hauptmann" in Zwickau
1991-1995	Elementary School in Zwickau

Bibliography

Basic Military Service

10/2003-06/2004 Self-Propelled Artillery bataillon 115 (PzArtBtl 115)
in Neunburg vorm Wald, Germany

Teaching Experience

2010-2013	Exercise in Bioinorganic Chemistry (EPR spectroscopy, 6th semester)
2010-2013	Exercise in Inorganic Chemistry (2nd semester)
2010-2013	Practical Course in Inorganic Chemistry (quantitative analysis, 2nd semester)
2013-2015	Exercise in Inorganic Chemistry (1st semester)
2013-2015	Practical Course in Inorganic Chemistry (qualitative analysis, 1st semester)

Jena, January 6, 2015

David Hornig

DECLARATION OF ORIGINALITY

I certify that the work presented here is, to the best of my knowledge and belief, original and the result of my own investigations, except as acknowledged, and has not been submitted, either in part or whole, for a degree at this or any other university.

Ich erkläre, dass ich die vorliegende Arbeit selbstständig und nur unter Verwendung der angegebenen Hilfsmittel, persönlichen Mitteilungen und Quellen angefertigt habe und dass ich nicht die gleiche, eine in wesentlichen Teilen ähnliche oder eine andere Abhandlung bei einer anderen Hochschule als Dissertation eingereicht habe.

Jena, January 6, 2015

David Hornig